Developments of Two Methodologies in Uncertainty Quantification in Civil Engineering and Engineering Mechanics

Mengyao Shen

Submitted in partial fulfillment of the
requirements for the degree of
Doctor of Philosophy
under the Executive Committee
of the Graduate School of Arts and Sciences

COLUMBIA UNIVERSITY

2022

Abstract

Developments of Two Methodologies in Uncertainty Quantification in Civil Engineering and Engineering Mechanics

Mengyao Shen

Uncertainty is ubiquitous in civil infrastructure systems and has a major impact on decision-making for structural safety and reliability, and for assessing and managing risk. This dissertation explores the field both from the theoretical-mathematical modeling point of view, as well as from the practical applications perspective. Two problems addressed in the dissertation: 1) how to quantify the randomness in material properties and 2) what's the impact for the uncertainties in material properties on the response/safety of the civil structures.

There are two distinct parts in the dissertation. Part I focuses on the strength evaluation of main cables for long span suspension bridges. A novel methodology is proposed to evaluate the ultimate strength of the main cables of suspension bridges using information obtained from site inspections and from tensile strength tests on selected wire samples extracted from the bridge's main cables. A new model is proposed accounting for the spatial variation of individual wires' strength along their length, an important physical attribute of corroded wires considered here for the first time. This model includes: (1) mapping the corrosion stage variation along one-panel-long wires that are visible during an inspection, (2) establishing probability distribution functions for

the ultimate tensile strength of 18″ long wire segments in each corrosion stage group, (3) generating random realizations of the ultimate strength of all the wires in the cable's cross section, accounting for their strength variation along the entire panel length, and (4) accounting for the effect of broken wires in the evaluation panel as well as in adjacent panels. A Monte Carlo simulation approach is finally proposed to generate random realizations of the ultimate overall strength of the cable, using an incremental loading procedure. The final outcome is the probability distribution of the ultimate strength of the entire cable. The methodology is demonstrated through the cable strength evaluation of the FDR Mid-Hudson Bridge and Bear Mountain Bridge in New York state, and compared with corresponding results obtained using the current guidelines of NCHRP Report 534.

Part II is more theoretical in nature and focuses on estimating the stochastic response variability of structures with uncertain material properties modeled by stochastic fields. The concept of Variability Response Function (VRF) is applied in the dissertation to quantify the response variability (e.g., mean and variance) of statically indeterminate structures. Two types of response for statically indeterminate beams at a specific location x are studied: bending moment $M(x)$ and displacement/deflection $w(x)$. By solving the governing equations of the statically indeterminate structure, the responses along the length of the beam, $M(x)$ and $w(x)$, are expressed as a function of its (random) zero-moment location denoted by h. For bending moment $M(x)$, combined with a second-order Taylor series expansion of the random zero-moment location h, novel Variability Response Function-based integral expressions for the variance of the response bending moment, $\mathrm{Var}[M(x)]$, are established. Extensive numerical examples are provided where the accuracy of the results obtained using the proposed formulation is validated using Monte Carlo simulations involving stochastic fields that follow truncated Gaussian and shifted lognormal

probability distribution functions. These Monte Carlo simulation results indicate that the proposed Variability Response Functions are probability-distribution-independent. For deflection $w(x)$, by introducing hinges at zero-moment location h, a statically indeterminate structure can be transformed into its equivalent statically determinate structure. An approximate close-form analytical expression of VRF is therefore built based on the transformed statically determinate structure with all (probabilistically) possible hinge locations. An ensemble average is taken to get the overall variability response function of the system, which can be replaced by the VRF with the hinge located at the same zero-moment point with the deterministic system without any randomness. This Variability Response Function can provide approximate estimates of the stochastic response variability with reasonable accuracy. Moreover, to get more accurate estimates of the statically indeterminate system, the results from the approximate variability response function can be further refined by introducing a correction term Dw. Finally, the corrected response variability of the original statically indeterminate structure can be obtained with almost perfect accuracy (compared to brute force Monte Carlo simulations). To sum up, the proposed VRFs of statically indeterminate beams, for both bending moment and deflection, have numerous desirable attributes including the capability to perform a full sensitivity analysis of the response variability with respect to the spectral characteristics of the random field modeling the uncertain material/system properties and establishing realizable upper bounds of the response variability.

Table of Contents

List of Figures

List of Tables

Acknowledgments

The dissertation covers my four-year work as a Ph.D. student at Columbia University. It would not be possible without the support from many people. First of all, I want to express my sincere gratitude to my advisor Prof. Deodatis. His endless patience and support walked me through the difficult times. Also, he always gave me insights and inspired me on the research by his unique wisdom and experience. Without his guidance, I would not make any achievements and complete my doctoral studies. I also would like to thank my advisor, Prof. Betti for his care and encouragement of not only my research but also my life. He has always been approachable any time I needed discussions and he is the one who always encouraged me to chase my dream. Besides, I also want to thank the committee members of my defense, Prof. Feng, Prof. Kougioumtzoglou and Prof. Arwade, for their attendance and the valuable suggestions and comments on this dissertation.

My appreciation also goes to my family and friends back in China. I owe many thanks to my parents, who are always supportive of my decision to pursue Ph.D. at Columbia University and care a lot about my life in U. S. And also, for my grandparents, I'm really appreciated for their love and I wish they could be proud of me in heaven. In addition, I would like to thank my dearest friends, Ning and Xiaoman, who are always there and helped me go through the darkest time.

In the past four years at Columbia University, I met a lot of good friends. I want to express my gratitude to them for making my life at Columbia University colorful and giving me nice memories. They are Chuanqi Liu, Guo Tian, Aoran Xu, Yuki Miura, Siyan Wang, Yang Jiao, Ran Ma, Haokai Zhao, Maria Katsidoniotaki, Zhenyu Shou, Gurpreet Singh Hora, Zhaobin Mo, Lechen

Li, Lampros Svolos. I also want to thank my roommates, Weiwei Zhan, Yuwei Liu and Queenie Ng, for making our apartment a lovely place.

Last but not least, I want to express my gratitude to all the faculty and staff in the Department of Civil Engineering and Engineering Mechanics. I also feel honored and grateful to receive the Presidential Fellowship from Columbia University throughout my doctoral studies. The work in Part I is sponsored by the Transportation Research Board through the National Cooperative Highway Research Program Project 12-115, whose support is gratefully acknowledged.

To my family and friends

Chapter 1 Introduction

1.1 Introduction

In this dissertation, some research progresses in the field of uncertainty quantification in civil engineering and engineering mechanics are presented. Two problems addressed in the dissertation: 1) how to quantify the spatial randomness in material properties and 2) what's the impact for the uncertainties in material properties on the response/safety of the civil structures, around which there are two distinct parts.

Part I discusses the problem of strength of main cables for ageing long-span suspension bridges, which is one of the most important factors affecting their safety because of the deterioration caused by corrosion during their long service life. A new model is developed in this part to model the spatial variability of the strength of wires due to the corrosions. And then Monte Carlo simulation is applied to generate random realizations of the ultimate overall strength of the cable. The final outcome is the probability distribution of the ultimate strength of the entire cable. Part II presents the work on the response variability of statically indeterminate beam structures caused by uncertain material properties which can be modeled by random fields. The concept of Variability Response Function (VRF) is introduced. And VRFs for statically indeterminate beam structures are developed to evaluate the variability of response bending moment and deflection of the structures for the first time.

1.2 Outline

Part I is about general methodology for inspection and strength evaluation of suspension bridge main cable systems. Chapter 2 is the background and literature review of the topic. Inspection

methods for suspension bridge inspection, e.g., cable wedging inspection, Non-Destructive Evaluation (NDE) and Structural Health Monitoring (SHM) techniques, are introduced. For cable strength evaluation, current standard and the random field method are reviewed. Chapter 3 establishes the corrosion model for cable segment. It includes the model along the wires accounting for the spatial variability of wire strength as well as the model for the cross section of the cable representing the worst corrosion conditions along the wires. Chapter 4 introduces a Monte Carlo approach to generate realizations of wire strength making use of the corrosion models in Chapter 3, together with the laboratory tensile testing data of wire segments. Redevelopment of broken wires in adjacent panels is also considered in this chapter by reducing the simulated strength of wires obtained in Monte Carlo approach. Finally, an incremental process is carried out to estimate the overall cable strength. Chapter 5 is the applications of the proposed methodology in engineering practice. For illustration, two suspension bridges in New York state are introduced with all the inspection and laboratory tests information. A comparison with current national standard is also carried out to demonstrate the superiority of the methodology in the dissertation.

Part II deals with the development of Variability Response Functions of statically indeterminate structures. In Chapter 6, the introduction and development of VRF are reviewed. A statically indeterminate beam model is then built with random variability of material properties modeled as random fields. Zero-moment location of the beam is pointed out as a random variable related to the random field. The response functions (bending moment and deflection) are expressed as a function of its (random) zero-moment location for the further derivation of VRFs. Chapter 7 develops the VRFs for bending moment. Taylor expansions are applied to the random zero-moment location, leads to novel Variability Response Function-based integral expressions for the variance of the response bending moment. Numerical example is followed to demonstrate the

effectiveness of the VRFs. Chapter 8 deals with another type of response for statically indeterminate beams, deflection. Hinges are introduced at the zero-moment locations to transform the original beam into a statically determinate beam, and an approximate close-form analytical VRF is therefore built based on the transformed statically determinate structure with all possible hinge locations. Furthermore, improvements are made by introducing a correction term for the results by the approximate VRF with perfect accuracy.

Finally, Chapter 9 summarizes the work in this dissertation, including the conclusions for the researches in the two parts and possible directions for future exploration that the author is very interested in. Reference and appendix are followed after Chapter 9. And Appendix A summarizes all the formulas involved in the expressions established for the response variability of bending moment using both a first-order and a second-order Taylor series expansion.

Part I Risk-based Methodology for Inspection and Strength Evaluation of Suspension Bridge Main Cables

Chapter 2 Background

For long span suspension bridges, the strength of their main cables is one of the most significant factors affecting their safety, especially because of the deterioration caused by corrosion during their long service life. Because of the complex structure of a main cable of a suspension bridge (i.e. thousands of high-strength wires, tightly compacted against each other in an overall cylindrical shape), and because of the complex corrosion conditions (i.e. different wires, as well as different locations along the same wire, might have different corrosion conditions), the evaluation of the remaining cable strength after years of service remains a challenging topic.

The accurate evaluation of the strength of a main cable that has been in service for many years depends on the availability of information about the condition of the various wires: the more reliable and extensive this information is, the more accurate the strength estimation is. There are several ways to obtain the information through the inspection of suspension bridge cables, including the conventional cable wedging and also Non-Destructive Evaluation (NDE) and Structural Health Monitoring (SHM) techniques.

2.1 Suspension bridge cable inspection

2.1.1 Cable wedging inspection

Currently, the most practical and effective way to acquire wires condition information is primarily through invasive cable inspections, in which main cables are unwrapped of their external protective coating (either wire or epoxy wrapping), wedged at various locations around their circumference, and visually inspected (see Figure 2.1). If deemed necessary, some wire samples are removed and tested in a laboratory for ultimate strength and corresponding elongation, as well as

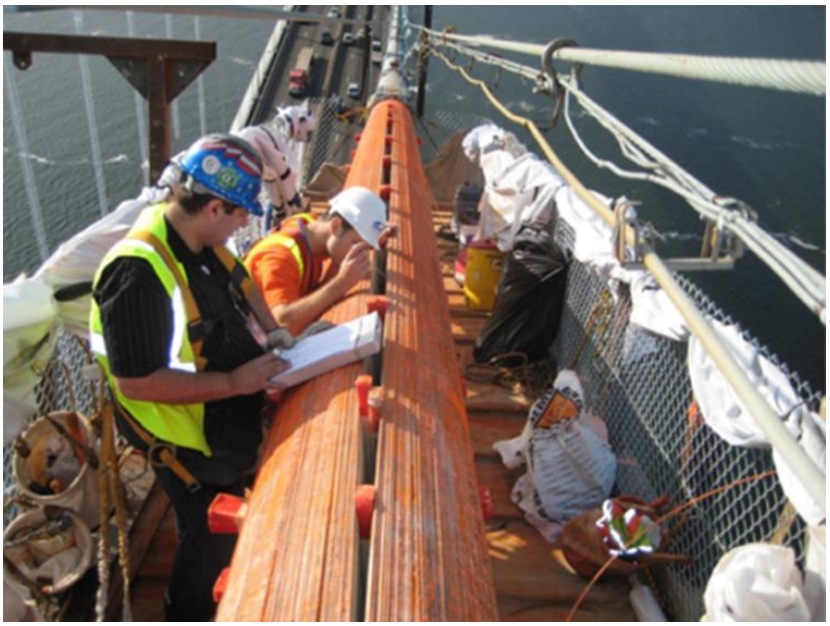

Figure 2.1: Inspection of a suspension bridge main cable using wedging (courtesy of Modjeski and Masters).

for fatigue. Inspection through cable wedging still constitutes the most effective method of extracting information for suspension bridge cable strength evaluation. As the extracted data are limited (only a small percentage of the total number of wires is inspected) and uncertain (visually estimating the corrosion stage is not foolproof), the ensuing strength estimation must be performed probabilistically. This was done for the first time during the 1988 major inspection of the Williamsburg Bridge [1]. Matteo et al. [2] used the raw inspection results of the 1988 Williamsburg Bridge to estimate the safety of its main suspension cables by Monte Carlo simulation and by considering extreme value distributions for the wire strength. Since then, various probability distribution models have been used (e.g., Gaussian, Type I and III (Weibull) extreme value distributions) to describe the mechanical characteristics of corroded wires (e.g., ultimate tensile strength) [3]. In 2011, Mahmoud introduced the BTC method [4] for cable strength estimation, a proprietary method that accounts for the wire's fracture toughness but with limited information available about its specifics.

2.1.2 Non-Destructive Evaluation (NDE) and Structural Health Monitoring (SHM) techniques

Lately, as emerging new technologies and computational capabilities are becoming available, attempts to obtain information about the internal cable conditions through Non-Destructive Evaluation (NDE) and Structural Health Monitoring (SHM) techniques have been made. NDE/SHM provides information about conditions inside a cable without the investigator having to remove the covering or otherwise alter the condition of the cable. The non-removal of the exterior wrapping and avoiding the cable wedging operation would be extremely advantageous for the bridge owners as well as for the overall "health" of the cable. Nickerson [5] developed a list of research needed for providing improved non-destructive inspection and evaluation techniques in a workshop in 1998. Sluszka et al. [6] mentioned new acoustic monitoring technologies which permit long-term monitoring of cables to detect breaking wires. Noyan et al. [7] measured of the strain/stress transfer among wires in parallel wire strands using neutron diffraction. Sloane et al. [8] carried out a testing of a full-scale specimen of a suspension bridge cable in an accelerated corrosive environment by placing a variety of sensors. Betti et al. [9] summarized the monitoring techniques on bridges cables, and a sensor system was also developed to analyze the corrosion of the main cables comprehensively. Park et al. [10] proposed a noncontact main cable NDE method of suspension bridge to observe the cross-sectional loss, utilizing the direct current (DC) magnetization and a searching coil-based total flux measurement.

However, due to the structural and mechanical complexity of the suspension bridge cable system, there are many non-destructive evaluation techniques that work either in principle or on smaller cables, e.g., suspenders, but, when brought to a main cable, they fail or provide unsatisfactory results. The use of NDE/SHM techniques for the estimation of interior cable

conditions is still in the development phase, with substantial logistic challenges still to be overcome (e.g., large diameter cables, distribution of deterioration, etc.).

2.2 Current national standard NCHRP Report 534

In engineering practice, the current standard for suspension bridge cable strength estimation, both nationally and internationally, is represented by the methodology proposed in NCHRP Report 534 [11]. This report provides a thorough cable strength evaluation process, from planning the inspections to the eventual strength estimation. The corresponding guidelines contain detailed steps for all field operations, laboratory tests and computational procedures, which are necessary to ensure consistent and repeatable results. In 2012, FHWA published a primer document [12] to supplement the report. Cable wedging inspection in section 2.1.1 is applied here. Then, a number of long wire samples (usually 20-40 ft long) within the cable's cross-section that provides a representative pool of all sectors of the cable are taken out. The long wire samples are cut into several segments with length l_s which are tested in lab for tensile strength.

With information obtained from inspection and laboratory testing, cable strength is calculated by the following procedures: 1) map and estimate wire deterioration by classifying all wires within the evaluated panel into five groups, and then a corrosion map for the cable profile is generated; 2) determine the probability distributions of the strength of the wire samples taken from the site by the laboratory results of wire segments, and then find the probable minimum tensile strength of each wire sample; 3) establish the strength of unbroken wires for the entire cable's cross section. Here, NCHRP Report 534 gives three methods to calculate unbroken wire strength R_u:

- Simplified Model: applies to cables that have very few cracked wires. It subtracts all the broken and cracked wires.

- Brittle wire Model: assumes that all the wires are subjected to the same tensile stress at any given strain. It's also the most commonly used model in practice.
- Limited Ductility Model: applies to wires that display unusual variations in tensile strength. The ultimate strain rather than stress of the wires is used as the variable in the distribution functions.

After obtaining the strength of unbroken wires, one last step is to calculate redevelopment strength of broken wires. The broken wire will redevelop its force as the distance from the break increases. This increase in wire force is caused by the friction at the cable bands. The force in a wire developed at a cable band is estimated using the measured gap between the ends of the broken wire. Eventually, the cable strength is the sum of unbroken wire strength R_u and redeveloped strength of broken wires R_b.

As current national standard, NCHRP Report proposes a systematic way for the strength evaluation for long-span suspension bridge cables. However, there is something very important missing in the cable strength estimation methodology in NCHRP Report 534: the spatial variation of the wire strength along the length of the wires within a panel (defined as the length of cable between two cable bands). For ductile materials like steel, there is always spatial variation in the wire strength along the length of a wire. In contrast to this fact, NCHRP Report 534 assumes that the strength of each wire within a panel is constant. This assumption can lead to erroneous results as will be shown later in this dissertation.

2.3 Random field method for wire strength

To account for this spatial variation in the wire strength, Shi et al. [13] introduced a random field model to describe the spatial correlation of wire strength along its length, and then included

this model in a methodology to estimate the remaining strength of the overall suspension bridge cable. In this method, the wire strength is modeled as a non-Gaussian random field along its length, the correlations in strength between different locations along the wire can be described by an autocorrelation function. The idea behind the approach in Shi et al. [13] is that the random field model is first applied to individual long ungalvanized wires (as a one-dimensional random field) so that the overall strength of each single long wire (i.e., its minimum strength) can be determined. The strength of the overall cable can then be obtained by adding together the strengths of each individual wire in the cable. However, although the Shi et al. [13] approach resolves the aforementioned NCHRP Report 534 drawback, it has two problems of its own: (1) it is overly complex mathematically and it only applies to ungalvanized wires, and (2) it can become computationally expensive when the number of wires in the cable cross section becomes very large.

2.4 Scope of the research

The main objective behind this part of research is to introduce a simple, efficient, practical and systematic approach to evaluate the overall cable strength, including full consideration of the spatial variation of wire strength. Furthermore, the new approach should not increase the cost of cable inspections from the current NCHRP Report 534 standard. The ultimate outcome of the proposed novel methodology is to establish the probability distribution function of the remaining ultimate strength of the entire cable. The proposed methodology is validated by performing the cable strength evaluation of the Franklin Delano Roosevelt Mid-Hudson Bridge and Bear Mountain Bridge in New York State, and comparing the results with the corresponding ones obtained using the current NCHRP Report 534 guidelines.

Chapter 3 Corrosion Model for Cable Segment

A corrosion model is proposed in this chapter, accounting for the spatial variation of individual wires' strength along their length, an important physical attribute of corroded wires considered here for the first time. This model includes: (1) mapping the corrosion stage variation along one-panel-long wires that are visible during an inspection, (2) the overall corrosion map of the whole cross-section of the evaluated panel.

3.1 The different levels of wire corrosion degradation

During an inspection, as already mentioned, the cable's cross section is wedged open at multiple locations along its circumference and continuously along its length within one panel. The corroded wires can be observed. There are some researches on the corrosion mechanism of the wires based on physical and chemical parameters of the environment to evaluate the level of corrosion [14]-[18], which is beyond scope of this dissertation. Here, wire corrosion level is determined visually and is classified into four different stages according to a classification presented by Hopwood and Havens [19]. These four stages of wire corrosion are defined as follows:

- Stage 1: white spots on the surface of the wire, indicating early stages of zinc oxidation
- Stage 2: white zinc oxidation over the entire wire surface
- Stage 3: white zinc oxidation in some areas of the wire, with brown rust spots not covering more than 30% of a 3-6 in. length of wire
- Stage 4: brown spots prevalent over the wire surface, covering more than 30% of a 3-6 in. length of wire

Figure 3.1 illustrates the four corrosion stages, which can be observed during cable inspection Apart from the above four groups, broken wires are classified into a single group regardless of corrosion stage.

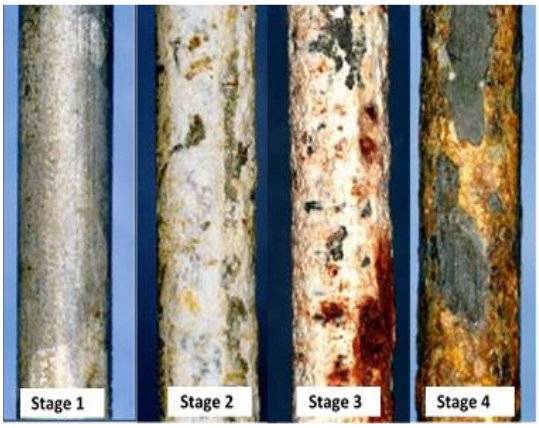

Figure 3.1: Four Corrosion Stages of Wires (Mayrbaurl and Camo [11])

3.2 Establishing the corrosion stage variation along long wires

The panel of the main cable under consideration is unwrapped and inspected by wedging at different locations along its length and around its circumference. The length of the panel, L_p, is defined as the distance between the end sections of two consecutive cable bends. The number of inspection locations along the panel length, N_i, depends on the length of the panel. Based on current engineering practice, the minimum number of inspection locations within a panel is given by:

- For panel lengths less than 30 ft: $N_i = 3$
- For panel lengths between 30 ft and 50 ft: $N_i = 4$
- For panel lengths more than 50 ft: $N_i = 5$.

The corrosion condition of the wires within the cable's cross-section is determined by inserting wedges at *r* locations along the cable's circumference. Figure 3.2 shows typical locations of wedged

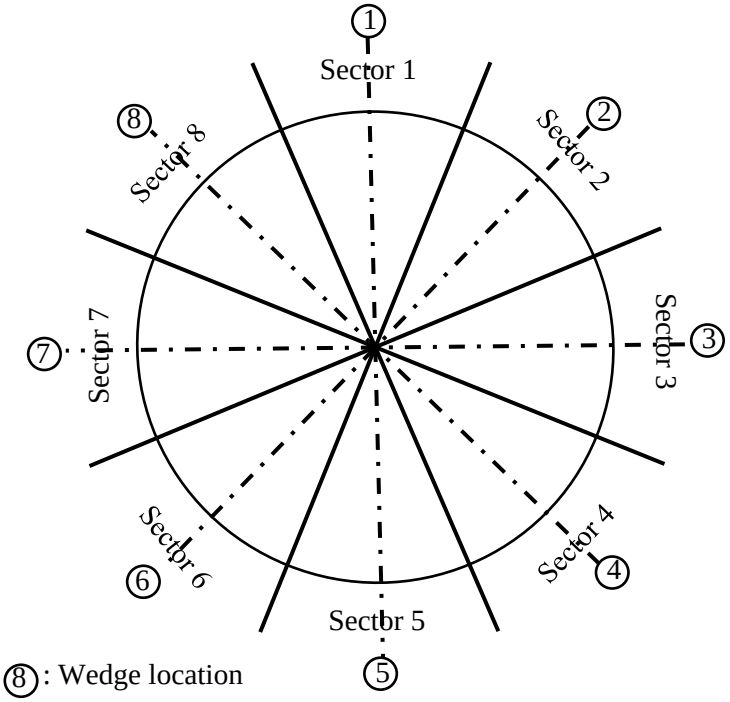

Figure 3.2: Typical wedged locations along the circumference of the cable's cross section

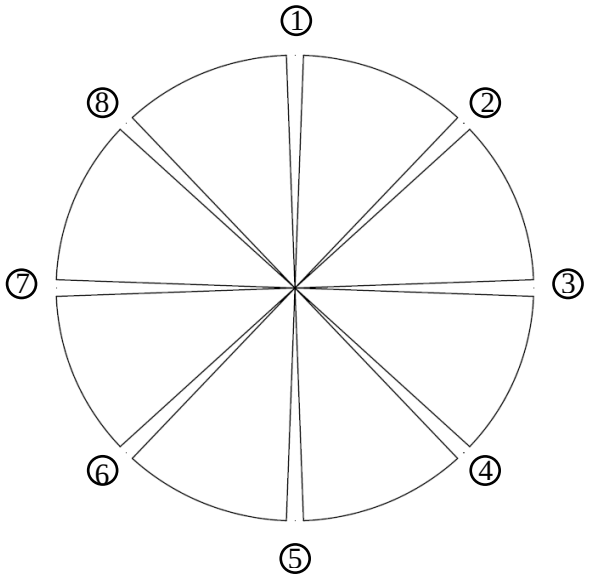

Figure 3.3: Eight wedging locations with corresponding sixteen faces of exposed wires.

openings in a cable's cross section (in this case r = 8). Every wedged opening exposes wires on two faces as shown in Figure 3.3. By performing this wedging operation, it becomes possible to visually identify and record the corrosion stage of every exposed wire on the $2r$ faces of the r wedged openings at each one of the N_i visual inspection locations along the length of the cable. The final outcome consists of $2r$ maps, each depicting the variation of the corrosion stage for all the exposed (visible) wires on a wedge face and along the entire length of the panel.

3.3 Spatial variation model for wires in the target panel

The length of each inspection location within a panel is denoted by L_i, with $L_i \approx L_p/N_i$. The reason for the approximation sign is that the inspection length L_i is not always constant, as it depends on various practical considerations (e.g. level of compaction of the cable, proximity to the cable bands, etc.). Each inspection length L_i is further subdivided into segments of length l_s = 18" (this is the standard ASTM testing length of steel wire specimens). The basic idea is that a different corrosion stage could be assigned in principle to each l_s segment. The outcome is that each inspection length L_i is subdivided into $N_{s_i} = L_i/l_s$ segments. Note again that the number of segments N_{s_i} is not constant for all the inspection locations because of the aforementioned approximation in L_i.

A specific example will be considered now for demonstration purposes. Consider that at a given inspection location, the length of the cable that has been wedged and visible (and consequently inspectable) is $L_i = 9$ ft. This means that there will be six ($N_{s_i} = 6$) 18" segments for each exposed wire that can be visually inspected and assigned a corrosion stage. Although each of the 6 individual wire segments could be assigned in principle a different corrosion stage, the segment with the worst corrosion stage is considered as representative of the entire $L_i = 9$ ft.

inspection length. For example, if the six 18" segments over the 9 ft. inspection length have been visually identified as: 1st segment: corrosion stage 2, 2nd segment: corrosion stage 2, 3rd segment: corrosion stage 3, 4th segment: corrosion stage 2, 5th segment: corrosion stage 1, and 6th segment: corrosion stage 3, then the following notation is used to identify them along the inspection length L_i:

2 – 2 – 3 – 2 – 1 – 3

while the entire inspection length L_i is assigned an overall corrosion stage of 3 (this is the segment with the worst corrosion stage among the six).

Note that the ability of visually identifying the distinct corrosion stages of all six segments depends on various practical parameters, the most important being physical accessibility for the inspector. When accessibility is difficult and/or compromised, it is possible that the inspector will not be able to provide a distinct corrosion stage classification for each one of the six segments. In such a case, the inspector identifies the worst corrosion stage along the entire 9 ft. length and applies it to all six segments. This means that, under this scenario, the six segments over the 9 ft. inspection length will be identified as:

3 – 3 – 3 – 3 – 3 – 3

Later on in this dissertation, the effects of corrosion stage variation along the length of wires is studied as part of a sensitivity analysis.

By repeating the aforementioned process at every inspection location within a panel for a specific wire, it is possible to determine its corrosion stage variation through the panel's entire length. The total number of l_s segments for this wire will obviously be: $N_{tot} = \sum_{i=1}^{N_i} N_{s_i}$, and there will be N_{tot} corresponding numerical values of different corrosion stages (ranging from 1 to 4).

Table 3.1: Simulated comprehensive corrosion stage wire profile in two dimensions: along the length of a cable panel and through the depth of its cross section (wire ring 1 is at the surface of the cable's cross section, while wire ring 46 is at the center of the cross section). These are all exposed wires from one side/face of a wedged opening.

Ring number	Corrosion stage variation of twenty 18" wire segments along the entire length of a panel																			
1	3	3	3	1	3	2	1	1	2	3	3	1	3	3	2	3	1	2	3	3
2	2	2	1	2	2	2	1	2	2	2	2	2	1	1	2	1	1	1	1	2
3	2	1	2	2	2	2	1	2	1	1	2	2	2	2	2	1	2	1	2	2
4	2	1	2	2	1	2	1	2	2	2	1	1	1	1	1	2	2	1	1	1
5	2	1	2	2	1	1	1	1	1	1	1	1	1	2	1	2	1	1	1	2
6	2	1	1	2	2	2	1	1	1	2	1	1	1	1	1	2	1	2	2	1
7	2	2	2	2	1	1	1	1	1	1	2	2	1	1	1	1	1	1	2	1
8	2	2	1	2	1	1	1	1	1	2	1	1	1	2	1	2	2	2	1	2
9	2	1	2	1	1	1	2	1	2	1	1	1	2	2	1	2	2	2	2	2
10	2	1	2	1	1	2	2	2	1	1	1	2	1	1	2	1	2	2	2	2
11	2	2	2	2	1	1	1	1	2	1	2	2	2	2	1	1	2	2	1	2
12	3	2	2	2	3	1	2	2	2	1	2	3	1	2	1	2	2	3	1	2
13	2	1	2	2	1	2	2	1	2	1	1	1	2	1	1	1	1	2	2	2
14	3	2	3	1	3	3	3	1	1	2	2	2	3	2	3	2	2	3	3	2
15	3	1	1	1	2	2	2	1	1	3	2	2	1	3	3	3	2	3	3	1
16	2	1	1	1	2	2	2	1	1	1	1	1	2	2	2	2	2	2	2	2
17	2	2	1	2	1	1	2	2	1	1	2	1	1	2	2	2	2	2	2	2
18	3	3	2	1	1	3	2	2	3	1	2	1	1	3	1	2	1	1	2	3
19	2	1	2	2	2	1	1	1	2	1	1	1	2	2	2	1	2	1	1	2
20	3	3	2	2	2	1	1	3	2	1	3	2	2	2	1	1	2	1	2	2
21	4	4	1	3	4	3	3	2	3	4	2	1	2	2	2	3	3	2	4	2
22	3	2	1	1	1	1	1	1	2	1	3	2	2	1	2	2	3	2	2	1
23	3	1	3	2	1	3	2	3	1	3	2	2	1	2	2	2	1	2	1	3
24	2	2	1	1	2	1	2	2	1	2	2	2	2	2	1	1	1	1	1	1
25	3	1	1	2	3	3	1	1	3	2	2	1	1	3	2	3	1	1	1	2
26	3	1	3	3	1	2	2	3	1	3	1	3	3	1	1	2	1	3	3	3
27	3	2	3	2	3	3	3	1	2	2	1	2	2	2	2	2	1	1	1	1
28	3	1	3	1	2	2	1	2	1	1	1	1	3	2	3	3	1	1	2	2
29	3	2	2	3	1	1	1	2	2	1	3	1	3	2	2	2	2	3	3	1
30	2	1	1	1	2	1	1	1	2	2	2	1	1	1	2	1	2	2	2	2
31	2	2	1	1	2	1	2	2	2	2	2	2	2	1	1	1	1	2	2	1
32	2	2	1	2	2	1	2	1	1	2	1	2	2	2	2	2	1	2	2	2
33	2	1	1	1	2	2	2	1	2	1	2	2	2	1	1	2	1	2	2	2
34	2	1	1	2	2	2	2	2	2	2	2	1	2	1	1	1	1	1	1	1
35	2	1	1	2	1	2	1	1	1	1	2	2	2	1	1	1	1	1	2	2
36	3	3	2	3	3	3	1	2	1	2	1	2	3	1	1	3	2	1	2	3
37	4	2	1	2	3	4	4	1	3	1	1	1	3	2	2	4	3	3	2	2
38	3	3	1	3	2	1	2	3	3	3	3	1	1	2	1	1	2	2	3	1
39	2	1	1	1	1	1	1	2	2	1	2	2	1	1	2	2	2	2	1	2
40	2	2	2	2	1	2	1	1	1	2	2	2	2	1	1	1	1	1	1	1
41	2	2	1	2	2	2	1	2	2	2	2	2	1	2	1	2	1	2	1	1
42	2	2	1	1	2	1	1	1	2	2	1	1	2	1	1	1	1	1	1	1
43	2	1	1	1	2	2	1	2	1	2	1	2	2	2	2	2	2	1	2	1
44	2	1	1	1	1	1	2	2	2	2	1	1	2	1	2	1	1	2	1	1
45	2	2	1	1	2	1	2	2	1	1	2	1	1	2	2	2	2	2	2	2
46	2	1	1	1	2	1	1	2	2	2	2	2	2	2	2	1	2	2	1	2

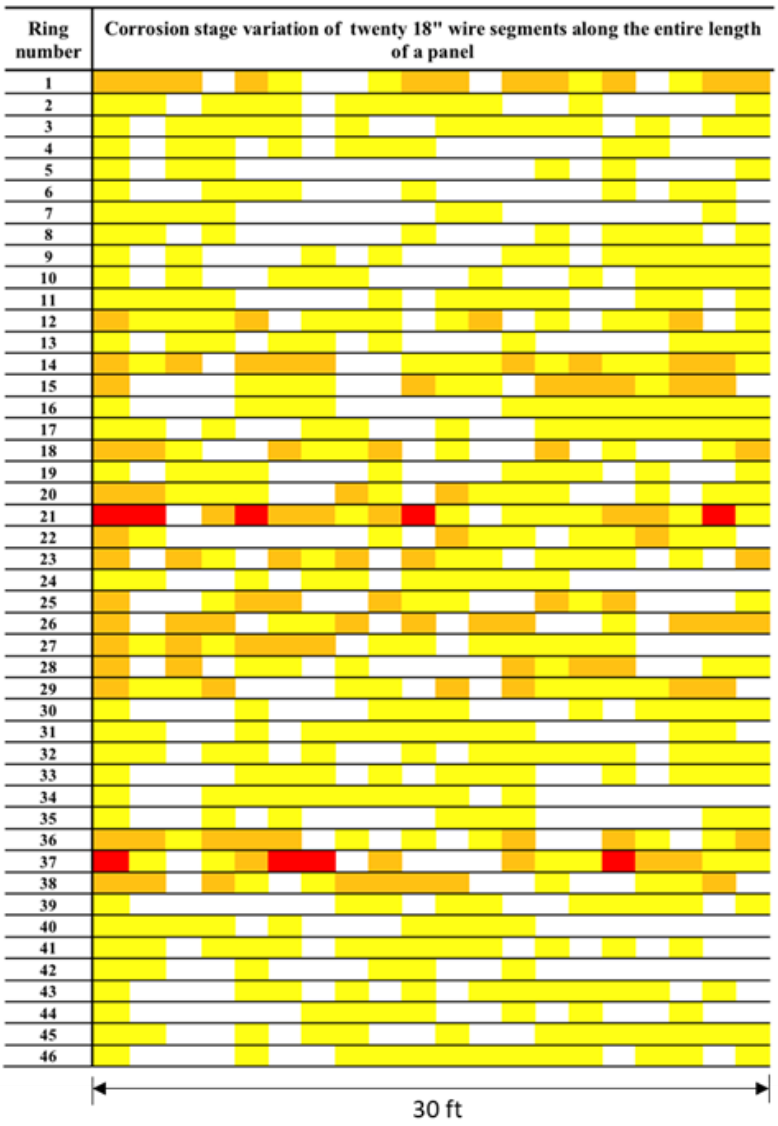

Figure 3.4: Color visualization of corrosion stage map shown in Table 3.1: simulated spatial variation of wire corrosion stage on one wedge face along the length of one panel (red indicates corrosion stage 4, orange indicates corrosion stage 3, yellow indicates corrosion stage 2, and white indicates corrosion stage 1).

Table 3.1 displays a simulated example of a corrosion stage map for all the exposed (visible) wires along the entire length of a panel. This cable has 46 wire rings ($N_r = 46$) with the first ring being on the outside circumference of the cable and the 46th ring located at the cable's center. The panel length consists of twenty ($N_{tot} = 20$) 18″ long segments (L_p is approximately 30′). This

corrosion stage map corresponds to one of the two faces of a wedged opening. Since for each wedged opening there are two faces (see Figure 3.3), there will be, in total, $2r$ corrosion stage maps for the cable (r is the number of wedged openings on the cable's cross-section). The corrosion stage map displayed in Table 3.1 using numbers to identify corrosion stages is visualized in color in Figure 3.4.

Even with eight wedges as shown in Figure 3.2, the majority of wires are still not visible (exposed) to the inspectors. The following assumption is made for the unexposed (hidden) wires: at any distance from the center of the cross section, all the wires in the corresponding half portion of the sector have the same corrosion stage variation as the wire exposed on the wedged surface.

For example, if a wire on a wedged opening, at a specific distance from the center of the cross section, has the following corrosion stage variation along the length of a panel:

3 – 3 – 3 – 1 – 3 – 3 – 2 – 1 – 1– 2 – 3 – 3 – 1 – 3 – 3 – 2 – 3 – 1 – 2 – 3

Then, all the wires behind it in the corresponding half of that sector at that same distance from the center of the cross section (same ring) will have the same corrosion stage variation. NCHRP Report 534 makes a similar assumption for the overall corrosion stage of a wire.

3.4 Comprehensive and overall corrosion maps of the cable cross section for an entire panel

At the end of this process, every wire within the cable cross section will have its corrosion stage variation along the entire length of the panel established deterministically. This 3-D model is called "comprehensive 3-D corrosion map of the cable cross section for the entire panel." In addition, each exposed wire (and those corresponding to its half sector ring) will be assigned an "overall corrosion stage label" defined as the worst corrosion stage found along its entire length

within the panel. For example, for the aforementioned wire with corrosion stage variation along the length of the panel:

3 – 3 – 3 – 1 – 3 – 3 – 2 – 1 – 1– 2 – 3 – 3 – 1 – 3 – 3 – 2 – 3 – 1 – 2 – 3

Its overall corrosion stage label will be 3. It is important to realize that numerous wires can be assigned the same overall corrosion stage label, but each wire will have its own different and specific corrosion stage variation along the length of the panel. A corrosion map based on overall corrosion stage labels is called an "overall 2-D corrosion map of the cable cross section for the entire panel."

Finally, all visually identified broken wires and their corresponding locations on the $2r$ exposed faces are recorded. Then, the number of hidden (unexposed) broken wires in the entire cross section is estimated using the simple proportionality rule proposed in NCHRP Report 534.

A representative example of an "overall 2-D corrosion map" (including broken wires) for a specific panel of an actual bridge is shown in Figure 3.5.

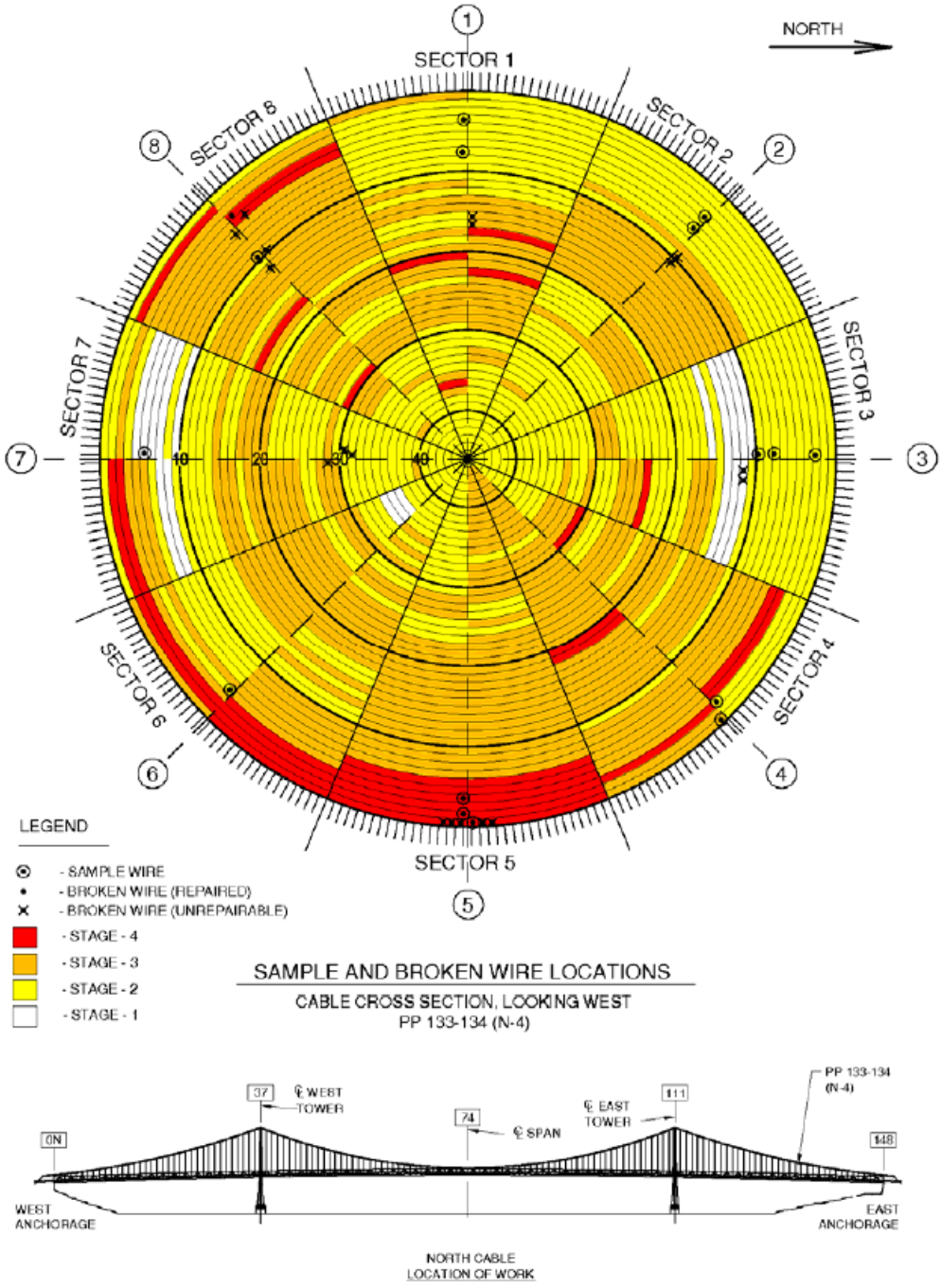

Figure 3.5: Overall 2-D corrosion map for panel PP133-134 of the Mid-Hudson Bridge (Modjeski and Masters, Inc. [20]).

Chapter 4 Estimation of Cable's Strength at a Given Panel

In this chapter, the ultimate strength of each wire in the cable's cross section is estimated, over the entire length of the panel. Although the 3-D corrosion map built in Chapter 3 is essentially deterministic, the estimation of the ultimate strength of one-panel-long wires will be stochastic, and will account for the corrosion stage variation of each wire along the entire panel length. Two steps are necessary to accomplish this objective: (1) establish the probability distribution function of the ultimate strength of wire segments of length l_s = 18" for each of the four different corrosion stages, using laboratory tensile tests of extracted wire specimens, and (2) estimate the ultimate strength of a wire of length equal to the length of an entire panel, $L_p = N_{tot} * l_s$. This long wire is composed of N_{tot} 18" segments of different corrosion stages that are known from the comprehensive 3-D corrosion map.

4.1 Ultimate strength of 18"-long wire segments

During a suspension bridge field inspection, long wire samples are removed from different panels, and different locations within a panel, brought to a laboratory, and cut into wire segments of length l_s = 18" (the long wire samples can extend over multiple neighboring inspection locations). Each of the 18" wire segments is classified into one of four groups based on their corrosion stages: Group 1 containing all the wire segments in stage 1, Group 2 containing all the wire segments in stage 2, Group 3 containing all the wire segments in stage 3 (cracked wires included), and Group 4 containing all the wire segments in stage 4 (cracked wires included). All 18" wire segments are then tested in the laboratory to determine their full stress-strain curve and resulting ultimate tensile strength σ_u^e (ASTM specifies that specimens for tensile testing must be

18" long).

In the proposed methodology, in contrast to NCHRP Report 534, cracked wires are not grouped in a separate category, but are kept within their original corrosion stage group determined from the visual inspection. The reason for this is that it is impossible during a field inspection to determine whether or not a wire of a given corrosion stage is cracked. The presence of cracked wires within a given corrosion stage group is accounted for in the estimated probability distribution function of the ultimate strength of the corresponding group.

Having tested an adequate number of wire segments of length l_s = 18" from each one of the four corrosion groups, it is straightforward to estimate empirical cumulative probability distribution functions for the ultimate strength of each corrosion group. Different distributions can be considered for the best fit to the empirical ones, including lognormal, Weibull and beta [4, 13, 21-25]. However, it is recommended to use directly the estimated empirical cumulative probability distribution functions, especially when testing data are limited.

4.2 Ultimate strength of wires over the entire length of a panel

The next step is the determination of the ultimate strength of a specific wire of length equal to one panel, using the wire's known corrosion stage variation over its length. A Monte Carlo simulation approach is used.

The corrosion stage wire profile, along the length of a cable panel and through the depth of its cross section, shown in Table 3.1, is used now to describe the steps of the Monte Carlo approach. For each one-panel-long wire consisting of twenty 18" segments in Table 3.1, values of the ultimate strength for each of its 20 segments are randomly generated, according to the corresponding estimated probability distributions described in the previous section. Specifically, for the long wire

in the 1st ring (first row) in Table 3.1, with corrosion stage variation of its segments:

3 – 3 – 3 – 1 – 3 – 3 – 2 – 1 – 1– 2 – 3 – 3 – 1 – 3 – 3 – 2 – 3 – 1 – 2 – 3

random values of the ultimate strength of each segment are generated according to the corresponding probability distributions. For the first segment, a random value is generated from the probability distribution of Group 3, as its ultimate strength. Then another random value is generated from the probability distribution of Group 3, as the ultimate strength of the second wire segment, and so on, until the ultimate strengths of all twenty segments of the long wire are generated.

To generate the random values of the ultimate strength of the 18" wire segments, based on the probability distributions developed for each group, the simple Inverse Transform Sampling [26] could be applied. As the current dissertation recommends to use empirical cumulative distribution functions (CDF's), standard interpolation schemes should be used to estimate values of the CDF in between data points. To briefly describe this approach, consider a wire segment of length l_s belonging in Group i (i=1, 2, 3 or 4), with a corresponding Cumulative Distribution Function (CDF) denoted as $F_i(x)$. The first step involves the generation of a random number, u, uniformly distributed in the interval [0, 1], i.e., $u \sim$ Uniform[0, 1]. This generated value u is then considered to be the value of the cumulative probability distribution $F_i(x)$. Finally, the corresponding inverse of the CDF $F_i(x)$ at u, denoted by $x = F_i^{-1}(u)$ can be easily computed. This value x will be the value of the strength of the wire segment of length l_s that follows the cumulative distribution function $F_i(x)$. Note that for the empirical CDFs, there is no continuous function, but only discrete points for $F_i(x)$. To apply the aforementioned method, linear interpolation can be used to get the value of $F_i^{-1}(u)$ between two data points. Figure 4.1 demonstrates schematically the implementation of the Inverse Transform Method for some wire segment group.

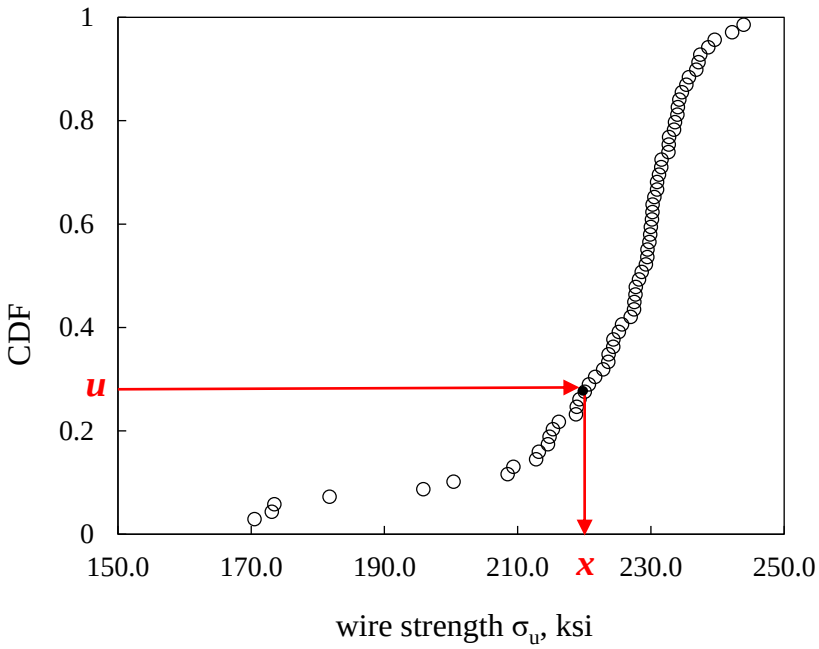

Figure 4.1: Implementation of Inverse Transform Method

Going back to the long wire in the 1st ring (first row) in Table 3.1, eventually $N_{tot} = 20$ ultimate strength values will be generated (one for each of its twenty segments). These twenty generated values constitute one "realization" of the one-panel-long wire. This realization of the one-panel-long wire will obviously fail at its weakest point, that is the minimum of the twenty generated ultimate strength values. Thus, the ultimate strength σ_u^{lw} of this specific realization of the one-panel-long wire is given by:

$$\sigma_u^{lw} = \min_{j=1,\ldots,N_{tot}} (\sigma_{u,j}^{e}) \tag{4.1}$$

This Monte Carlo simulation approach for estimating the ultimate strength of long wires (of length equal to one panel) can be applied to every single wire of the panel under consideration. The corresponding final result is one (random) "realization" of the ultimate strengths of all the wires in the panel.

The Monte Carlo approach described above fully accounts for the corrosion stage spatial variation of each and every wire in the cross section, along the entire length of the panel. This constitutes the main difference between the proposed methodology and the current methodology in NCHRP Report 534. Accounting for the corrosion stage spatial variation represents a significant improvement, as it takes into account a large amount of information that is simply disregarded in NCHRP Report 534. This is information that can have a large effect on the estimated overall cable strength as will be shown later.

It will be shown later, how one "realization" of the ultimate strengths of all the wires in the panel can be used to determine one "realization" of the overall cable strength of the given panel. It is extremely straightforward to generate multiple realizations of the ultimate strengths of all the wires in the panel, as well as the corresponding multiple realizations of the overall cable strength of the given panel. The ultimate outcome is the probability distribution function of the overall cable strength of the given panel.

It should be noted that, given the actual dimensions of suspension bridge main cables (thousands of wires and panels 30-40 ft. long), the numerical calculations involved in estimating the probability distribution of the overall cable strength could become expensive. A more efficient computational approach takes advantage of the assumption that all the wires in a half sector of a given ring are considered to have the same corrosion stage variation along their length. Following this assumption, the process of estimating the ultimate strength of one-panel-long wires is applied only to the wires on the exposed *2r* wedged surfaces. Then, all the wires behind the exposed ones in each corresponding half sector are assigned the same value for their ultimate strength as the corresponding exposed ones. This simplified approach is followed.

4.3 Redevelopment length for the strength of broken wires

It is generally recognized that a broken wire in a panel can regain its load carrying capacity and strength in adjacent panels because of friction with neighboring wires and the compaction provided by cable bands. Hence, it's necessary to account for the presence of broken wires in adjacent panels when estimating the ultimate strengths of a panel's wires. This is done by considering that wires which are broken in adjacent panels will have reduced ultimate strengths in the panel under examination.

Recent research on the contact model and friction mechanism among wires [5, 27-29] has provided interesting insights on these phenomena and shown that broken wires can recover their strength over relatively short distances. However, these studies have been limited in scope and constrained by experimental (e.g. maximum number of 19 wires) and/or computational (e.g. simplified FEM models) limitations. More research is needed to scale their results to large suspension bridge cables. To address this issue in a practical way, this dissertation uses conservative empirical knowledge based on the concept of redevelopment length (i.e. what is the required number of panels for a broken wire to regain its full strength).

The redevelopment length has been estimated during past inspections of suspension cables through the following observations and measurements. If a broken wire is perfectly clamped at its two adjacent cable bands so that no slipping occurs at these two locations, then the gap at its breaking location has to be equal to its elastic elongation between the two cable bands. In such a case, this wire would not have any loss of strength in adjacent panels. However, if the gap at the wire's breaking location is larger than the elastic elongation, this means that the broken wire has slipped at the cable bands at the two ends of its panel and can only regain its strength after multiple cable bands (i.e. over multiple panels) through the clamping action of the cable bands.

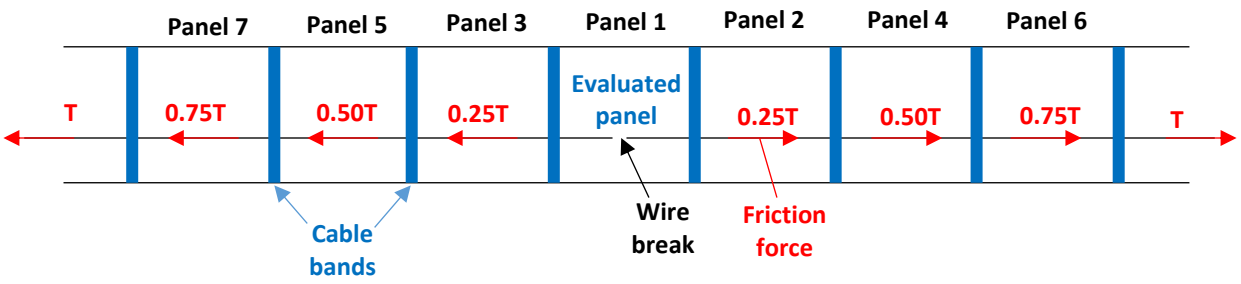

Figure 4.2: Redevelopment length: demonstration of how a broken wire in Panel 1 regains its full strength T as it goes through adjacent cable bands.

In this dissertation, the estimation of the redevelopment length for broken wires follows the same guidelines as those described in NCHRP Report 534 (Articles 4.5.1-4.5.2). Typically, the redevelopment length is equivalent to 7 panels (including the evaluated panel), with three panels on each side of the evaluated one. In different words, broken wires within a panel regain their full strength after three panels from each side. This means that each cable band contributes to redevelop 25% of the broken wire's full strength. The redevelopment length is visually demonstrated in Figure 4.2 and the corresponding concept of redevelopment factor is defined in Table 4.1.

Table 4.1: Definition of redevelopment factor C_{di} (as in NCHRP Report 534). Panel numbers are defined in Figure 4.2.

Panel number *i*	1	2 & 3	4 & 5	6 & 7
C_{di}	0	0.25	0.50	0.75

Let's denote the total number of wires in the cable cross section by N_{all}. Referring to Figure 4.2, the panel under investigation/inspection is Panel 1, with N_{b1} denoting the total number of broken wires in the panel. N_{b1} includes observed broken wires as well as estimated hidden broken wires obtained following the approach in NCHRP Report 534 (Articles 4.3.3.1 - 4.3.3.3). The

estimated hidden broken wires are removed at random, but keeping the same proportions in the four corrosion stages as those for the observed broken wires.

Assuming now that all the other panels within the redevelopment length in Figure 4.2 are also inspected, let's denote by $N_{bi}, i = 2,3, \ldots,7$ the total number of broken wires in the i-th panel (including again observed broken wires and estimated hidden broken wires).

The wires broken in panels 2 and 3 will regain/redevelop 25% of their full ultimate strength in panel 1. These $(N_{b2} + N_{b3})$ wires are identified within panel 1 by random selection (representative of panel 1 and keeping the same proportions of corrosion stages as those of the broken wires in panels 2 and 3) and their ultimate strengths are multiplied by $C_{d2,3} = 0.25$.

The wires broken in panels 4 and 5 will regain/redevelop 50% of their full ultimate strength in panel 1. These $(N_{b4} + N_{b5})$ wires are identified within panel 1 by random selection (representative of panel 1 and keeping the same proportions of corrosion stages as those of the broken wires in panels 4 and 5) and their ultimate strengths are multiplied by $C_{d4,5} = 0.50$.

Finally, the wires broken in panels 6 and 7 will regain/redevelop 75% of their full ultimate strength in panel 1. These $(N_{b6} + N_{b7})$ wires are identified within panel 1 by random selection (representative of panel 1 and keeping the same proportions of corrosion stages as those of the broken wires in panels 6 and 7) and their ultimate strengths are multiplied by $C_{d6,7} = 0.75$.

At the end of this process, the following modifications would be implemented on certain wires in the panel under consideration/inspection (panel 1): $(N_{b2} + N_{b3})$ wires will have their realized ultimate strength reduced by 75%, $(N_{b4} + N_{b5})$ wires will have their realized ultimate strength reduced by 50%, and $(N_{b6} + N_{b7})$ wires will have their realized ultimate strength reduced by 25%. The remaining number of wires, N_{rem}:

$$N_{rem} = N_{all} - N_{b1} - (N_{b2} + N_{b3}) - (N_{b4} + N_{b5}) - (N_{b6} + N_{b7}) \quad (4.2)$$

will experience no modification in their original realized ultimate strength.

This new modified set of values for the ultimate strengths of the panel's wires is the final one, and accounts for both the spatial variation of wire strength along the length of the panel and the effects of broken wires in neighboring panels.

4.4 Incremental loading process to estimate overall cable strength

The final set of values for the ultimate strengths of a panel's wires (as described in the previous section), in combination with an incremental loading procedure, are used to determine the strength of the cable at a given panel.

The proposed methodology will be an iterative process where, at each load step, the load carried by each wire is checked against the wire's ultimate strength. For the effective wires that are not broken throughout the redevelopment length (i.e. N_{rem} in Eq. (4.2)), if such a load exceeds the wire's strength, the wire is removed and the number of effective wires is updated. For the broken wires in adjacent panels (i.e. $N_{bi}, i = 2, 3, \dots, 7$ in Eq. (4.2)), they can redevelop part of their strength because of friction between wires. Therefore, once the load exceeds the redeveloped strength, the wire will not be removed from the calculation and its strength will remain constant till the end of the iterative process. This process will stop when the remaining wires will not be able to carry the applied load. At this point, we can define as the cable overall strength the maximum load calculated during the iteration process. By repeating this process for different realizations of values for the ultimate strengths of the panel's wires, it is possible to produce a large number of realizations for the cable's overall strength. These values are used to establish the empirical probability distribution function of the cable's overall strength.

The steps to calculate one random realization of the overall strength of the cable at a given panel (denoted by R_u) are outlined below:

1) Randomly generate realizations for the ultimate strengths of all the cable's wires over the length of the panel and properly account for broken wires (this step has already been described in earlier sections).

2) Start from an initial value for the applied force on the cable (denoted by F_0). The value of F_0 has to be low enough to avoid immediate complete cable failure. A good value for F_0 is the load carried by the cable under service load conditions.

3) Compute an average stress s_0:

$$s_0 = \frac{F_0}{A_{eff}} \tag{4.3}$$

where A_{eff} is the product of the nominal area of a single wire, a_w, multiplied by the total number of effective wires, N_{eff}: $A_{eff} = a_w \times N_{eff}$. The term "effective wires" indicates those wires in the cross section that have not failed at the current iteration (i.e. wires that are still able to carry their corresponding load and have not been removed in previous iterations). At the first load step: $N_{eff} = N_{all} - N_{b1}$ (refer to Equation (4.2)).

4) Compare the value of s_0 in Equation (4.3) to all the ultimate strength values of the effective wires, σ_u^{lw} (refer to Equation (4.1) for the definition of σ_u^{lw}). For effective wires not broken throughout the redevelopment length (N_{rem} in Eq. (4.2)), if there are values of the wire ultimate strengths that are less than s_0, then the corresponding wires are eliminated. For wires broken in the redevelopment length, if the redeveloped strength is less than s_0, then the wire strength will be set equal to the redeveloped strength and will remain constant throughout the entire loading process. To highlight these two contributions, the overall load T carried

by the cable can be decomposed into two parts: 1) One component is the load carried by the effective wires ((denoted by T_u), and 2) the component carried by the wires broken in the redevelopment length (denoted by R_b), i.e.

$$T = T_u + R_b \tag{4.4}$$

where:

$$T_u = s_0 \cdot a_w \cdot N'_{eff} \tag{4.5}$$

with N'_{eff} the total number of effective wires that do not fail under a stress s_0 (at the first iteration, it is expected that $N'_{eff} = N_{eff} = N_{all} - N_{b1}$)

The second contribution to the cable strength, R_b, can be obtained as:

$$R_b = s_0 \cdot a_w \cdot N_{b,\geq s} + R_{b,<s} \tag{4.6}$$

where $N_{b,\geq s}$ is the total number of broken wires in the redevelopment length whose strength is larger than s_0. The component $R_{b,<s}$ represents the total force provided by the wires broken in the redevelopment length whose strength is less than s_0 and hence they will keep their strength constant regardless of the increasing load. Thus, $R_{b,<s}$ can be expressed as:

$$R_{b,<s} = a_w \cdot \sum_{j=1}^{n} s_{bj} \tag{4.7}$$

with s_{bj} indicating the redeveloped strength of the j-th broken wire and n being the total number of broken wires whose redeveloped strength is less than s_0.

5) At this point, consider an increase in the cable force by applying an arbitrary small increment in stress (Δs) and consider the new wire stress level as:

$$s_1 = s_0 + \Delta s \tag{4.8}$$

Replace s_0 with s_1 in step 4 and update the N'_{eff}, $N_{b,\geq s}$ and $R_{b,<s}$ according to the strength map. So, the new cable force

$$T_1 = T_{u1} + R_{b1} \tag{4.9}$$

6) Repeat steps 4 and 5 until, at the i-th iteration, the corresponding s_i will be greater than the ultimate strength of all the remaining long effective wires ($\sigma_u^{lw} < s_i$ for every effective wire in the cross section). This means that, at that applied force level, all wires in the cross section fail. This is equivalent to failure of the entire cable.

7) With the series of (s_i, T_i), the curve of incremental loading can be obtained. The overall cable strength is the maximum point of the curve, which can be simply determined by

$$R_u = \max_{1\leq k\leq i}(T_k) \tag{4.10}$$

The 7-step procedure described above yields one random realization of the overall strength of the cable at a given panel. To establish the statistics of the overall cable strength, the 7-step procedure has to be repeated a large number of times N_{MC} (every time with a different set of realizations for the ultimate strengths of all the cable's wires over the length of the panel). These N_{MC} values for R_u are used to establish the empirical probability distribution of the cable's overall strength for the panel under consideration (as well as its mean, standard deviation, percentiles, etc.).

Chapter 5 Application of the Methodology to Suspension Bridges

This chapter includes two case studies: Franklin Delano Roosevelt Mid-Hudson Bridge and Bear Mountain Bridge. In the case of Mid-Hudson bridge, simulated inspection information on corrosion stages variation along wires is applied, as an illustration of proposed methodology. In case of Bear Mountain Bridge, inspection information at site is provided, including the corrosion variations observed at three inspection locations. And a comprehensive comparison with current standard methods is also carried out.

5.1 Case 1: Franklin Delano Roosevelt Mid-Hudson Bridge

The proposed methodology is applied to the Franklin Delano Roosevelt Mid-Hudson Bridge in New York State in order to evaluate the strength of its cables. All relevant information comes from the bridge's inspection conducted in 2009 by Modjeski and Masters, Inc.[20].

5.1.1 Bridge cable inspection information

Each of the main cables of the Mid-Hudson Bridge consists of 19 wire strands, each strand composed of 320 wires, for a total of 6,080 wires per cable ($N_{all} = 6{,}080$). All main cable wires are No. 6 gauge galvanized (0.196" nominal diameter, 0.192" diameter prior to galvanizing), cold-drawn, with a specified minimum tensile strength of 215 ksi. In this example, panel PP133-134 is the target panel selected for evaluation (see Figure 3.5). During the 2009 inspection, it was found that this panel had 3.4% of its wires in corrosion stage 1, 42.1% in corrosion stage 2, 46.5% in corrosion stage 3, and 8.0% in corrosion stage 4. A total of 122 long wire samples, ranging in length from 9.5 ft. to 12 ft., were removed from the cable for laboratory testing. The extracted

samples were cut into 18" segments (l_s = 18") for tensile testing. Overall, there were three 18" segments in stage 1 (that were tested), 100 in stage 2, 211 in stage 3, and 68 in stage 4.

There were also 18 observed broken wires, with 2 of them classified in corrosion stage 1, 2 in stage 2, 8 in stage 3, and 6 in stage 4. Following the proportionality guidelines in NCHRP Report 534, the estimated total number of broken wires in the entire cross section (observed + hidden) would be 139 ($N_{b1} = 139$), with 15 in corrosion stage 1, 15 in corrosion stage 2, 63 in corrosion stage 3, and 46 in corrosion stage 4. The effective wires in panel PP133-134 would be $N_{eff} =$ 6,080 - 139 = 5,941. The actual locations of the observed broken wires can be seen in Figure 3.5.

Note that the corrosion stage variation along the length of the wires was not part of this 2009 inspection program. Hence, to illustrate the proposed methodology, comprehensive corrosion maps (describing the corrosion stage variation along the entire length of wires in the panel) have been numerically simulated to match and reflect the overall corrosion map that was observed and recorded during the inspection. For example, the simulated comprehensive corrosion map for the left side of wedged sector 1 (refer to Figure 3.2), is shown in Table 3.1. The remaining 15 comprehensive corrosion maps are simulated in the same way (but are not shown because of space limitations).

5.1.2 Cable strength evaluation

Figure 5.1(a)-(c) displays the empirical CDF's of the ultimate strength of 18" wire segments belonging to corrosion stages 2, 3 and 4, established using laboratory test data from extracted wires during the inspection of the Mid-Hudson Bridge. As corrosion stage 1 has only three experimental data points, its CDF is not computed.

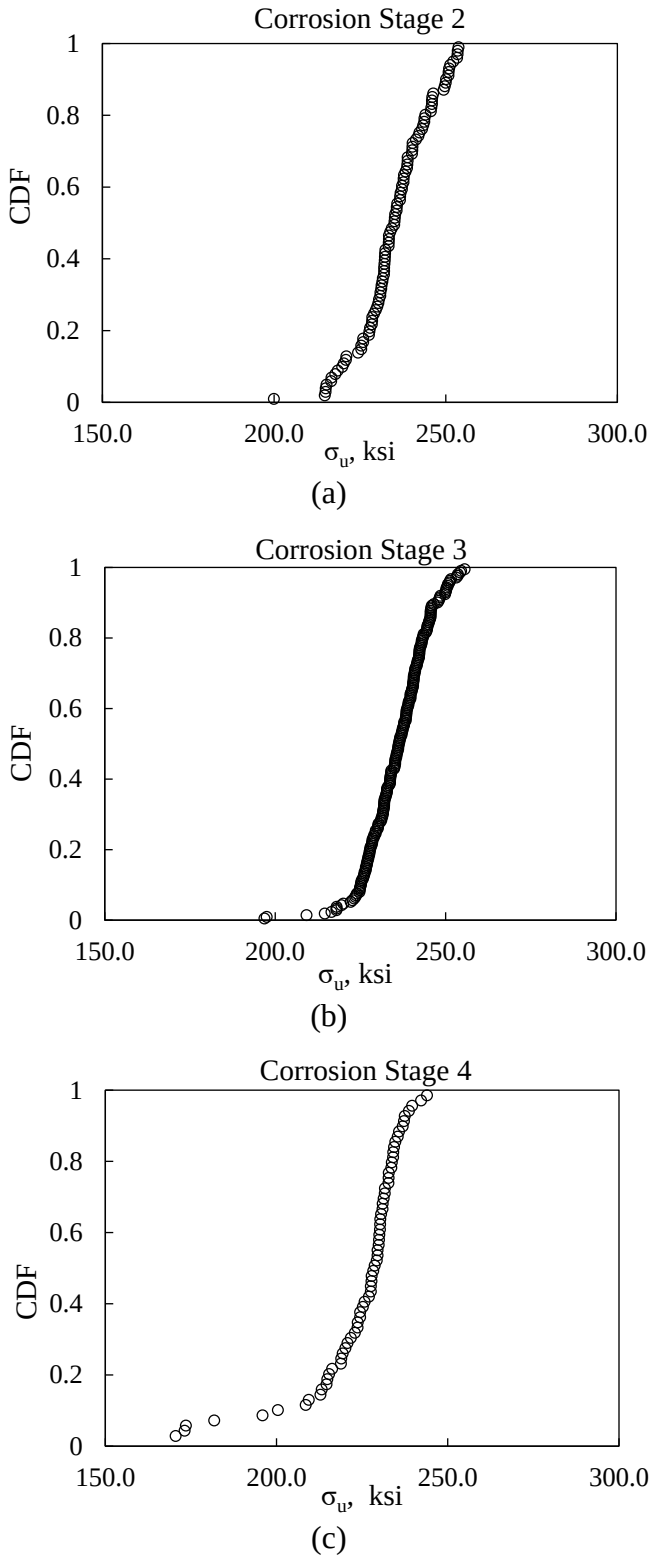

Figure 5.1: Empirical CDF's of the ultimate strength of 18" wire segments belonging to corrosion stage 2 (a), 3 (b) and 4 (c), established using actual laboratory data from extracted wires from the inspection of the Mid-Hudson Bridge.

Combining now the CDF's of the corrosion groups in Figure 5.1, with the simulated comprehensive corrosion maps (like the one displayed in Table 3.1) one random realization for the ultimate stress σ_u^{lw} of each of the one-panel-long wires in the cross section can be eventually generated, as described in Section 4.2. In addition, each of the cross section's 6,080 wires will be assigned an overall corrosion stage (the worst corrosion stage among its 18" wire segments).

To account for the effect of broken wires in adjacent panels, the redevelopment length (Section 4.3) is considered to be equal to 7 panels (including the evaluated panel), with three panels on each side of the evaluated one. Section 4.3 made the assumption that all 7 panels were inspected. This was not the case with the Mid-Hudson Bridge where only the evaluated panel was inspected. Because of the lack of inspection of the six neighboring panels, it is assumed here that all 7 panels contain the same number of broken wires as that in the evaluated panel PP133-134, i.e.,

$$N_{b1} = N_{b2} = N_{b3} = N_{b4} = N_{b5} = N_{b6} = N_{b7} = 139$$

It is further assumed that in all 7 panels, the proportion of broken wires in each corrosion stage is the same as the corresponding one in the evaluation (inspected) panel. Denoting with $N_{bi,j}$ the number of broken wires in the *i*-th panel that are assigned to the *j*-th corrosion stage group, the following relations hold:

$$N_{b1,1} = N_{b2,1} = N_{b3,1} = N_{b4,1} = N_{b5,1} = N_{b6,1} = N_{b7,1} = 15$$

$$N_{b1,2} = N_{b2,2} = N_{b3,2} = N_{b4,2} = N_{b5,2} = N_{b6,2} = N_{b7,2} = 15$$

$$N_{b1,3} = N_{b2,3} = N_{b3,3} = N_{b4,3} = N_{b5,3} = N_{b6,3} = N_{b7,3} = 63$$

$$N_{b1,4} = N_{b2,4} = N_{b3,4} = N_{b4,4} = N_{b5,4} = N_{b6,4} = N_{b7,4} = 46$$

The procedure for the evaluation of the entire cable strength continues as follows. For each one of the four corrosion stage groups (*j*=1, 2, 3, 4), $N_{b1,j}$ wires are removed from the evaluation panel's cable cross section. Note that $N_{b1,j}$ includes observed and hidden broken wires. The

observed broken wires are of course removed from their actual locations within the cross section. The locations of the hidden broken wires are randomly selected among the totality of hidden wires, keeping the same proportions in the four corrosion stages as those for the observed broken wires. This wire removal is accounted for by multiplying the ultimate strengths σ_u^{lw} of the $N_{b1,j}$ broken wires by 0.

The next step involves the random selection, within the evaluation panel, of $(N_{b2,j} + N_{b3,j})$ wires from the remaining wires in the *j*-th group (*j*=1, 2, 3, 4), and multiplying their ultimate strengths σ_u^{lw} by 0.25: this means that the $(N_{b2,j} + N_{b3,j})$ wires broken in the two adjacent panels 2 and 3 (refer to Figure 4.2), have only 25% of their ultimate strength in the evaluation panel (in other words, they have recovered only 25% of their ultimate strength in the evaluation panel). Then, randomly select within the evaluation panel, $(N_{b4,j} + N_{b5,j})$ wires from the remaining wires in the *j*-th group (*j*=1, 2, 3, 4), and multiply their ultimate strengths σ_u^{lw} by 0.50: this means that the $(N_{b4,j} + N_{b5,j})$ wires broken in panels 4 and 5 have only 50% of their ultimate strength in the evaluation panel (in other words, they have recovered only 50% of their ultimate strength in the evaluation panel). Finally, to account for broken wires in panels 6 and 7, randomly select within the evaluation panel, $(N_{b6,j} + N_{b7,j})$ wires from the remaining wires in the *j*-th group (*j*=1, 2, 3, 4), and multiply their ultimate strengths σ_u^{lw} by 0.75: this means that the $(N_{b6,j} + N_{b7,j})$ wires broken in panels 6 and 7 have 75% of their ultimate strength in the evaluation panel (in other words, they have recovered 75% of their ultimate strength in the evaluation panel).

For example, considering corrosion stage group 3 that has 63 broken wires in each of the seven panels, the procedure described in the previous two paragraphs goes as follows:

1) Within the cross-section of the evaluation panel, identify 63 wires among those in corrosion stage 3 (either considering the actual locations of observed broken wires in corrosion stage 3

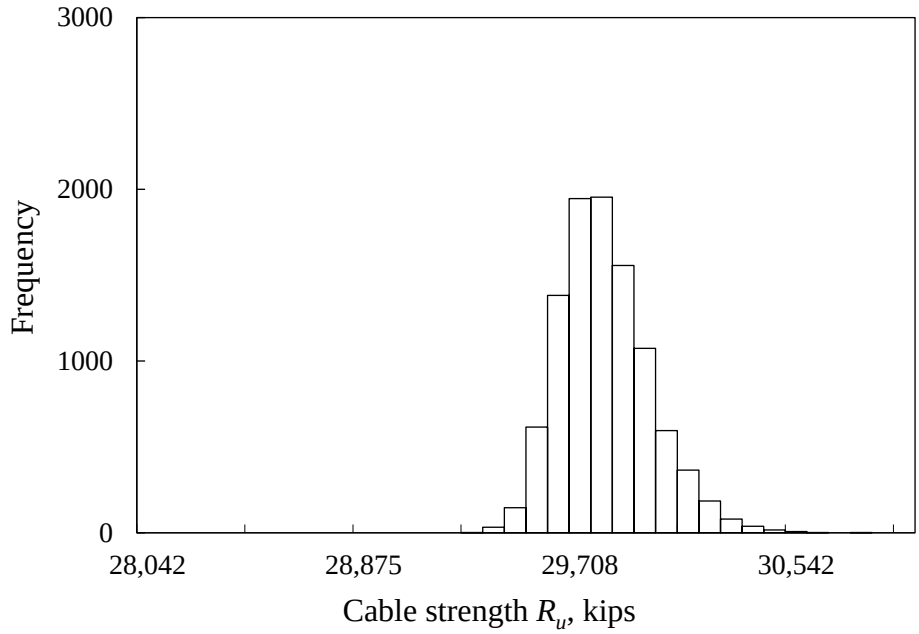

Figure 5.2: Histogram of 10,000 simulated values of the overall cable strength of the FDR Mid-Hudson Bridge using the proposed methodology

or randomly among the hidden wires in corrosion stage 3), and multiply the values of their ultimate strengths by 0,

2) Within the cross-section of the evaluation panel, randomly select 2*63=126 wires among those remaining in corrosion stage 3, and multiply their ultimate strengths by 0.25,
3) Within the cross-section of the evaluation panel randomly select 2*63=126 wires among those remaining in corrosion stage 3, and multiply their ultimate strengths by 0.50,
4) Within the cross-section of the evaluation panel randomly select 2*63=126 wires among those remaining in corrosion stage 3, and multiply their ultimate strengths by 0.75.

At the end of the 4-step process described above for the four corrosion stages, the evaluation panel will contain 6,080 – 139 = 5941 unbroken wires, but the ultimate stress σ_u^{lw} of some of them would have been appropriately reduced to account for the presence of broken wires in the neighboring six panels (three from each side of the evaluation panel). At this point, the 7-step

procedure described in Section 4.4 is used to calculate one random realization of the overall strength of the cable, R_u, at the evaluation panel.

To establish the statistics of the overall cable strength of the Mid-Hudson Bridge, the 7-step procedure in Section 4.4 is repeated 10,000 times. Figure 5.2 plots the resulting histogram from these 10,000 simulated values of R_u. The values for the cable strength range from 29,323 kips to 30,784 kips, with a mean value of 29,805 kips and a standard deviation of 174 kips. Figure 5.2 indicates that the probability distribution of the overall cable strength R_u is slightly skewed and very smooth. Other statistics that can be estimated for R_u include median, mode, various percentiles, skewness, kurtosis, etc.

5.2 Case 2: Bear Mountain Bridge

5.2.1 Bridge cable inspection information

Each of the main cables of Bear Mountain Bridge consists of 37 strands, each composed of 196 wires, for a total of 7,252 wires per cable. ($N_{all} = 7{,}252$). Panel PP 2-3W is the target panel selected for evaluation. During the inspection, it was found that this panel had 95% in corrosion stage 2, 4% in corrosion stage 3, and 1% in corrosion stage 4, which indicated that the cable is in a good condition. A total of 54 long wire samples were removed from the cable for laboratory testing and then cut into 18" segments. Overall, there were 27 segments tested in stage 1, 78 in stage 2, 123 in stage 3, and 124 in stage 4. There were also 86 observed broken wires within the panel, with 82 of them classified in corrosion stage 2, 3 in stage 3, and 1 in stage 4.

The inspection on corrosion stage variations along the wires is carried out at three locations throughout the panel. Table 5.1 is the corrosion map for the left side of wedged sector 1 and Figure 5.3 is the corrosion map for the cross section, where the locations of broken wires are also reflected.

Table 5.1: Spatial variation of wire corrosion stage of one panel observed at three inspection locations denoted by three different colors.

Ring number	Corrosion stage variation of twenty 18″ long wire segments along the entire length of a panel																	
1	2	2	2	2	2	2	2	2	2	2	2	2	2	2	2	2	2	2
2	1	1	1	1	1	1	2	2	2	2	2	2	2	2	2	2	2	2
3	1	1	1	1	1	1	2	2	2	2	2	2	2	2	2	2	2	2
4	1	1	1	1	1	1	1	1	1	1	1	1	2	2	2	2	2	2
5	1	1	1	1	1	1	1	1	1	1	1	1	2	2	2	2	2	2
6	1	1	1	1	1	1	1	1	1	1	1	1	2	2	2	2	2	2
7	1	1	1	1	1	1	2	2	2	2	2	2	2	2	2	2	2	2
8	1	1	1	1	1	1	2	2	2	2	2	2	2	2	2	2	2	2
9	1	1	1	1	1	1	1	1	1	1	1	1	2	2	2	2	2	2
10	1	1	1	1	1	1	1	1	1	1	1	1	2	2	2	2	2	2
11	1	1	1	1	1	1	1	1	1	1	1	1	2	2	2	2	2	2
12	1	1	1	1	1	1	1	1	1	1	1	1	2	2	2	2	2	2
13	1	1	1	1	1	1	1	1	1	1	1	1	2	2	2	2	2	2
14	1	1	1	1	1	1	1	1	1	1	1	1	2	2	2	2	2	2
15	1	1	1	1	1	1	1	1	1	1	1	1	2	2	2	2	2	2
16	1	1	1	1	1	1	1	1	1	1	1	1	2	2	2	2	2	2
17	1	1	1	1	1	1	2	2	2	2	2	2	2	2	2	2	2	2
18	1	1	1	1	1	1	1	1	1	1	1	1	2	2	2	2	2	2
19	1	1	1	1	1	1	1	1	1	1	1	1	2	2	2	2	2	2
20	1	1	1	1	1	1	1	1	1	1	1	1	2	2	2	2	2	2
21	1	1	1	1	1	1	1	1	1	1	1	1	2	2	2	2	2	2
22	1	1	1	1	1	1	2	2	2	2	2	2	2	2	2	2	2	2
23	1	1	1	1	1	1	2	2	2	2	2	2	2	2	2	2	2	2
24	1	1	1	1	1	1	2	2	2	2	2	2	2	2	2	2	2	2
25	1	1	1	1	1	1	2	2	2	2	2	2	2	2	2	2	2	2
26	1	1	1	1	1	1	2	2	2	2	2	2	2	2	2	2	2	2
27	1	1	1	1	1	1	2	2	2	2	2	2	2	2	2	2	2	2
28	1	1	1	1	1	1	2	2	2	2	2	2	2	2	2	2	2	2
29	1	1	1	1	1	1	2	2	2	2	2	2	2	2	2	2	2	2
30	1	1	1	1	1	1	2	2	2	2	2	2	2	2	2	2	2	2
31	2	2	2	2	2	2	2	2	2	2	2	2	2	2	2	2	2	2
32	2	2	2	2	2	2	2	2	2	2	2	2	2	2	2	2	2	2
33	2	2	2	2	2	2	2	2	2	2	2	2	2	2	2	2	2	2
34	2	2	2	2	2	2	2	2	2	2	2	2	2	2	2	2	2	2
35	2	2	2	2	2	2	2	2	2	2	2	2	2	2	2	2	2	2
36	2	2	2	2	2	2	2	2	2	2	2	2	2	2	2	2	2	2
37	2	2	2	2	2	2	2	2	2	2	2	2	2	2	2	2	2	2
38	2	2	2	2	2	2	2	2	2	2	2	2	2	2	2	2	2	2
39	2	2	2	2	2	2	2	2	2	2	2	2	2	2	2	2	2	2
40	2	2	2	2	2	2	2	2	2	2	2	2	2	2	2	2	2	2
41	2	2	2	2	2	2	2	2	2	2	2	2	2	2	2	2	2	2
42	2	2	2	2	2	2	2	2	2	2	2	2	2	2	2	2	2	2
43	2	2	2	2	2	2	2	2	2	2	2	2	2	2	2	2	2	2
44	2	2	2	2	2	2	2	2	2	2	2	2	2	2	2	2	2	2
45	2	2	2	2	2	2	2	2	2	2	2	2	2	2	2	2	2	2
46	2	2	2	2	2	2	2	2	2	2	2	2	2	2	2	2	2	2
47	2	2	2	2	2	2	2	2	2	2	2	2	2	2	2	2	2	2
48	2	2	2	2	2	2	2	2	2	2	2	2	2	2	2	2	2	2
49	2	2	2	2	2	2	2	2	2	2	2	2	2	2	2	2	2	2

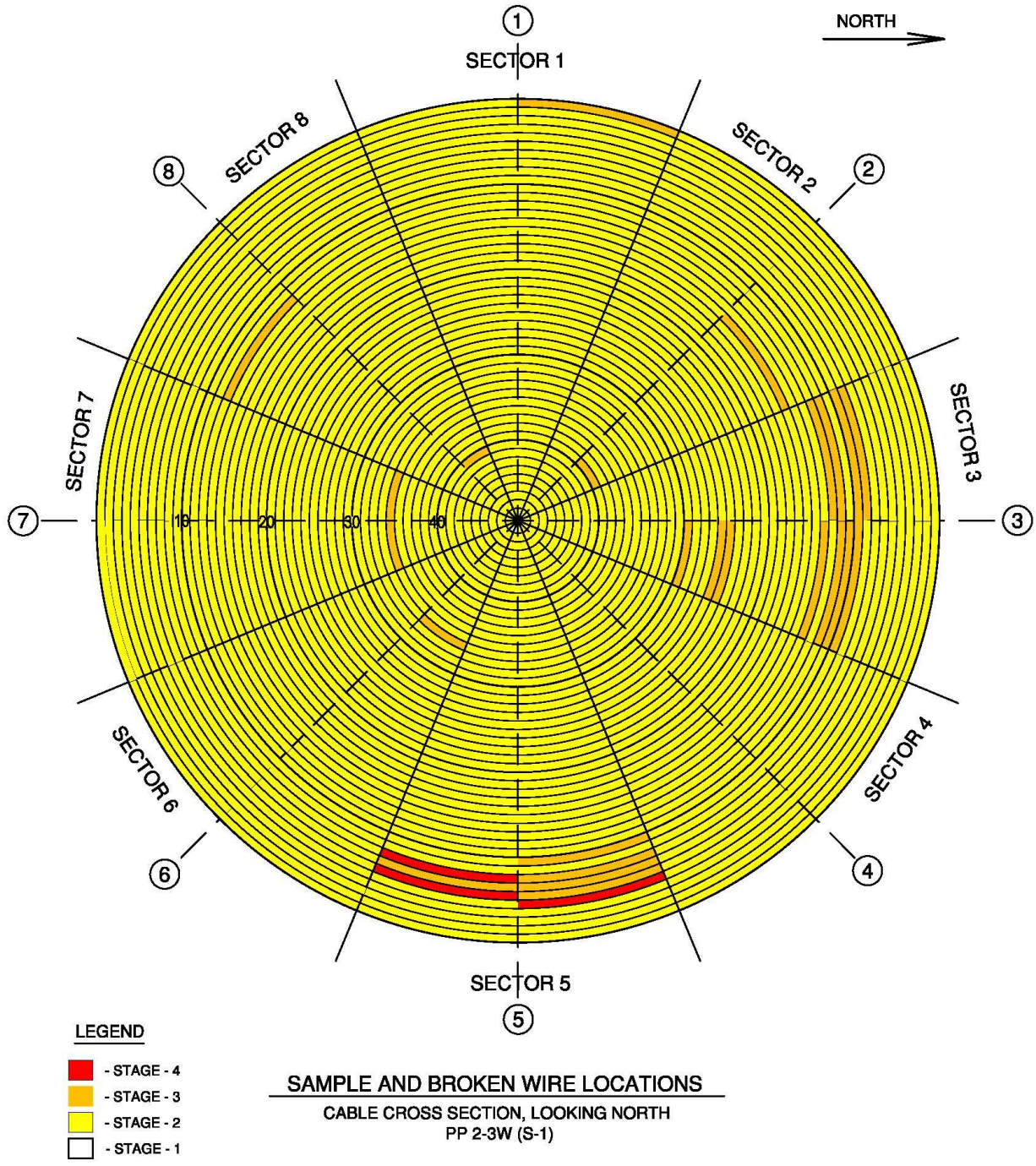

Figure 5.3: Corrosion map of the cross section of PP 2-3W of Bear Mountain Bridge (Modjeski and Masters, Inc. [30])

5.2.2 Cable strength evaluation

Probability distributions of the four corrosion stages are constructed based on laboratory testing data. Figure 5.4(a)-(d) shows the empirical CDFs of four corrosion groups, which are used, together with observations of corrosion variations along the wire in Table 5.1, to generate ultimate stress $\sigma_{u,l}$ samples of the 7,252 wires by Monte Carlo simulation approach.

For broken wires, following the guidelines in NCHRP Report 534, the estimated total number of broken wires within the panel is 635. Therefore, the effective wires in panel PP 2-3W would be 7,252 - 635 = 6,617. Because of the lack of inspection on adjacent panels, it's assumed that all the 7 panels contain the same number of broken wires (and same corrosion stages) as in the evaluated panel PP 2-3W, i.e., there are 635 broken wires in each of the 7 panels. For the 6 adjacent panels, the redevelopment of a fraction of the ultimate wire strength is considered, following the approach described in Section 4.3.

At the end of this process, all the wires in the cross-section representative of panel PP 2-3 W will have their ultimate strength. There are still 6,617 effective wires (that contribute to the overall global cable strength) but, for some of them, the original ultimate stress $\sigma_{u,l}$ has been reduced to account for the presence of broken wires in the neighboring panels. At this point, the incremental loading procedure to estimate the ultimate strength of the entire cable can be carried out and the overall cable strength R_u for this realization can be obtained.

Table 5.2 is the result of 10000 realizations Monte Carlo simulations for R_u. The cable strength ranges from 24,668 kips to 24,836 kips with the mean value of 24,750 kips, and standard deviation of 21 kips.

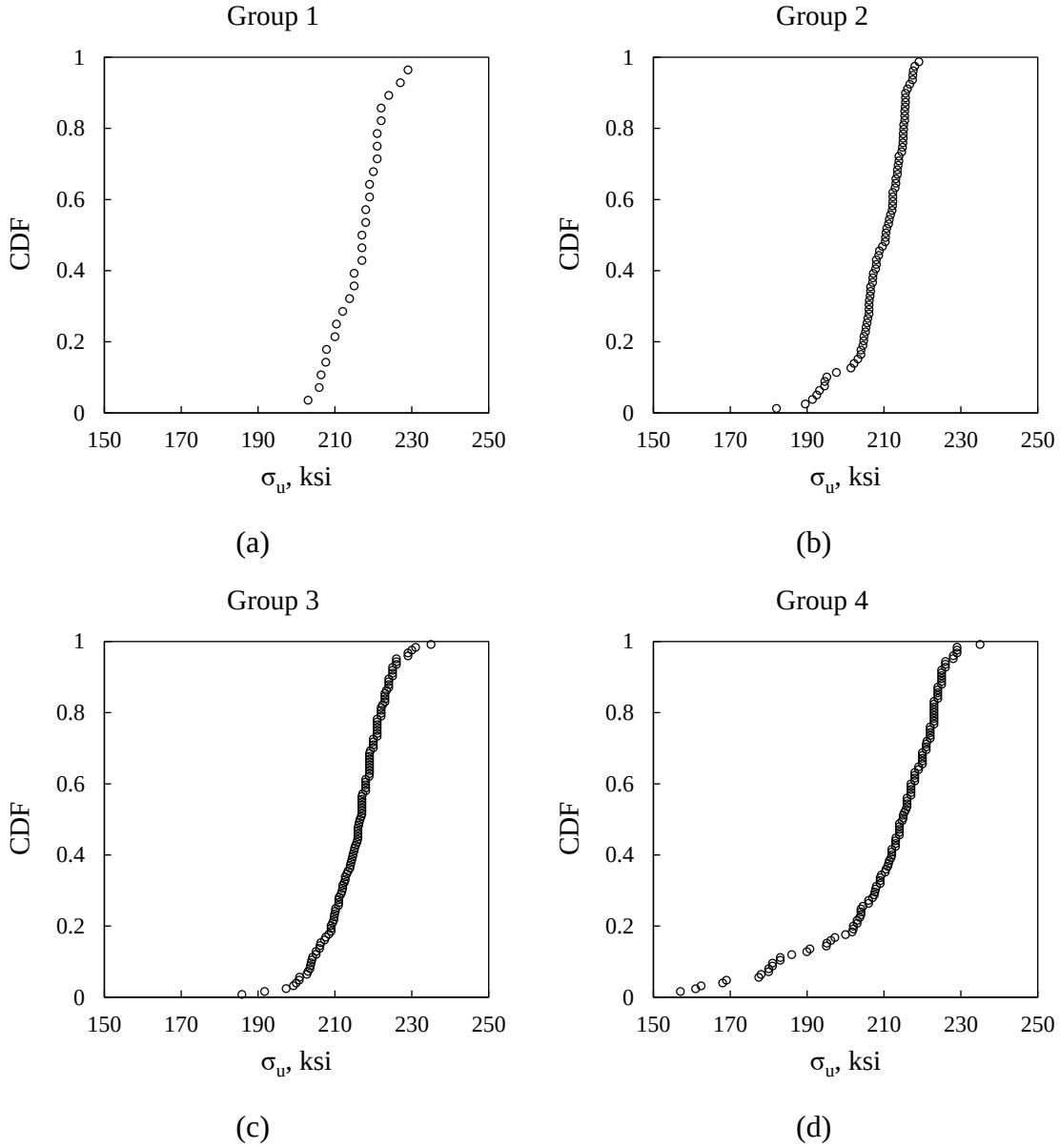

Figure 5.4: Empirical Cumulative Probability Distribution Functions for the ultimate strength of wire segments in different corrosion groups

5.2.3 Comparison with current standard approach in NCHRP Report 534

NCHRP Report 534 suggests three models for the estimation of the remaining cable strength: (1) Simplified Strength Model, (2) Brittle Wire Model, and (3) Limited Ductility Model. Table 5.2 displays the estimates for the overall cable strength of panel PP 2-3W of Bear Mountain Bridge

using the three models in NCHRP Report 534 and the proposed methodology (for the proposed methodology, mean, minimum and maximum values of the 10,000 simulations are provided). Table 5.2 indicates that the NCHRP Report 534 Brittle Wire and Limited Ductility Models provide unconservative values for the cable strength, as both are well above the maximum value of the 10,000 simulations. In contrast, the NCHRP Report 534 Simplified Method is overly conservative as its value for the cable strength is lower than the minimum value of the 10,000 simulations.

For further comparison with NCHRP Report 534 models, mainly Brittle Wire which is the most widely used method in practice, the overall cable strength R_u can be divided into two components, i.e., the strength of effective or non-broken wires (denoted by T_u in Section 4.4) and the redevelopment strength of broken wires (denoted by R_b in Section 4.4). To have a comprehensive understanding of the proposed method, each component is also compared with the result by NCHRP Report 534. Figure 5.5(a)-(c) display the evolution of the total strength T, strength of effective wires T_u and redevelopment strength R_b during the incremental loading process.

Table 5.2: Comparison of results for the overall cable strength of Bear Mountain Bridge: Monte Carlo simulation based proposed methodology (10,000 samples) versus the three standard models in NCHRP Report 534

Method Used		Overall Cable Strength (kips)
Proposed method	Mean value	24,750
	Minimum value	24,668
	Maximum value	24,836
NCHRP Report 534	Simplified strength model	15,900
	Brittle wire model	27,100
	Limited ductility model	27,200

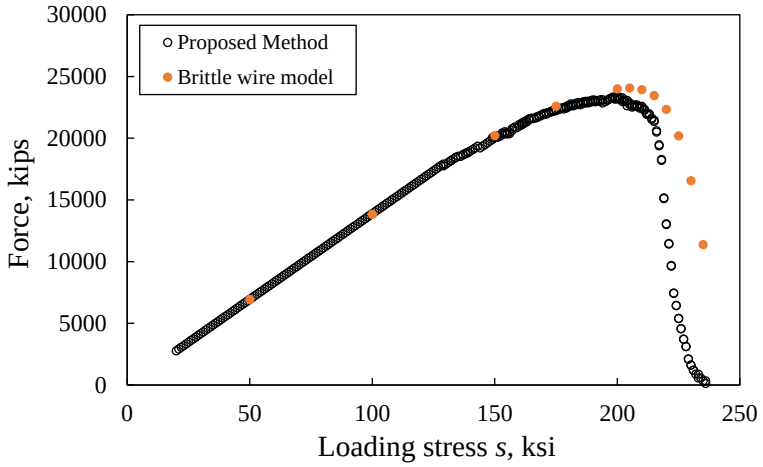

(a) Strength of effective wires T_u

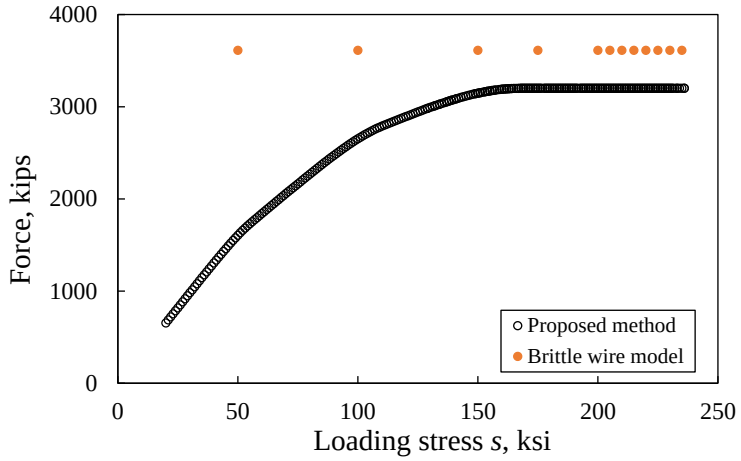

(b) Redevelopment strength of broken wires R_b

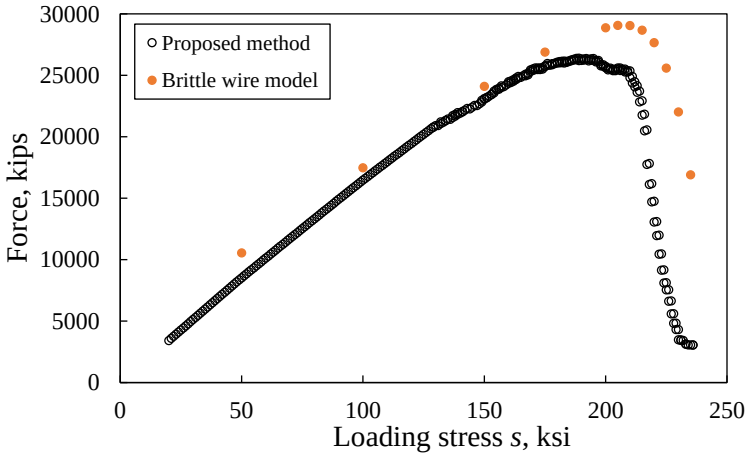

(c) Total force T

Figure 5.5: Comparison of each component force in the incremental loading process

To summarize, the main differences between the proposed methodology and the three models in NCHRP Report 534 are:

1) In the proposed methodology, all cracked wires are included in their corresponding corrosion stage groups (usually Groups 3 and 4) and fully accounted for (by including their usually reduced strengths in the corresponding CDF's). There is no need for any separate group for cracked wires. In contrast, NCHRP Report 534 separates cracked wires into an additional independent group. And the effects of cracked wires can be reflected by the effective strength T_u in Figure 5.5(a). It should be pointed out that, during a panel inspection, it is impossible to estimate the total number of cracked wires since they cannot be visually identified. The separation of cracked wires would overestimate the strength of effective wires.
2) The proposed methodology accounts for the variation of wire strength along the length of the panel through the variation of the corresponding corrosion conditions. This very important information is disregarded by NCHRP Report 534.
3) The proposed methodology accounts for the redeveloping strength of broken wires (R_b) in adjacent panels by reducing their originally simulated ultimate strength. The percent reduction (i.e. the redevelopment factor) depends on the location of the adjacent panels. In NCHRP 534, the redeveloped strength is simply taken as 95% of the mean strength of Group 2 wires, which is a constant value, as indicated in Figure 5.5(b).

The three models in NCHRP Report 534 provide three corresponding deterministic values for the cable strength. In contrast, the proposed methodology yields a full probability distribution function of the cable strength (as a histogram) through Monte Carlo simulations (see Figure 5.2).

5.3 Effect of corrosion & strength variation along wires on overall cable strength

It has been claimed in this work that it is very important to consider the variation of corrosion stage and strength along the length of wires within a panel. The validity of this claim is demonstrated in the following.

Let us consider two panel-long wires that, according to current NCHRP Report 534 practice, are both categorized as overall corrosion stage 4. Wire 1 is in relatively good condition (mostly in corrosion stage 2), with only one of its segments in corrosion stage 4:

Wire 1: 2 – 2 – 2 – 2 – 2 – 2 – 2 – 2 – 2 – 2 – 4 – 2 – 2 – 2 – 2 – 2 – 2 – 2 – 2 – 2

Wire 2, also in overall corrosion stage 4, is in poor condition and shows no variation of its corrosion stage along its length:

Wire 2: 4 – 4 – 4 – 4 – 4 – 4 – 4 – 4 – 4 – 4 – 4 – 4 – 4 – 4 – 4 – 4 – 4 – 4 – 4 – 4

Using the proposed procedure in Section 4.2 to calculate a wire's ultimate strength σ_u^{lw}, the histograms resulting from 10,000 realizations for the ultimate strength of Wires 1 and 2 are shown in Figure 5.6(a) and (b) respectively. The mean and standard deviation for Wire 1 are: 206.9 ksi and 16.9 ksi, while for Wire 2: 164.3 ksi and 28.5 ksi. By comparing the two histograms, it is clear that accounting for the spatial variation of the corrosion stage along a wire's length makes it possible to account for the considerable additional strength of Wire 1 compared to that of Wire 2 (although both wires are characterized as overall corrosion stage 4).

To demonstrate the impact of this corrosion stage variation on the overall cable strength, let us now use the case of Mid-Hudson Bridge, replacing the comprehensive corrosion stage wire profile in Table 3.1 with a new one, where no corrosion variation along the length of the wires exists, and every wire has all its segments assigned the worst corrosion stage along its length from Table 3.1 (this is called homogeneous corrosion conditions). Figure 5.7 plots the resulting histogram of 10,000

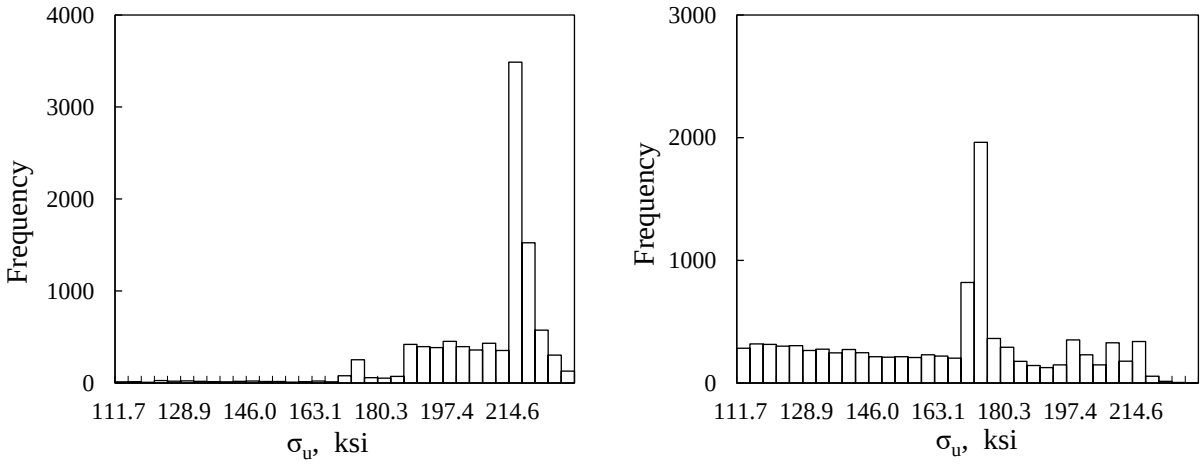

(a) Ultimate strength of Wire 1 (b) Ultimate strength of Wire 2

Figure 5.6: Empirical probability distribution functions for the ultimate strength of panel-long Wires 1 and 2.

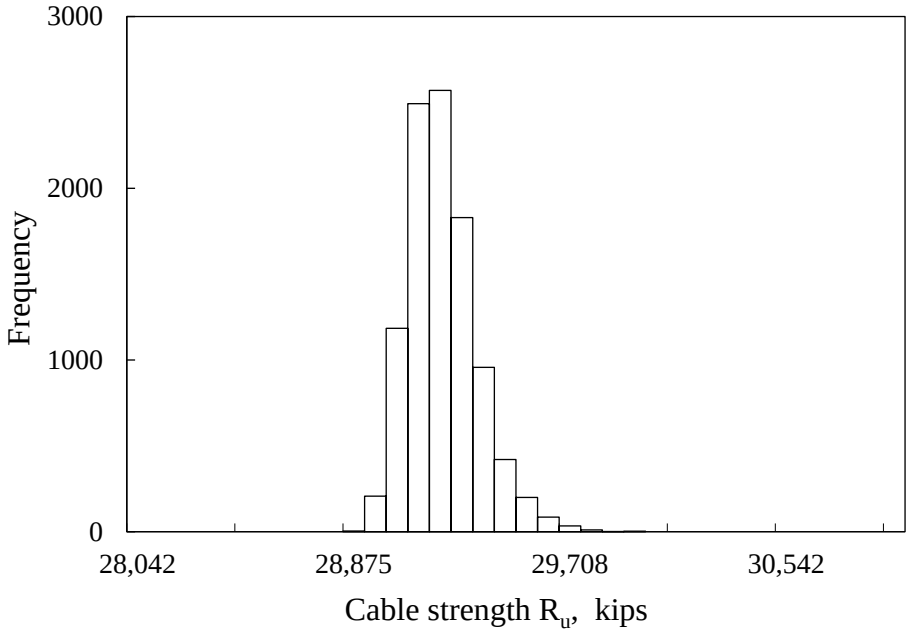

Figure 5.7: Histogram of 10,000 simulated values of the overall cable strength of the FDR Mid-Hudson Bridge using the proposed methodology, but disregarding spatial variation of corrosion stage along the length of one-panel-long wires (homogeneous corrosion conditions)

simulated values of R_u for this new case of homogeneous corrosion conditions, with mean value of 29,217 kips, standard deviation of 132 kips, minimum value of 28,885 kips and maximum value

of 29,997 kips. Comparing Figure 5.2 (spatial variation of corrosion conditions) and Figure 5.7 (homogeneous corrosion conditions), it becomes clear that the artificial and unrealistic assumption of homogeneous corrosion conditions leads to a significant (and erroneous) underestimate of the cable's real overall strength.

Summary

In the Part I of the dissertation, a novel methodology has been proposed to estimate the ultimate strength of the main cables of suspension bridges based on: (1) information collected during visual inspections of the wedged cable cross section, and (2) laboratory tensile tests of wires extracted from the cable's cross section. To fully account for the spatial variation of strength along a wire's length, the methodology uses the mapping of the corrosion stage variation of all wires exposed through wedging, along the length of the entire panel. Then, samples for the strength of wire segments can be generated based on the corrosion stages and probability distributions of each stage developed from laboratory testing.

The existence of broken wires in neighboring panels is fully accounted for, through a reduction in the evaluation panel of the original simulated strengths of wires that are broken in adjacent panels. After establishing the final map of the wires' ultimate strength accounting for both strength variation along the panel's length and redeveloped strength of broken wires in neighboring panels, an incremental loading procedure is applied to determine the overall cable strength for a given realization of the wire strength uncertainties. Using a Monte Carlo simulation approach allows the generation of a large number of realizations of the overall cable ultimate strength, so that its probability distribution function can be estimated through a histogram. The proposed methodology has been illustrated through an example involving the actual cable inspection of the Mid-Hudson

Bridge. Finally, It's also demonstrated that disregarding the corrosion stage variation of wires along the panel length, can lead to a significant underestimation of the overall strength of the cable. Finally, the flow chart of the methodology is shown in Figure 5.8.

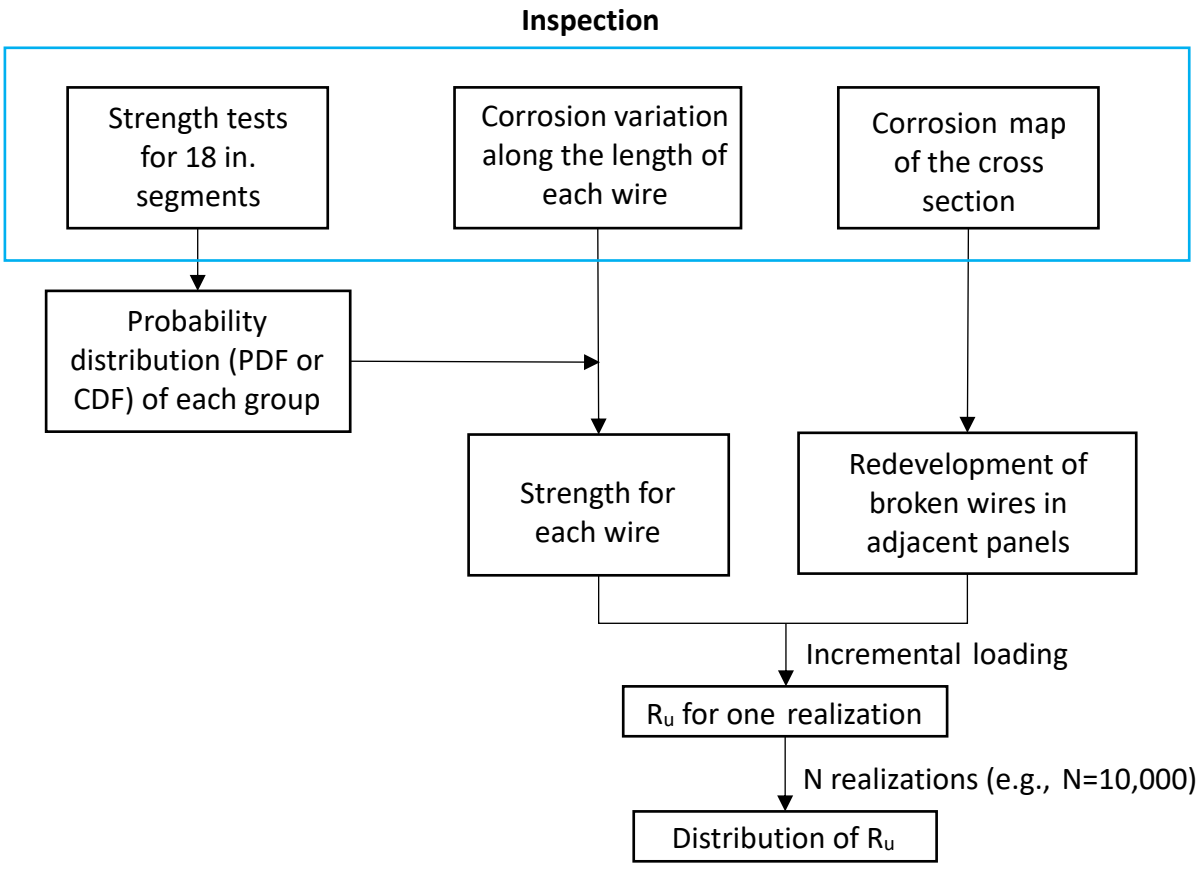

Figure 5.8: Flowchart of proposed methodology

Part II Development of Variability Response Function for Statically Indeterminate Structures

Chapter 6 Response Variability of Statically Indeterminate Structures

6.1 Introduction and scope

The research in Part II examines the uncertainty in the response of structures caused by stochastic material/system properties modeled by random fields. This response uncertainty is termed "response variability." Extensive work along these lines has been conducted over the last four decades resulting in a wide range of different methodologies to resolve such problems within the field of stochastic mechanics. The vast majority of this work has focused on determining the response variability of a structure for a specific random field modeling the uncertain material/system properties.

6.1.1 Random field model

In engineering world, many systems have attributes exhibit complex patterns of variation in space and time. Spatial variability of material properties is one of the most important physical attributes in civil engineering and engineering mechanics. There has been a history of research that material properties are interpreted as random fields, including analytical models for spatial variability of material strength [31, 32], discretization of material property variation and applying in finite element systems [33], and the modeling of random fields which is the bedrock of Monte Carlo simulations.

There have been some techniques developed to generate the realizations of random fields, Spectral Representative Method (SRM) [34, 35], Autoregressive Moving Average (ARMA) model [36]-[39], Karhunen-Loève decomposition [40, 41],to name a few. Among them, SRM is one of

the most widely used in civil engineering and engineering mechanics due to its simplicity and physical interpretation, i.e., it generates samples based on Spectral Density Function (SDF) of the stochastic process, which reflects the features on frequency domain. Over the years, the theory of SRM has also extended to model more complex stochastic fields to fit different scenarios in the real world. One of them is the modeling of non-Gaussian fields. It's very important for material properties which, by definition, should be non-negative and hence non-Gaussian. To achieve the goal, Grigoriu introduced a translation process [42]. It maps the underlying Gaussian process to the target non-Gaussian process making use of the CDFs and inverse CDFs of both types of processes. Some approximate techniques developed later to solve the case of 'incompatibility' in the translation theory [44]-[48].

6.1.2 Concept of Variability Response Function

As for dealing with the estimation of response variability, there are two sub-topics. One is Stochastic Finite Element Methodologies (SFEM), which involves numerical solution of the stochastic differential equations in the problem. It's a powerful approach and can be applied to various situations with flexibility, hence, majority of researches focus on this topic [49]-[51]. However, there are some cases where the response variability is needed for a wide range of different random fields describing these uncertain material/system properties (i.e. fields with different spectral characteristics, or equivalently, different correlation structures). For example, such problems can arise when the spectral characteristics of the random field are unknown (or partially known), and it becomes necessary to estimate the response variability for a range of different random fields. For such problems, calculating the response variability by SFEM requires a large (or very large) number of times – every time considering a different random field, which

is impractical because of the resulting prohibitive computational cost. In such case, the second option for response variability estimation, analytical solutions, are highly recommended. This work addresses this challenge by focusing on the concept of "Variability Response Function" that enables the performance of a full sensitivity analysis of the response variability with respect to the spectral characteristics of the random field modeling the uncertain material/system properties.

The concept of the Variability Response Function (VRF) was introduced in Shinozuka [52]. According to it, the variance of the response displacement of linear, elastic, and statically determinate beams is expressed in the following integral form:

$$Var[w] = \int_{-\infty}^{+\infty} S(\kappa)\mathrm{VRF}(\kappa)d\kappa \tag{6.1}$$

where w is the response displacement, $S(\kappa)$ is the spectral density function of the random field modeling the uncertain material/system properties, $\mathrm{VRF}(\kappa)$ is the Variability Response Function which is available in analytic form and is independent of the probabilistic characteristics of the random field describing the uncertain material/system properties, and κ is the wave number. It is immediately obvious that the above integral expression for the variance of the response displacement can be used to perform a full sensitivity analysis of the response variability with respect to the spectral characteristics of the random field modeling the uncertain material/system properties (considering also that the Variability Response Function is a smooth function of the wave number κ). For example, the upper bound for $Var[w]$ is obtained when the spectral density function $S(\kappa)$ becomes a Dirac delta function at the wave number where the Variability Response Function takes its maximum value. Furthermore, the response variability $Var[w]$ can be easily computed for any form of the spectral density function $S(\kappa)$.

For statically determinate structures like the ones considered by Shinozuka [52], the VRF can

be established analytically and its existence is consequently assured. The same has not been possible so far for statically indeterminate structures. There have been numerous attempts along these lines, starting with Bucher and Shinozuka [53] who suggested a first-order Taylor series expansion to compute the response statistics of a statically indeterminate beam (but without any reference to a VRF). Kardara et al. [54] extended the first-order Taylor series expansion idea to frame structures (again without any reference to a VRF). Deodatis and Shinozuka [55] used the basic idea of the first-order Taylor expansion in [53, 54] to formulate an integral expression identical to the one in Eq. (6.1) for the variance of the response displacement of a statically indeterminate beam. The limitation and accuracy of such approximation by Taylor expansion is analyzed by [56, 57]. At the same time, VRF has also been established in stochastic finite element system, which can accommodate more different structures with additional complexity. Deodatis [58, 59] expanded the first-order Taylor expansion-based VRF formulation to stochastic finite element systems. Deodatis [60, 61] proposed weighted integral method to formulate the exact expression of stiffness matrix and evaluate the response variability of statically indeterminate structures. Wall and Deodatis [62] to plane stress/strain problems, and Graham and Deodatis [63] to plate bending problems. Arwade et al. [64] built finite element based VRFs for apparent material properties. Papadopoulos et al. [65]-[67] went one step further by conjecturing the existence of the integral form in Eq. (6.1) for any linear, statically determinate or indeterminate, stochastic structural system.

Alternatively, VRF for statically indeterminate structures can be obtained by a Monte Carlo based methods called generalized VRF (GVRF). Deodatis et al. [56-57, 65] introduced a generalized VRF (GVRF) where a family of stochastic fields is included (associated fields). Fast Monte Carlo simulations are then applied to obtain the GVRF. It’s a more general method to

evaluate the response variabilities of statically indeterminate structures and it's then used in various situations[69]-[74]. Although extensive works on developments and applications of Variability Response Function have been carried out over the years, the developments of VRF for statically indeterminate structures still remain challenging with some key questions not perfectly answered, e.g., does the standard form in Eq. (6.1) exist, or is it possible to derive an analytical close-form VRF?

This work revisits the problem of a VRF-based integral expression for the response variance of statically indeterminate structures, and demonstrates that a form like the one shown in Eq. (6.1) does not necessarily exist for statically indeterminate structures. VRFs for the response bending moment and deflection of the structures are developed for statically indeterminate beams, by making use of the zero-moment location along the length of the beam. Numerical examples are then followed and the accuracy of the results obtained using the proposed formulations is validated using Monte Carlo simulations.

6.2 Statically indeterminate structure with random material properties

6.2.1 Random variability of material properties

Consider the statically indeterminate beam shown in Figure 6.1(a) having length L, a constant cross-sectional area A, and a deterministic uniformly distributed load q_0. The beam is fixed at x=0 and pinned at x=L. It is assumed that Young's modulus $E(x)$ varies randomly along the length of the beam and can be modeled as a stochastic field. The inverse of $E(x)$ is assumed to constitute a homogenous, one-dimensional, scalar stochastic field [52-54, 65-67]:

$$\frac{1}{E(x)} = \frac{1}{E_0}[1 + f(x)] \tag{6.2}$$

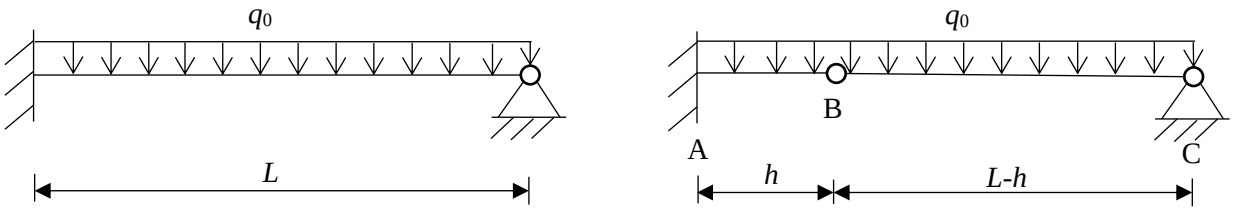

(a) Statically indeterminate beam (b) Statically determinate beam

Figure 6.1: Configuration of statically indeterminate beam and its equivalent statically determinate one. The hinge in the statically determinate structure (b) is introduced at the location of zero bending moment of the statically indeterminate structure (a)

where $1/E_0$ is the expected value of $1/E(x)$ i.e. $\varepsilon[1/E(x)] = 1/E_0$ with $\varepsilon[\cdot]$ denoting the expectation, and $f(x)$ is a zero-mean, homogeneous stochastic field.

Let $R_{ff}(\xi)$ denote the autocorrelation function of $f(x)$:

$$R_{ff}(\xi) = \varepsilon[f(x+\xi) f(x)] \tag{6.3}$$

where ξ is the separation distance. Also let $S_{ff}(\kappa)$ denote the spectral density function of $f(x)$ with κ being the wave number. $R_{ff}(\xi)$ and $S_{ff}(\kappa)$ are related through the Wiener-Khintchine transform [75]-[77]:

$$R_{ff}(\xi) = \int_{-\infty}^{+\infty} S_{ff}(\kappa) e^{i\kappa\xi} d\kappa \tag{6.4}$$

6.2.2 Response functions and random zero-moment location

It is well-known that the statically indeterminate structure in Figure 6.1(a) will have a bending moment diagram with a location where the moment will be equal to zero (this applies to structures with both constant and varying material properties along their length). The location of zero bending moment is equivalent to the presence of a hinge at that point, making the original statically

indeterminate structure in Figure 6.1(a) equivalent to the statically determinate one in Figure 6.1(b). The distance of the hinge from the left end of the beam is denoted by *h* as can be seen in Figure 6.1(b). The response functions (bending moments and deflections) of the structure can be obtained by solving the governing differential equation of the statically indeterminate Euler-Bernoulli beam in Figure 6.1(a):

$$\frac{d^2}{dx^2}\left(E(x)I\frac{d^2w}{dx^2}\right)=q(x) \tag{6.5}$$

where I is the constant cross-sectional moment of inertia, $w(x)$ is the deflection, and $q(x)$ is the load assumed to be constant and equal to q_0. The boundary conditions are:

$$\begin{cases} w(x=0)=0 \\ w(x=L)=0 \\ \dfrac{dw}{dx}(x=0)=0 \\ M(x=L)=0 \end{cases} \tag{6.6}$$

where $M(x)$ denotes the bending moment. It is also known that: $M(x=h)=0$.

The bending moment $M(x)$ can be determined by integrating Eq. (6.5) twice:

$$\left(E(x)I\frac{d^2w}{dx^2}\right)=-M(x)=\int_0^x\int_0^{x_1}q_0dx_2dx_1+c_1x+c_2 \tag{6.7}$$

where c_1 and c_2 are parameters to be determined. Using boundary condition: $M(x=L)=0$ with Eq. (6.7) yields:

$$M(x=L)=-\int_0^L\int_0^{x_1}q_0dx_2dx_1-c_1L-c_2=0 \tag{6.8}$$

and solving with respect to c_2:

$$c_2=-\int_0^L\int_0^{x_1}q_0dx_2dx_1-c_1L=\frac{q_0L^2}{2}-c_1L \tag{6.9}$$

Using now the condition that the bending moment is zero at $x=h$, i.e., $M(x=h)=0$, with Eq. (6.7) yields:

$$M(x=h)=-\int_0^h\int_0^{x_1} q_0 dx_2 dx_1 - c_1 h - c_2 = 0 \tag{6.10}$$

Substituting the expression for c_2 in Eq. (6.9) into Eq. (6.10) results in:

$$c_1 = \frac{q_0}{2}(h+L) \tag{6.11}$$

Substituting Eqs. (6.9) and (6.11) into Eq. (6.7), the following expression is established for the bending moment:

$$M(x) = -\frac{q_0}{2}(x-h)(x-L) \tag{6.12}$$

After two more integrations and application of the boundary conditions $w(x=0)=0$ and $\frac{dw}{dx}(x=0)=0$, the deflection function $w(x)$ is obtained as:

$$w(x) = -\int_0^x\int_0^{x_1} \frac{M(x_2)}{E(x_2)I} dx_2 dx_1 = \frac{q_0}{2}\int_0^x\int_0^{x_1} \frac{(x_2-h)(x_2-L)}{E(x_2)I} dx_2 dx_1 \tag{6.13}$$

The location of zero-moment h in response functions $M(x)$ and $w(x)$ is not constant. It constitutes a random variable as will be shown in the following subsection.

6.2.3 Determination of analytical expression for zero-moment location h

When Young's modulus is deterministic and constant over the entire length of the beam, i.e., $E(x)=E_0$ for $x \in [0, L]$, conventional structural analysis establishes the location of the hinge as: $h = h_m = L/4$. However, when $1/E(x)$ is modeled as a stochastic field according to Eq. (6.2), the values of $1/E(x)$ will change from location to location along the length of the beam and, in principle, it is possible to have an infinity of different realizations of $1/E(x)$ over the length of the

structure. Each one of these realizations of $1/E(x)$ will yield a different location for the zero-moment and subsequently for the location of the hinge h. This means that h becomes a random variable. An expression for h will be derived in this subsection in terms of stochastic field $f(x)$.

Based on the governing equations and derived deflection function $w(x)$, there is one last boundary condition remaining: $w(x=L)=0$. Applying it on Eq. (6.13) yields:

$$w(x=L)=\frac{q_0}{2}\int_0^L\int_0^{x_1}\frac{(x_2-h)(x_2-L)}{E(x_2)I}dx_2dx_1=0 \tag{6.14}$$

Equation (6.14) is rewritten as:

$$\begin{aligned}\int_0^L\int_0^{x_1}\frac{(x_2-h)(x_2-L)}{E(x_2)I}dx_2dx_1&=\int_0^L dx_2\int_{x_2}^L\frac{(x_2-h)(x_2-L)}{E(x_2)I}dx_1\\&=\int_0^L\frac{(L-x_2)(x_2-h)(x_2-L)}{E(x_2)I}dx_2\\&=\int_0^L\left[\frac{h(x_2-L)^2}{E(x_2)I}-\frac{x_2(x_2-L)^2}{E(x_2)I}\right]dx_2=0\end{aligned} \tag{6.15}$$

In the integral appearing in Eq. (6.15), $E(x_2)$ is obviously a function of the x_2 coordinate and cannot be taken out of the integral. However, although the zero-moment location h depends on the specific realization of $E(x_2)$, once a specific realization of $E(x_2)$ is established, h becomes a constant value independent of the x_2 coordinate, and consequently can be taken out of the integral:

$$h\int_0^L\frac{(x_2-L)^2}{E(x_2)I}dx_2-\int_0^L\frac{x_2(x_2-L)^2}{E(x_2)I}dx_2=0 \tag{6.16}$$

Finally, substituting the expression for $E(x_2)$ in Eq. (6.2) into Eq. (6.16), the analytic expression for the value of the zero-moment location h is determined as:

$$h=\frac{\int_0^L x_2(x_2-L)^2(1+f(x_2))dx_2}{\int_0^L(x_2-L)^2(1+f(x_2))dx_2} \tag{6.17}$$

Equation (6.17) clearly indicates that the zero-moment location h is a random variable depending on the specific realization of stochastic field $f(x)$. For each realization of stochastic field $f(x)$, a corresponding realization of h can be obtained using Eq. (6.17).

It should be noted that the location of zero-moment can also be determined numerically using the Finite Element Method (FEM). This is demonstrated in Figure 6.2 where 1,000 values of h are determined analytically using Eq. (6.17) and numerically using FEM. For this purpose, 1,000 sample realizations of stochastic field $f(x)$ are generated according to the following spectral density function:

$$S_{ff}(\kappa) = \frac{1}{4}\sigma_{ff}^2 b^3 \kappa^2 e^{-b|\kappa|} \tag{6.18}$$

where $f(x)$ is modeled as a truncated Gaussian field with $\sigma_{ff} = 0.1$ and b = 1 m.

The beam parameters associated with the results in Figure 6.2 are: L = 5 m, $E_0I = 2.8125 \cdot 10^6$ N·m^2 and q_0 = 1,000 N/m. In Figure 6.2, red x's are indicating values of h obtained using Eq. (6.17) and blue circles indicate values of h obtained using FEM. When the same realization of stochastic field $f(x)$ is used, the values of h calculated from the two approaches coincide as expected and as can be seen in Figure 6.2 (i.e., there is an x inside each circle, and these two identical values of h are obtained using the same realization of stochastic field $f(x)$). For the case shown in Figure 6.2, the deterministic value of h is equal to 1.25m, $h_m = {}^{L}/_{4} = 1.25\text{m}$ (obtained when the elastic modulus is constant along the length of the beam and equal to its mean value E_0).

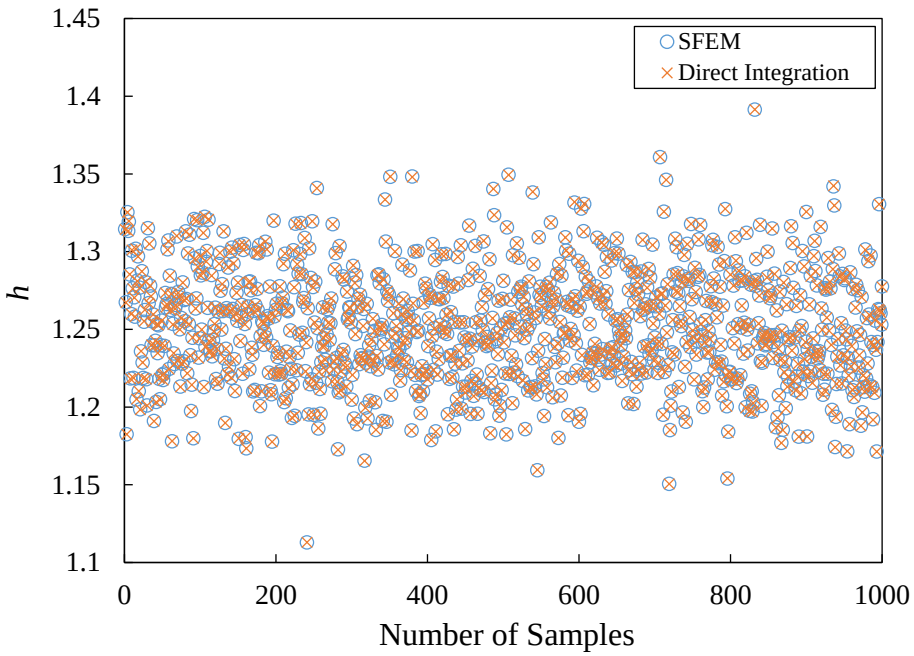

Figure 6.2: Comparison of h values generated by FEM and by direct integration of Eq. (6.17)

Chapter 7 Variability Response Function for Bending Moments

In this chapter, the response bending moment along the length of the beam, $M(x)$, is expressed as a function of its (random) zero-moment location. This approach, combined with a second-order Taylor series expansion of the random zero-moment location, leads to novel Variability Response Function-based integral expressions for the variance of the response bending moment, $Var[M(x)]$. Extensive numerical examples are then provided where the accuracy of the results obtained using the proposed formulation is validated using Monte Carlo simulations involving stochastic fields that follow truncated Gaussian and shifted lognormal probability distribution functions.

7.1 Mean and variance of bending moment $M(x)$

The only random quantity in the expression for the bending moment $M(x)$ in Eq. (6.12) is h. In other words, the uncertainty of $M(x)$ is fully controlled by random variable h.

The expected value of $M(x)$ is computed as:

$$\begin{aligned}\varepsilon[M(x)] &= -\frac{q_0}{2}\varepsilon[(x-h)(x-L)] \\ &= -\frac{q_0}{2}(x-L)\varepsilon[x-h] = -\frac{q_0}{2}(x-L)(x-\varepsilon[h])\end{aligned} \tag{7.1}$$

while the variance of $M(x)$ is given by:

$$
\begin{aligned}
Var[M(x)] &= \varepsilon[(M(x)-\varepsilon[M(x)])^2] \\
&= \varepsilon\left[\left(-\frac{q_0}{2}(x-h)(x-L)+\frac{q_0}{2}(x-\varepsilon[h])(x-L)\right)^2\right] \\
&= \varepsilon\left[\left(\frac{q_0}{2}(x-L)(-x+h+x-\varepsilon[h])\right)^2\right] \\
&= \left(\frac{q_0}{2}(x-L)\right)^2 \varepsilon[(h-\varepsilon[h])^2] \\
&= \left(\frac{q_0}{2}(x-L)\right)^2 Var[h] = \left(\frac{q_0}{2}(x-L)\right)^2 \{\varepsilon[h^2]-(\varepsilon[h])^2\}
\end{aligned}
\tag{7.2}
$$

where Var designates the variance. Equations (7.1) and (7.2) indicate that as $M(x)$ is a linear function of h (see Eq.(6.12)), its mean value and variance are expressed as linear functions of the mean and variance of h. In different words, finding the mean and variance of $M(x)$ is equivalent to finding the mean and variance of h, which is accomplished in the following section.

7.2 Estimation of mean, mean square and variance of *h*

The expression for h in Eq. (6.17) indicates that h is not a simple linear function of stochastic field $f(x)$, as $f(x)$ appears in the integrands of both the numerator and denominator. Obviously, h is a nonlinear function of $f(x)$ and it's not possible to determine a closed-form expression for the stochastic variability of such function. Consequently, a Taylor series expansion will be used. For this purpose, Eq. (6.17) is rewritten as:

$$
h = \frac{\int_0^L x_2(x_2-L)^2(1+f(x_2))dx_2}{\int_0^L (x_2-L)^2(1+f(x_2))dx_2} = \frac{X}{Y} \tag{7.3}
$$

with:

$$X = \int_0^L x_2 (x_2 - L)^2 (1 + f(x_2)) dx_2 \tag{7.4}$$

$$Y = \int_0^L (x_2 - L)^2 (1 + f(x_2)) dx_2 \tag{7.5}$$

The expression for X/Y can be expanded using a Taylor series at point ($X=\beta$, $Y=\alpha$) as follows:

$$h = \frac{X}{Y} = \frac{\beta}{\alpha} + \left.\frac{\partial h}{\partial X}\right|_{\alpha,\beta} (X - \beta) + \left.\frac{\partial h}{\partial Y}\right|_{\alpha,\beta} (Y - \alpha) + \cdots \tag{7.6}$$

The point ($X=\beta$, $Y=\alpha$) is selected as the means of X and Y:

$$\alpha = \varepsilon[Y] = \int_0^L (x_2 - L)^2 \varepsilon[1 + f(x_2)] dx_2 = \int_0^L (x_2 - L)^2 dx_2 \tag{7.7}$$

$$\beta = \varepsilon[X] = \int_0^L x (x - L)^2 dx \tag{7.8}$$

In this dissertation, first- and second-order Taylor series expansions will be considered to establish the mean and variance of h, and eventually, the variance of $M(x)$ and the corresponding Variability Response Functions.

7.2.1 First-order Taylor series

Consider the first-order Taylor series expansion of X/Y in Eq. (7.6):

$$\frac{X}{Y} = \frac{\beta}{\alpha} + \left.\frac{\partial h}{\partial X}\right|_{\alpha,\beta} \cdot (X - \beta) + \left.\frac{\partial h}{\partial Y}\right|_{\alpha,\beta} \cdot (Y - \alpha) + \theta_1 \approx \frac{\beta}{\alpha} + \left.\frac{\partial h}{\partial X}\right|_{\alpha,\beta} \cdot (X - \beta) + \left.\frac{\partial h}{\partial Y}\right|_{\alpha,\beta} \cdot (Y - \alpha) \tag{7.9}$$

where θ_1 is the expansion's error. Then, h can be expressed as:

$$h = \frac{X}{Y} \approx \frac{\beta}{\alpha} + (X - \beta)\frac{1}{\alpha} - (Y - \alpha)\frac{\beta}{\alpha^2} = \frac{X}{\alpha} - \frac{Y\beta}{\alpha^2} + \frac{\beta}{\alpha} \tag{7.10}$$

The expected value of h, $\varepsilon[h]$, can be written as:

$$\varepsilon[h] = \frac{1}{\alpha}\varepsilon[X] - \frac{\beta}{\alpha^2}\varepsilon[Y] + \frac{\beta}{\alpha} \tag{7.11}$$

Considering that Eqs. (7.7) and (7.8) yield: $\alpha = \frac{L^3}{3}$, $\beta = \frac{L^4}{12}$, so that: $\frac{\beta}{\alpha} = h_m = \frac{L}{4}$, the expected value of *h* in Eq. (7.11) can be determined as:

$$\varepsilon[h] = \frac{\beta}{\alpha} \tag{7.12}$$

Equation (7.12) indicates that, when using a first-order Taylor approximation, the expected value of *h* is constant and independent of stochastic field *f*(*x*). Note that the term $\frac{\beta}{\alpha}$ represents the deterministic value of *h* obtained when the elastic modulus is constant along the length of the beam and equal to its mean value E_0.

Using Eq. (7.10), the mean square of *h*, $\varepsilon[h^2]$, is written as:

$$\begin{aligned}
\varepsilon[h^2] &= \varepsilon\left[\left(\frac{X}{\alpha} - \frac{Y\beta}{\alpha^2} + \frac{\beta}{\alpha}\right)^2\right] \\
&= \varepsilon\left[\frac{\beta^2}{\alpha^2} + \frac{2\beta X}{\alpha^2} + \frac{X^2}{\alpha^2} - \frac{2\beta^2 Y}{\alpha^3} - \frac{2\beta XY}{\alpha^3} + \frac{\beta^2 Y^2}{\alpha^4}\right] \\
&= \frac{\beta^2}{\alpha^2} + \frac{1}{\alpha^2}\varepsilon[X^2] - \frac{2\beta}{\alpha^3}\varepsilon[XY] + \frac{\beta^2}{\alpha^4}\varepsilon[Y^2]
\end{aligned} \tag{7.13}$$

Three terms have to be computed in Eq.(7.13): $\varepsilon[X^2]$, $\varepsilon[XY]$ and $\varepsilon[Y^2]$. The term $\varepsilon[XY]$ is written as:

$$
\begin{aligned}
\varepsilon[XY] &= \varepsilon\left[\int_0^L x_1(x_1-L)^2(1+f(x_1))dx_1 \cdot \int_0^L (x_2-L)^2(1+f(x_2))dx_2\right] \\
&= \varepsilon\left[\int_0^L\int_0^L x_1(x_1-L)^2(x_2-L)^2(1+f(x_1))(1+f(x_2))dx_1dx_2\right] \\
&= \int_0^L\int_0^L x_1(x_1-L)^2(x_2-L)^2\varepsilon[(1+f_1f_2+f_1+f_2]dx_1dx_2 \\
&= \int_0^L\int_0^L x_1(x_1-L)^2(x_2-L)^2(1+\varepsilon[f_1f_2])dx_1dx_2 \\
&= \int_0^L\int_0^L x_1(x_1-L)^2(x_2-L)^2dx_1dx_2 + \int_0^L\int_0^L x_1(x_1-L)^2(x_2-L)^2R(x_1-x_2)dx_1dx_2
\end{aligned}
\tag{7.14}
$$

where f_1 and f_2 stand for $f(x_1)$ and $f(x_2)$, $\varepsilon[f_1]=\varepsilon[f_2]=0$, and $\varepsilon[f_1f_2]=R(x_1-x_2)$ according to the definition of the autocorrelation function in Eq. (6.3).

Using the Wiener-Khintchine transform on the autocorrelation function in Eq. (7.14) leads to:

$$
\begin{aligned}
\varepsilon[XY] &= \int_0^L\int_0^L x_1(x_1-L)^2(x_2-L)^2dx_1dx_2 + \int_0^L\int_0^L x_1(x_1-L)^2(x_2-L)^2\int_{-\infty}^{+\infty} S_{ff}(\kappa)e^{i(x_1-x_2)\kappa}d\kappa dx_1dx_2 \\
&= C_1 + \int_{-\infty}^{+\infty} S_{ff}(\kappa)V_1(\kappa)d\kappa
\end{aligned}
\tag{7.15}
$$

where:

$$
C_1 = \int_0^L\int_0^L x_1(x_1-L)^2(x_2-L)^2dx_1dx_2 = \alpha\beta \tag{7.16}
$$

$$
V_1(\kappa) = \int_0^L x_1(x_1-L)^2e^{ix_1\kappa}dx_1 \cdot \int_0^L (x_2-L)^2e^{-ix_2\kappa}dx_2 \tag{7.17}
$$

Note that the imaginary part of V_1 in Eq. (7.17) is an odd function of κ, and consequently, $\varepsilon[XY]$ in Eq. (7.15) will be real-valued (as the spectral density function is an even function of κ).

The term $\varepsilon[X^2]$ is written as:

$$\begin{aligned}\varepsilon[X^2] &= \varepsilon\left[\int_0^L x_1(x_1-L)^2(1+f(x_1))dx_1 \cdot \int_0^L x_2(x_2-L)^2(1+f(x_2))dx_2\right] \\ &= \int_0^L\int_0^L x_1x_2(x_1-L)^2(x_2-L)^2\varepsilon[1+f_1f_2+f_1+f_2]dx_1dx_2 \\ &= \int_0^L\int_0^L x_1x_2(x_1-L)^2(x_2-L)^2\left(1+\varepsilon[f_1f_2]\right)dx_1dx_2 \\ &= \int_0^L\int_0^L x_1x_2(x_1-L)^2(x_2-L)^2dx_1dx_2 + \int_0^L\int_0^L x_1x_2(x_1-L)^2(x_2-L)^2R(x_1-x_2)dx_1dx_2\end{aligned} \tag{7.18}$$

Using the Wiener-Khintchine transform on the autocorrelation function in Eq. (7.18) leads to:

$$\begin{aligned}\varepsilon[X^2] &= C_2 + \int_0^L\int_0^L x_1x_2(x_1-L)^2(x_2-L)^2\left(\int_{-\infty}^{+\infty} S_{ff}(\kappa)e^{i(x_1-x_2)\kappa}d\kappa\right)dx_1dx_2 \\ &= C_2 + \int_{-\infty}^{+\infty} S_{ff}(\kappa)\,|V_2(\kappa)|^2\,d\kappa\end{aligned} \tag{7.19}$$

where:

$$C_2 = \int_0^L\int_0^L x_1x_2(x_1-L)^2(x_2-L)^2dx_1dx_2 = \beta^2 \tag{7.20}$$

$$V_2(\kappa) = \int_0^L x_1(x_1-L)^2e^{ix_1\kappa}dx_1 \tag{7.21}$$

For the last term, $\varepsilon[Y^2]$:

$$\begin{aligned}\varepsilon[Y^2] &= \varepsilon\left[\int_0^L (x_1-L)^2(1+f(x_1))dx_1 \cdot \int_0^L (x_2-L)^2(1+f(x_2))dx_2\right] \\ &= \int_0^L\int_0^L (x_1-L)^2(x_2-L)^2\varepsilon[1+f_1f_2+f_1+f_2]dx_1dx_2 \\ &= \int_0^L\int_0^L (x_1-L)^2(x_2-L)^2\left(1+\varepsilon[f_1f_2]\right)dx_1dx_2 \\ &= \int_0^L\int_0^L (x_1-L)^2(x_2-L)^2dx_1dx_2 + \int_0^L\int_0^L (x_1-L)^2(x_2-L)^2R(x_1-x_2)dx_1dx_2\end{aligned} \tag{7.22}$$

Using the Wiener-Khintchine transform again:

$$\begin{aligned}\varepsilon[Y^2] &= C_3 + \int_0^L \int_0^L (x_1 - L)^2 (x_2 - L)^2 \left(\int_{-\infty}^{+\infty} S_{ff}(\kappa) e^{i(x_1 - x_2)\kappa} d\kappa \right) dx_1 dx_2 \\ &= C_3 + \int_{-\infty}^{+\infty} S_{ff}(\kappa) |V_3(\kappa)|^2 \, d\kappa \end{aligned} \tag{7.23}$$

where:

$$C_3 = \int_0^L \int_0^L (x_1 - L)^2 (x_2 - L)^2 dx_1 dx_2 = \alpha^2 \tag{7.24}$$

$$V_3(\kappa) = \int_0^L (x_1 - L)^2 e^{ix_1\kappa} dx_1 \tag{7.25}$$

Finally, substituting Eqs.(7.15), (7.19) and (7.23) into Eq. (7.13), yields the following expression for $\varepsilon[h^2]$:

$$\varepsilon[h^2] = \frac{\beta^2}{\alpha^2} + \int_{-\infty}^{+\infty} S_{ff}(\kappa) \frac{1}{\alpha^2} \left[|V_2(\kappa)|^2 - \frac{2\beta}{\alpha} V_1(\kappa) + \frac{\beta^2}{\alpha^2} |V_3(\kappa)|^2 \right] d\kappa \tag{7.26}$$

Denoting now:

$$\mathrm{VRF}_1(\kappa) = \frac{1}{\alpha^2} \left(|V_2(\kappa)|^2 - \frac{2\beta}{\alpha} V_1(\kappa) + \frac{\beta^2}{\alpha^2} |V_3(\kappa)|^2 \right) \tag{7.27}$$

results in the following VRF-based integral expression for the mean square of *h*:

$$\varepsilon[h^2] = h_m^2 + \int_{-\infty}^{+\infty} S_{ff}(\kappa) \mathrm{VRF}_1(\kappa) d\kappa \tag{7.28}$$

Note that the imaginary part of V_1 in Eq. (7.27) is an odd function of κ, and consequently, $\varepsilon[h^2]$ will be real-valued (as the spectral density function is an even function of κ).

7.2.2 Second-order Taylor series

Consider now the second-order Taylor series expansion of *X*/*Y* in Eq. (7.6):

$$\frac{X}{Y} \approx \frac{\beta}{\alpha} + \left.\frac{\partial h}{\partial X}\right|_{\alpha,\beta}(X-\beta) + \left.\frac{\partial h}{\partial Y}\right|_{\alpha,\beta}(Y-\alpha) + \left.\frac{\partial^2 h}{\partial X \partial Y}\right|_{\alpha,\beta}(X-\beta)(Y-\alpha) + \frac{1}{2}\left.\frac{\partial^2 h}{\partial X^2}\right|_{\alpha,\beta}(X-\beta)^2 + \frac{1}{2}\left.\frac{\partial^2 h}{\partial Y^2}\right|_{\alpha,\beta}(Y-\alpha)^2 \tag{7.29}$$

Then, h can be expressed as:

$$h = \frac{X}{Y} \approx \frac{\beta}{\alpha} + \frac{1}{\alpha}(X-\beta) - \frac{\beta}{\alpha^2}(Y-\alpha) - \frac{1}{\alpha^2}(X-\beta)(Y-\alpha) + \frac{\beta}{\alpha^3}(Y-\alpha)^2 = \frac{\beta}{\alpha} + \frac{2X}{\alpha} - \frac{2\beta Y}{\alpha^2} - \frac{XY}{\alpha^2} + \frac{bY^2}{\alpha^3} \tag{7.30}$$

The expected value of h, $\varepsilon[h]$, can be written as:

$$\varepsilon[h] = \varepsilon\left[\frac{\beta}{\alpha} + \frac{2X}{\alpha} - \frac{2\beta Y}{\alpha^2} - \frac{XY}{\alpha^2} + \frac{bY^2}{\alpha^3}\right] = \frac{\beta}{\alpha} - \frac{1}{\alpha^2}\varepsilon[XY] + \frac{\beta}{\alpha^3}\varepsilon[Y^2] \tag{7.31}$$

where $\varepsilon[XY]$ is given in Eq. (7.15) and $\varepsilon[Y^2]$ in Eq. (7.23). After some algebra, the following VRF-based integral expression is established for $\varepsilon[h]$:

$$\varepsilon[h] = \frac{\beta}{\alpha} + \frac{1}{\alpha^3}\int_{-\infty}^{+\infty} S_{ff}(\kappa)[-\alpha V_1(\kappa) + \beta |V_3(\kappa)|^2]d\kappa = h_m + \int_{-\infty}^{+\infty} S_{ff}(\kappa)\frac{[-\alpha V_1(\kappa) + \beta |V_3(\kappa)|^2]}{\alpha^3}\,d\kappa = h_m + \int_{-\infty}^{+\infty} S_{ff}(\kappa)\mathrm{VRF}_{mean}(\kappa)\,d\kappa \tag{7.32}$$

The mean value of h in Eq. (7.32) is again real-valued following a similar reasoning as earlier, but is not constant as was the case involving the first-order Taylor series expansion (Eq. (7.12)). Instead, it is now a function of stochastic field $f(x)$ as can be seen in Eq (7.32).

Using Eq. (7.30), the mean square of h is expressed as:

$$\varepsilon[h^2] = \varepsilon\left[\left(\frac{\beta}{\alpha}+\frac{2X}{\alpha}-\frac{2\beta Y}{\alpha^2}-\frac{XY}{\alpha^2}+\frac{bY^2}{\alpha^3}\right)^2\right]$$

$$= \varepsilon\left[\begin{array}{l}\frac{\beta^2}{\alpha^2}+\frac{4\beta X}{\alpha^2}+\frac{4X^2}{\alpha^2}-\frac{4\beta^2 Y}{\alpha^3}-\frac{10\beta XY}{\alpha^3}-\frac{4X^2Y}{\alpha^3}+\frac{6\beta^2Y^2}{\alpha^4} \\ +\frac{8\beta XY^2}{\alpha^4}+\frac{X^2Y^2}{\alpha^4}-\frac{4\beta^2Y^3}{\alpha^5}-\frac{2\beta XY^3}{\alpha^5}+\frac{\beta^2Y^4}{\alpha^6}\end{array}\right] \tag{7.33}$$

$$= \frac{\beta^2}{\alpha^2}+\frac{4}{\alpha^2}\varepsilon[X^2]-\frac{10\beta}{\alpha^3}\varepsilon[XY]+\frac{6\beta^2}{\alpha^4}\varepsilon[Y^2]-\frac{4}{\alpha^3}\varepsilon[X^2Y]+$$

$$\frac{8\beta}{\alpha^4}\varepsilon[XY^2]+\frac{1}{\alpha^4}\varepsilon[X^2Y^2]-\frac{4\beta^2}{\alpha^5}\varepsilon[Y^3]-\frac{2\beta}{\alpha^5}\varepsilon[XY^3]+\frac{\beta^2}{\alpha^6}\varepsilon[Y^4]$$

There are nine terms that need to be determined in Eq. (7.33). The first three ($\varepsilon[X^2]$, $\varepsilon[XY]$ and $\varepsilon[Y^2]$) have been already established in Eqs. (7.19), (7.15) and (7.23). For the fourth term, $\varepsilon[X^2Y]$:

$$\varepsilon[X^2Y] = \varepsilon\left[\begin{array}{l}\int_0^L x_1(x_1-L)^2(1+f(x_1))dx_1 \cdot \int_0^L x_2(x_2-L)^2(1+f(x_2))dx_2 \\ \cdot\int_0^L (x_3-L)^2(1+f(x_3))dx_3\end{array}\right]$$

$$= \varepsilon\left[\int_0^L\int_0^L\int_0^L G(x_1,x_2,x_3)(1+f_1)(1+f_2)(1+f_3)dx_1dx_2dx_3\right] \tag{7.34}$$

$$= \varepsilon\left[\int_0^L\int_0^L\int_0^L G(x_1,x_2,x_3)(1+f_1+f_2+f_3+f_1f_2+f_1f_3+f_2f_3+f_1f_2f_3)dx_1dx_2dx_3\right]$$

$$= \int_0^L\int_0^L\int_0^L G(x_1,x_2,x_3)(1+\varepsilon[f_1f_2]+\varepsilon[f_1f_3]+\varepsilon[f_2f_3]+\varepsilon[f_1f_2f_3])dx_1dx_2dx_3$$

where $G(x_1,x_2,x_3) = x_1(x_1-L)^2x_2(x_2-L)^2(x_3-L)^2$.

The following approximation is now implemented in Eq. (7.34), as well as in all subsequent equations. As stochastic field *f*(*x*) is fluctuating around zero and is assumed to have a relatively small variance, all expectations of order three and above (i.e. $\varepsilon[f_if_jf_k]$, $\varepsilon[f_if_jf_kf_l]$, …) will be considered infinitesimally small and will be disregarded. Consequently, Eq. (7.34) is rewritten as:

$$\varepsilon[X^2Y] \approx \int_0^L\int_0^L\int_0^L G(x_1,x_2,x_3)(1+R(x_1-x_2)+R(x_1-x_3)+R(x_2-x_3))dx_1dx_2dx_3 \tag{7.35}$$

Using the Wiener-Khintchine transform on the autocorrelation functions in Eq. (7.35) leads to:

$$\begin{aligned}
\varepsilon[X^2Y] &= C_4 + \int_0^L\int_0^L\int_0^L G(x_1,x_2,x_3)\int_{-\infty}^{+\infty} S_{ff}(\kappa)e^{i(x_1-x_2)}d\kappa dx_1dx_2dx_3 \\
&\quad + \int_0^L\int_0^L\int_0^L G(x_1,x_2,x_3)\int_{-\infty}^{+\infty} S_{ff}(\kappa)e^{i(x_1-x_3)\kappa}d\kappa dx_1dx_2dx_3 \\
&\quad + \int_0^L\int_0^L\int_0^L G(x_1,x_2,x_3)\int_{-\infty}^{+\infty} S_{ff}(\kappa)e^{i(x_2-x_3)\kappa}d\kappa dx_1dx_2dx_3 \\
&= C_4 + \int_0^L (x_3-L)^2 dx_3 \int_{-\infty}^{+\infty} S_{ff}(\kappa)\left(\int_0^L x_1(x_1-L)^2 e^{ix_1\kappa}dx_1\right)^2 d\kappa \\
&\quad + \int_0^L x_2(x_2-L)^2 dx_2 \int_{-\infty}^{+\infty} S_{ff}(\kappa)\left(\int_0^L x_1(x_1-L)^2 e^{ix_1\kappa}dx_1\right)\left(\int_0^L (x_3-L)^2 e^{-ix_3\kappa}dx_3\right)d\kappa \\
&\quad + \int_0^L x_1(x_1-L)^2 dx_1 \int_{-\infty}^{+\infty} S_{ff}(\kappa)\left(\int_0^L x_2(x_2-L)^2 e^{ix_2\kappa}dx_2\right)\left(\int_0^L (x_3-L)^2 e^{-ix_3\kappa}dx_3\right)d\kappa \\
&= C_4 + \int_{-\infty}^{+\infty} S_{ff}(\kappa)\left[\alpha|V_2(\kappa)|^2 + 2\beta V_1(\kappa)\right]d\kappa
\end{aligned} \tag{7.36}$$

where $V_1(\kappa)$ and $V_2(\kappa)$ have been defined in Eqs. (7.17) and (7.21), respectively, and:

$$C_4 = \int_0^L\int_0^L\int_0^L G(x_1,x_2,x_3)dx_1dx_2dx_3 = \alpha\beta^2 \tag{7.37}$$

The remaining five terms, $\varepsilon[XY^2]$, $\varepsilon[X^2Y^2]$, $\varepsilon[Y^3]$, $\varepsilon[XY^3]$, and $\varepsilon[Y^4]$ are calculated after some straightforward algebra (again disregarding terms of order three and higher) as:

$$\begin{aligned}
\varepsilon[XY^2] &= \varepsilon\left[\begin{array}{l}\displaystyle\int_0^L x_1(x_1-L)^2(1+f(x_1))dx_1 \cdot \int_0^L (x_2-L)^2(1+f(x_2))dx_2 \\ \displaystyle\cdot\int_0^L (x_3-L)^2(1+f(x_3))dx_3\end{array}\right] \\
&= \alpha^2\beta + \int_{-\infty}^{+\infty} S_{ff}(\kappa)\left[2\alpha V_1(\kappa) + \beta|V_3(\kappa)|^2\right]d\kappa
\end{aligned} \tag{7.38}$$

$$\varepsilon[X^2Y^2]=\varepsilon\left[\begin{array}{l}\int_0^L x_1(x_1-L)^2(1+f(x_1))dx_1\cdot\int_0^L x_2(x_2-L)^2(1+f(x_2))dx_2\\ \cdot\int_0^L (x_3-L)^2(1+f(x_3))dx_3\cdot\int_0^L (x_4-L)^2(1+f(x_4))dx_4\end{array}\right] \tag{7.39}$$

$$=\alpha^2\beta^2+\int_{-\infty}^{+\infty} S_{ff}(\kappa)\left[\alpha^2\left|V_2(\kappa)\right|^2+4\alpha\beta V_1(\kappa)+\beta^2\left|V_3(\kappa)\right|^2\right]d\kappa$$

$$\varepsilon[Y^3]=\varepsilon\left[\begin{array}{l}\int_0^L (x_1-L)^2(1+f(x_1))dx_1\cdot\int_0^L (x_2-L)^2(1+f(x_2))dx_2\\ \cdot\int_0^L (x_3-L)^2(1+f(x_3))dx_3\end{array}\right] \tag{7.40}$$

$$=\alpha^3+\int_{-\infty}^{+\infty} S_{ff}(\kappa)\left[3\alpha\left|V_3(\kappa)\right|^2\right]d\kappa$$

$$\varepsilon[XY^3]=\varepsilon\left[\begin{array}{l}\int_0^L x_1(x_1-L)^2(1+f(x_1))dx_1\cdot\int_0^L (x_2-L)^2(1+f(x_2))dx_2\\ \cdot\int_0^L (x_3-L)^2(1+f(x_3))dx_3\cdot\int_0^L (x_4-L)^2(1+f(x_4))dx_4\end{array}\right] \tag{7.41}$$

$$=\alpha^3\beta+\int_{-\infty}^{+\infty} S_{ff}(\kappa)\left[3\alpha^2V_1(\kappa)+3\alpha\beta\left|V_3(\kappa)\right|^2\right]d\kappa$$

$$\varepsilon[Y^4]=\varepsilon\left[\begin{array}{l}\int_0^L (x_1-L)^2(1+f(x_1))dx_1\cdot\int_0^L (x_2-L)^2(1+f(x_2))dx_2\\ \cdot\int_0^L (x_3-L)^2(1+f(x_3))dx_3\cdot\int_0^L (x_4-L)^2(1+f(x_4))dx_4\end{array}\right] \tag{7.42}$$

$$=\alpha^4+\int_{-\infty}^{+\infty} S_{ff}(\kappa)\left[6\alpha^2\left|V_3(\kappa)\right|^2\right]d\kappa$$

Finally, substituting Eqs.,(7.15), (7.19) and (7.23), (7.36) and (7.38)-(7.42) into Eq. (7.33), yields the following expression for $\varepsilon[h^2]$:

$$\varepsilon[h^2]=\frac{\beta^2}{\alpha^2}+\int_{-\infty}^{+\infty} S_{ff}(\kappa)\frac{1}{\alpha^2}\left[\left|V_2(\kappa)\right|^2-\frac{4\beta}{\alpha}V_1(\kappa)+\frac{3\beta^2}{\alpha^2}\left|V_3(\kappa)\right|^2\right]d\kappa \tag{7.43}$$

Denoting now:

$$\mathrm{VRF}_2(\kappa) = \frac{1}{\alpha^2}\left(|V_2(\kappa)|^2 - \frac{4\beta}{\alpha} V_1(\kappa) + \frac{3\beta^2}{\alpha^2} |V_3(\kappa)|^2 \right) \tag{7.44}$$

results in the following VRF-based integral expression for the mean square of *h*:

$$\varepsilon[h^2] = h_m^2 + \int_{-\infty}^{+\infty} S_{ff}(\kappa)\mathrm{VRF}_2(\kappa) d\kappa \tag{7.45}$$

The mean square value of *h* in Eq. (7.45) is again real-valued following a similar reasoning as earlier.

Table A.1-Table A.4 in Appendix A summarize all the terms involved in the expressions established for $\varepsilon[h^2]$ using both a first-order and a second-order Taylor series expansion.

7.3 Estimation of mean and variance of bending moment *M*(*x*) and of corresponding Variability Response Functions

The last step consists of establishing VRF-based integral expressions for the mean and the variance of the bending moment *M*(*x*). The expression for the mean is given by Eq. (7.1):

$$\varepsilon[M(x)] = -\frac{q_0}{2}(x-L)(x-\varepsilon[h]) \tag{7.46}$$

where $\varepsilon[h]$ is provided in Eq. (7.12) for the case of a first-order Taylor series expansion, and in Eq. (7.32) for the case of a second-order Taylor series expansion. It should be pointed out that the first-order Taylor series formulation leads to a constant value for $\varepsilon[M(x)]$ that is independent of stochastic field *f*(*x*), while the second-order Taylor series formulation leads to a value for $\varepsilon[M(x)]$ that depends on stochastic field *f*(*x*).

To establish the expression for the variance of *M*(*x*) using Eq. (7.2), the following expression is used for $\varepsilon[h^2]$:

$$\varepsilon[h^2] = h_m^2 + \int_{-\infty}^{+\infty} S_{ff}(\kappa)\mathrm{VRF}(\kappa)d\kappa \tag{7.47}$$

where VRF(κ) in Eq. (7.47) is given in Eq. (7.27) for the case of a first-order Taylor series expansion, and in Eq. (7.44) for the case of a second-order Taylor series expansion.

Then, the expression for the variance of $M(x)$ is determined using Eq. (7.2) as:

$$\begin{aligned} Var[M(x)] &= \left(\frac{q_0}{2}(x-L)\right)^2 (\varepsilon[h^2] - (\varepsilon[h])^2) \\ &= \left(\frac{q_0}{2}(x-L)\right)^2 \left(h_m^2 + \int_{-\infty}^{+\infty} S_{ff}(\kappa)\mathrm{VRF}(\kappa)d\kappa - (\varepsilon[h])^2\right) \end{aligned} \tag{7.48}$$

<u>First-order Taylor series</u>

When first-order Taylor series is applied, the variance of $M(x)$ in Eq. (7.48) can be further simplified since $\varepsilon[h] = \frac{\beta}{\alpha} = h_m$ is constant:

$$\begin{aligned} Var[M(x)] &= \left(\frac{q_0}{2}(x-L)\right)^2 \left(h_m^2 + \int_{-\infty}^{+\infty} S_{ff}(\kappa)\mathrm{VRF}(\kappa)d\kappa - (\varepsilon[h])^2\right) \\ &= \left(\frac{q_0}{2}(x-L)\right)^2 \int_{-\infty}^{+\infty} S_{ff}(\kappa)\mathrm{VRF}(\kappa)d\kappa \end{aligned} \tag{7.49}$$

If the scaling term $\left(\frac{q_0}{2}(x-L)\right)^2$ in the above equation is incorporated inside the VRF (Eq. (7.27)), then a standard form can be established for the variance of the response bending moment, as originally proposed by Shinozuka [52] in Eq. (6.1):

$$Var[M(x)] = \int_{-\infty}^{+\infty} S_{ff}(\kappa)\mathrm{VRF}_1'(\kappa, x)d\kappa \tag{7.50}$$

where

$$\mathrm{VRF}_1'(\kappa, x) = \left(\frac{q_0}{2\alpha}(x-L)\right)^2 \left(|V_2(\kappa)|^2 - \frac{2\beta}{\alpha}V_1(\kappa) + \frac{\beta^2}{\alpha^2}|V_3(\kappa)|^2\right) \tag{7.51}$$

Second-order Taylor series

For the second-order Taylor series case, the expression for $Var[M(x)]$ in Eq. (7.48) cannot be reduced into a form involving a single Variability Response Function as was done for the first-order Taylor series expansion in Eqs. (7.50)-(7.51). For the second-order Taylor series case, in addition to the VRF in the term $\int_{-\infty}^{+\infty} S_{ff}(\kappa)\mathrm{VRF}(\kappa)d\kappa$ in Eq. (7.48), there is another VRF inside the expression for $\varepsilon[h]$ as can be seen in Eq. (7.32) (i.e., $\mathrm{VRF}_{\mathrm{mean}}$). However, this expression for the variance of $M(x)$ involving two VRF's can still be used to estimate $Var[M(x)]$ with the same level of computational efficiency.

It should be pointed out that the first-order Taylor series formulation leads to an expression for $Var[M(x)]$ of the same form as the classic one shown in Eq. (6.1) that involves a single integral. In contrast, the second-order Taylor series formulation leads to a fundamentally different expression for $Var[M(x)]$ that involves two distinct integrals (still retaining all the advantages of the classic formulation shown in Eq. (6.1) involving a single integral).

7.4 Numerical examples

7.4.1 Response variability of bending moment M(x)

Consider the statically indeterminate beam of length L = 5m shown in Figure 6.1(a), carrying a deterministic uniformly distributed load q_0 = 1,000 N/m. The beam's elastic modulus is assumed to vary randomly along its length, with its inverse modeled as a homogenous stochastic field $f(x)$

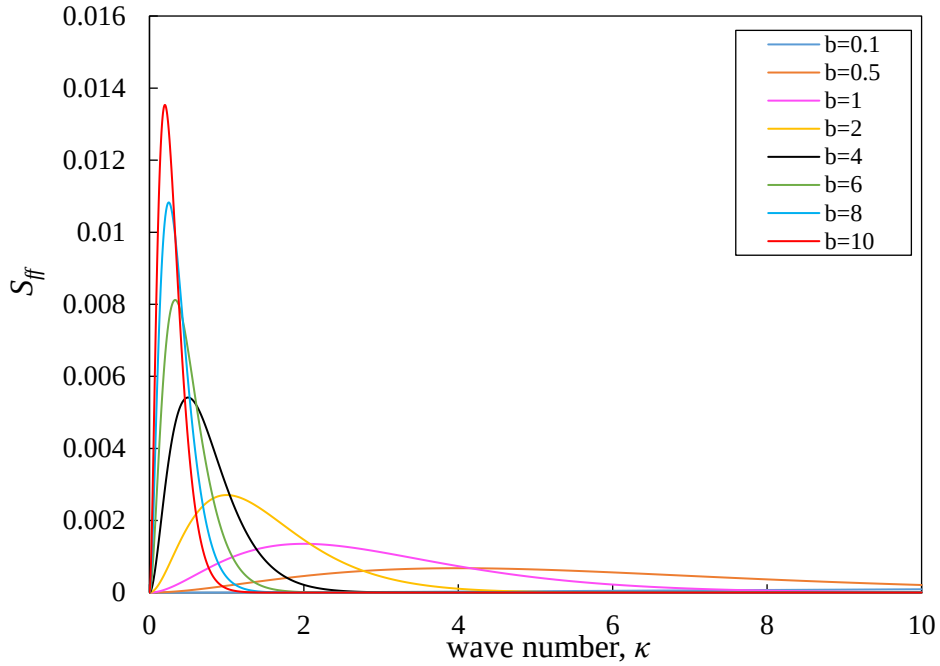

Figure 7.1: Spectral density function $S_{ff}(\kappa)$ in Eq. (6.18) plotted for different values of b

according to Eq. (6.2). The mean value of the beam's stiffness is set equal to E_0I = 2.8125 10^6 N·m^2. The form of the spectral density function of stochastic field $f(x)$ is defined in Eq. (6.18) with its two constants taking the following values: $\sigma_{ff} = 0.1$ and $b = 1$m (a parametric analysis will also be performed later with respect to b). The spectral density function $S_{ff}(\kappa)$ is plotted in Figure 7.1 for a few different values of b. When performing Monte Carlo simulations to demonstrate the accuracy of the VRF-based integral expressions for the response variance (Eq.(7.48)), the stochastic field $f(x)$ is modeled as both truncated Gaussian and lognormally distributed. For both probability distributions, their mean value is zero and standard deviation $\sigma_{ff} = 0.1$. The lognormal distribution is shifted to satisfy the zero-mean value. This way, it is not possible to have negative values of the beam's stiffness when using either distribution. For simulation purposes, the spectral representation method is used to generate sample functions of the truncated Gaussian field and the methodology proposed by Shields et al. [47] for the shifted lognormal field.

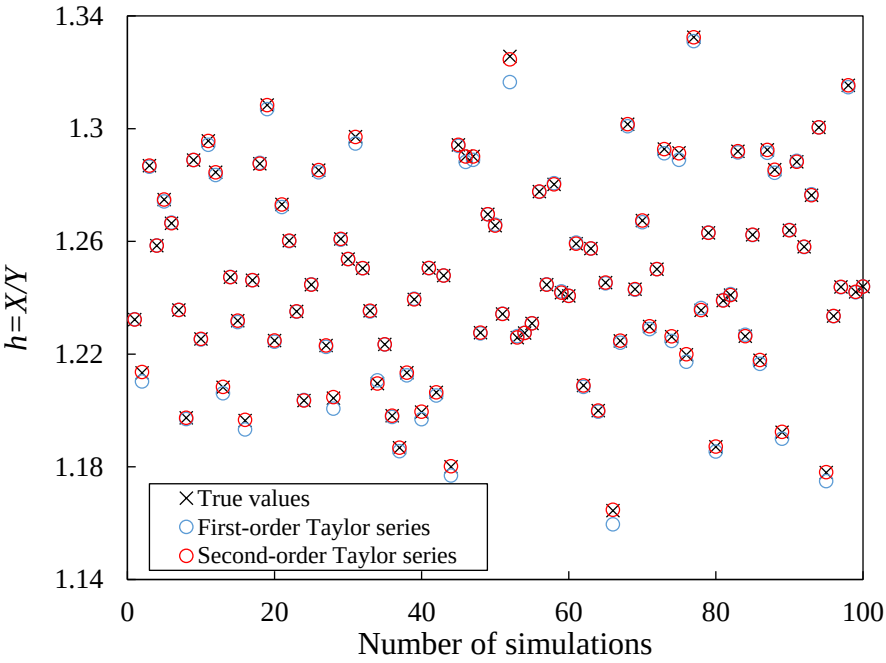

(a) Truncated Gaussian field

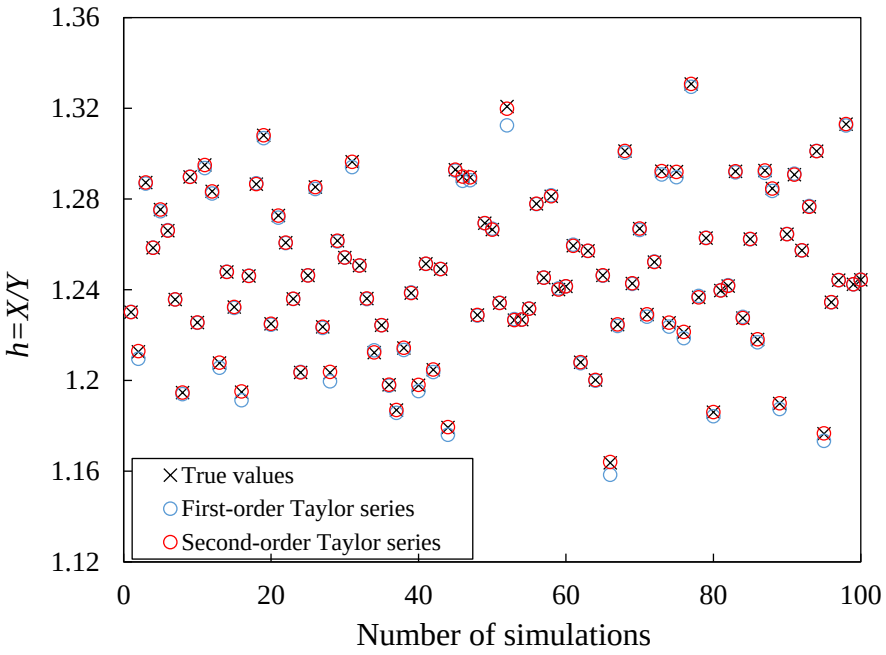

(b) Shifted lognormal field

Figure 7.2: Accuracy of first- and second-order Taylor series approximations of h values

As the accuracy of the bending moment VRF's in Eq. (7.48) (given by Eqs. (7.27) and (7.44)) directly depends on the accuracy of the two Taylor series approximations of X/Y in Eqs. (7.10) and

(7.30), the accuracy of the *X*/*Y* expansions is examined first. This is accomplished using 100 sample functions of stochastic field *f*(*x*) generated according to the probabilistic characteristics provided in the previous paragraph. Figure 7.2 displays and compares the exact values of h (computed via direct integration of Eq. (6.17)), with the corresponding values from the first-order (Eq. (7.10)) and second-order (Eq. (7.30)) Taylor series expansions. Figure 7.2 (a) is for the truncated Gaussian field and Figure 7.2 (b) for the shifted lognormal field. Figure 7.2 indicates that the first-order approximation is very good, while the second-order one is excellent.

The next step in assessing the relative accuracy of the two Taylor series approximations involves the calculation of $\varepsilon[h]$ and $\varepsilon[h^2]$. Table 7.1 displays values of $\varepsilon[h]$ and $\varepsilon[h^2]$ computed using the integral expressions involving Variability Response Functions (Eqs. (7.12) and (7.32) for $\varepsilon[h]$ and Eqs. (7.26) and (7.43) for $\varepsilon[h^2]$). For comparison, brute force Monte Carlo simulation results are also provided with both truncated Gaussian and shifted lognormal stochastic fields. Table 7.1 indicates that the first-order approximation is very good, while the second-order one is

Table 7.1: Comparison of $\varepsilon[h]$ and $\varepsilon[h^2]$ values calculated using the integral expressions involving Variability Response Functions and brute force Monte Carlo simulations

Method		$\varepsilon[h]$	$\varepsilon[h^2]$
VRF	First-order Taylor series	1.25	1.5638
	Second-order Taylor series	1.2508	1.5658
10 million Monte Carlo simulations (truncated Gaussian distribution)		1.2508	1.5658
10 million Monte Carlo simulations (shifted lognormal distribution)		1.2508	1.5658

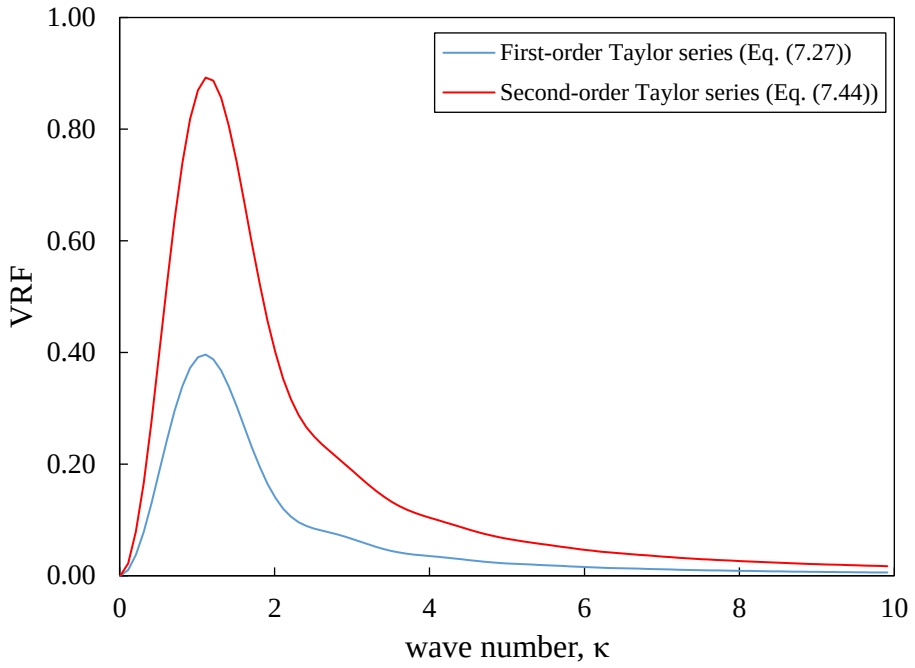

Figure 7.3: First- and second-order Taylor series VRFs associated with $\varepsilon[h^2]$

essentially perfect. It is also interesting to note that the Monte Carlo simulation results for truncated Gaussian and shifted lognormal fields coincide, providing the first indication that the VRF-based results are probability-distribution-independent. Figure 7.3 displays the first- and second-order Taylor series VRFs associated with $\varepsilon[h^2]$ (i.e., Eqs. (7.27) and (7.44)).

Eqs. (7.46) and (7.48) are eventually used to calculate the mean, variance and coefficient of variation of the bending moment $M(x)$ at two locations along the length of the beam: $x = \frac{L}{5} = 1.0\ m$ and $x = \frac{L}{2} = 2.5\ m$. Table 7.2 displays the results for the response variability of the bending moment calculated using the integral expressions involving Variability Response Functions (Equations (7.46) and (7.48)) and brute force Monte Carlo simulations. Table 7.2 indicates an excellent agreement between the MCS estimates (both truncated Gaussian and shifted lognormal) and the corresponding ones based on the Taylor series approximations. All results in Table 7.1 and Table 7.2 are established using the spectral density function in Eq. (6.18) with $\sigma_{ff} = 0.1$ and $b = 1$.

Table 7.2: Response variability of bending moment $M(x)$ at x=1m and x=2.5m calculated using the integral expressions involving Variability Response Functions and brute force Monte Carlo simulations.

Method	$M(x=1\text{m})$			$M(x=2.5\text{m})$		
	Mean	**Standard deviation**	**COV**	**Mean**	**Standard deviation**	**COV**
VRF (first-order Taylor series)	500	71.947	0.1439	-1562.50	44.967	0.0288
VRF (second-order Taylor series)	501.59	71.929	0.1434	-1561.51	44.956	0.0288
10 million MCS (truncated Gaussian)	501.57	72.183	0.1439	-1561.52	45.114	0.0289
10 million MCS (shifted lognormal)	501.67	71.952	0.1434	-1561.52	44.970	0.0288

Figure 7.4 and Figure 7.5 provide the same results as those in Table 7.2 (namely mean, variance and coefficient of variation of the bending moment $M(x)$ at the same two locations along the length of the beam), but now for a range of different values of parameter b appearing in the expression for the spectral density function. The results in Figure 7.4 and Figure 7.5 indicate that the second-order Taylor series approximation yields consistently excellent matches to the corresponding MCS estimates (while the first-order Taylor series results can have some deviations from the corresponding MCS values).

The Monte Carlo simulation results for truncated Gaussian and shifted lognormal fields in Table 7.2 and Figure 7.4 and Figure 7.5 provide a strong indication that the corresponding VRF-based results are probability-distribution-independent.

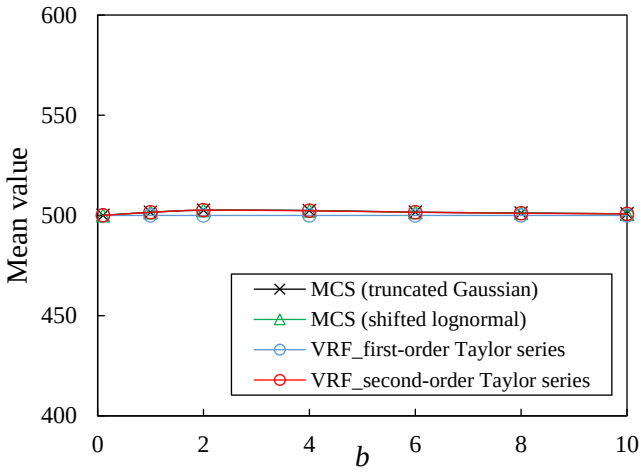

(a) Mean value

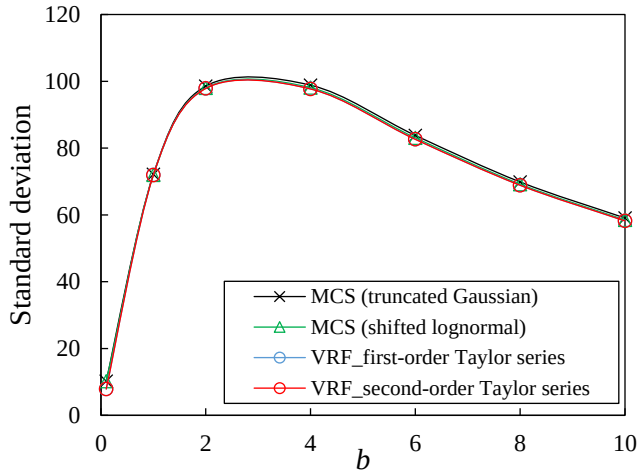

(b) Standard deviation

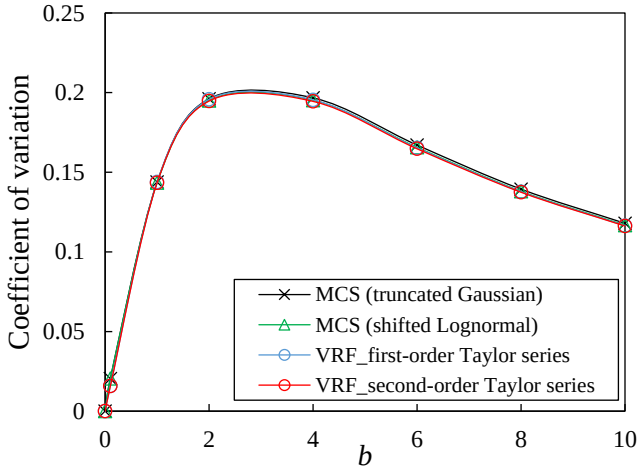

(c) Coefficient of variation

Figure 7.4: Mean, standard deviation and coefficient of variation of bending moment $M(x)$ at x=1m for a range of different values of parameter b appearing in the expression of the spectral density function

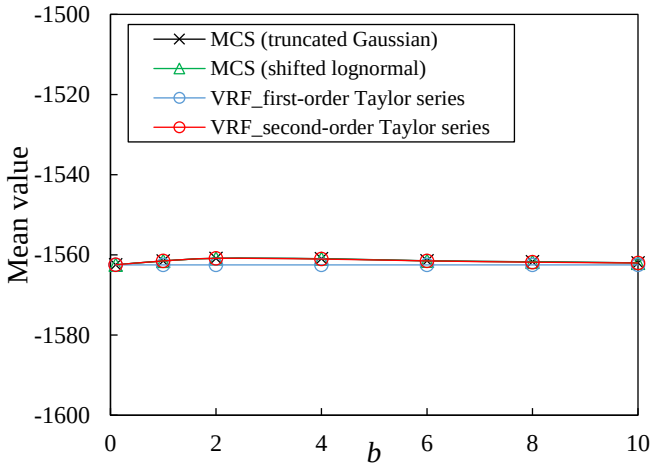

(a) Mean value

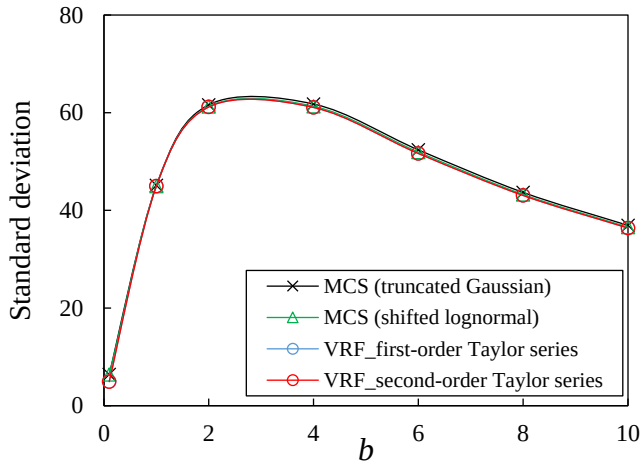

(b) Standard deviation

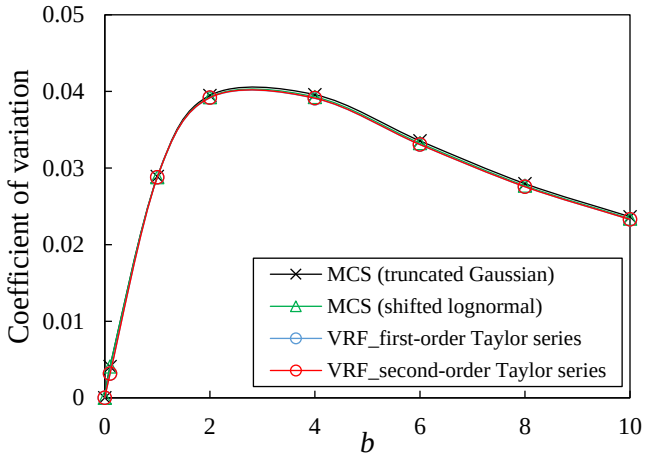

(c) Coefficient of variation

Figure 7.5: Mean, standard deviation and coefficient of variation of bending moment $M(x)$ at x=2.5m for a range of different values of parameter b appearing in the expression of the spectral density function

7.4.2 Upper bounds on response variability of bending moment M(x) using the VRF

The main advantage of the Variability Response Function is that it can be used to determine the response variability (i.e. mean, standard deviation and coefficient of variation) of the bending moment $M(x)$ through simple and computationally extremely efficient integrations (see Eqs. (7.46) and (7.48)). This makes possible the performance of full sensitivity analyses of the response variability with respect to the form of the spectral density function of stochastic field $f(x)$. A small example of this is presented in Figure 7.4 and Figure 7.5 where the response variability of the bending moment $M(x)$ is calculated for a number of different values of parameter b appearing in the expression for the spectral density function (corresponding to a number of different shapes of the spectral density function as seen in Figure 7.1).

An interesting exercise is to compare the coefficient of variation of the uncertain material properties (in this case 10%) to the corresponding coefficient of variation of the response bending moment. Such a comparison reveals how much is the system uncertainty (input uncertainty) affecting the response bending moment uncertainty (output uncertainty). Figure 7.4 and Figure 7.5 indicate that the coefficient of variation of the response bending moment can become as high as around 20% (double the 10% level of uncertainty of the input material properties). This can be seen occurring at location $x = 1m$ for values of parameter b between approximately 2 and 3 (refer to Figure 7.4(c)).

Figure 7.4 and Figure 7.5 consider only one expression of the spectral density function (Eq. (6.18)). It would be very interesting to know which specific form of the spectral density function yields the overall highest possible coefficient of variation of the response bending moment at various locations along the length of the beam (for the prescribed variance of $\sigma_{ff} = 0.1$).

For the first-order Taylor series case, it's straightforward to determine the upper bound of the

response variability as a standard form is available (see Eq. (7.50)). Deodatis and Shinozuka [55] have already determined that the spectral distribution-free upper bound for the response variability is obtained from the following power spectral density function:

$$S_{ff}(\kappa) = \frac{1}{2}\sigma_{ff}^2\,\delta(\kappa - \kappa^*) \tag{7.52}$$

where δ is Dirac's delta function and κ* is the wave number where VRF_1' in Eq. (7.50) takes its maximum value. Then, the upper bound of the response variability is given by:

$$Var[M(x = x_B)] \le \sigma_{ff}^2 \cdot \mathrm{VRF}_1'(x_B, \kappa^*) \tag{7.53}$$

Using this approach, the upper bound of the coefficient of variation of the response bending moment at location $x = 1m$ is determined as 25.2% (the corresponding wavenumber is κ*=1.1).

For the second-order Taylor series case, there is no standard form available like the one in Eq. (7.50). Equation (7.48) indicates that the upper bound of the response variance is directly related to the maximum value of $(\varepsilon[h^2] - \varepsilon[h])$:

$$Var[M(x)] = \left(\frac{q_0}{2}(x-L)\right)^2 (\varepsilon[h^2] - (\varepsilon[h])^2) \le \left(\frac{q_0}{2}(x-L)\right)^2 \cdot \max(\varepsilon[h^2] - (\varepsilon[h])^2) \tag{7.54}$$

The integral expressions for $\varepsilon[h^2]$ and $\varepsilon[h]$ in Eq. (7.54) are provided in Eqs. (7.45) and (7.32) respectively. The two VRF's in Eqs. (7.45) and (7.32) are plotted in Figure 7.6, where it can be observed that their maximum values occur at neighboring wave number values. A value for $\max(\varepsilon[h^2] - (\varepsilon[h])^2)$ can be easily established numerically by considering the spectral density function $S_{ff}(\kappa)$ becoming a Dirac delta function as in Eq. (7.52), and then calculating $(\varepsilon[h^2] - (\varepsilon[h])^2)$ for all wave number values between 0 and 10 (refer to Figure 7.6). The maximum of these computed values of $(\varepsilon[h^2] - (\varepsilon[h])^2)$ can be used to establish the upper bound for the variance of the response bending moment according to Eq. (7.54).

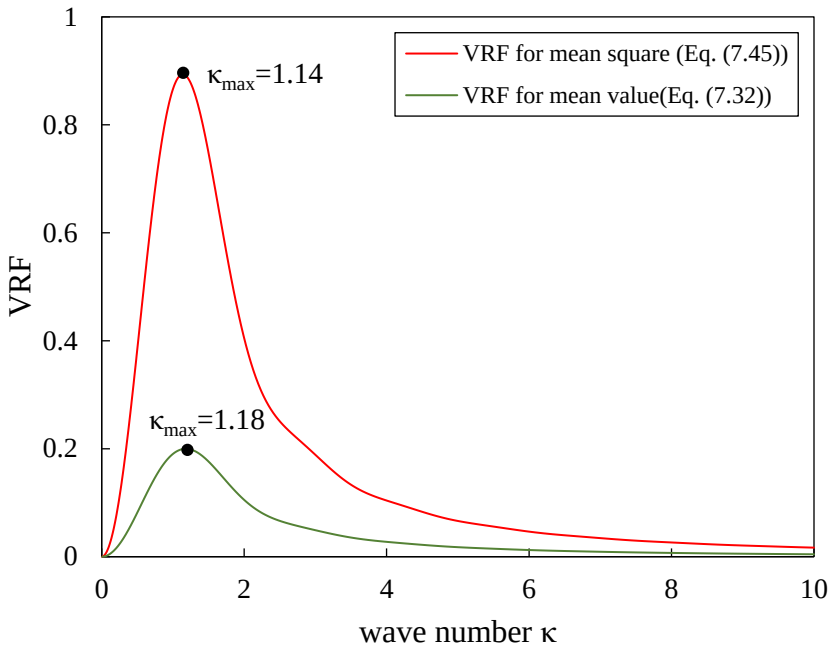

Figure 7.6: Second-order Taylor series Variability Response Functions for the mean square of *h* and for the mean value of *h*.

Using this approach, the upper bound of the coefficient of variation of the response bending moment at location $x = 1m$ is determined as 25% (the corresponding wave number is κ*=1.09). This estimated upper bound and corresponding wave number are essentially identical to those obtained from the first-order Taylor series (25.2% and 1.10).

It should be pointed out that these upper bounds on the variability of the response bending moment are realizable (i.e. the stochastic fields producing them are known).

7.4.3 First-order versus second-order Taylor series expansion formulations

Although all results in the previous two sections indicate that the first-order and second-order Taylor series formulations yield results that are very close to each other (and to Monte Carlo simulations), it is still recommended to always use the second-order Taylor series formulation. The reason for this recommendation is that the first-order Taylor series formulation lacks two important

attributes: (i) two distinct integrals in the expression for $Var[M(x)]$, and (ii) an expression for $\varepsilon[M(x)]$ that depends on stochastic field $f(x)$. Contrary to the results presented in this dissertation, there might be different problems where the lack of these two attributes might produce results that have a more significant error when using the first-order Taylor series approximation.

7.4.4 Proposed method for complex structures

For more complex structure with higher degrees of indeterminacy, e.g., statically indeterminate frames and plates, there are multiple zero bending moment locations within the structure, and hence more random variables are introduced corresponding to the zero bending moment locations h_1, h_2,…, h_n. The probabilistic characteristics of these random variables are estimated either by solving the governing equation of the structure similar with the expression of h in Eq (6.17) as a function of stochastic field $f(x)$, or solving numerically with Stochastic Finite Element method. Then, the expression of bending moments $M(x)$ is derived in terms of the random variables h_1, h_2,…, h_n so that the VRFs and response variability can be obtained accordingly using the similar procedure described in this chapter.

Chapter 8 Variability Response Function for Deflections

This chapter works on the Variability Response Function of another very important type of response for statically indeterminate structures, i.e., displacement (or deflection for beams). The property is directly related to the safety of structures, and hence it has been closed studied by many researchers over the years [52-55, 58-61]. In this chapter, the statically indeterminate structure can be transformed to its equivalent statically determinate structure. An approximate close-form analytical Variability Response Function is then built based on the transformed statically determinate structure. Moreover, to get more accurate estimates of the original statically indeterminate system, the results from Variability Response Function can be further revised by introducing a correction term *Dw*. Finally, incorporating the *Dw* function as well as the estimates from Variability Response Function into the correction function, the corrected response variability of the original statically indeterminate structure can be obtained.

8.1 Equivalent statically determinate structure with random location of hinge

From the deflection function in Eq. (6.13), It takes two more integrations to obtain deflection w(x) from bending moment M(x), which means that there exists a nonlinear relationship between w(x) and M(x). Therefore, although the VRFs of M(x) are well-defined in Chapter 7, there is still no straightforward way to obtain the closed-form analytical expressions of the variability of w(x) by the proposed VRFs of bending moment. As described in Chapter 7, the statically indeterminate structure in Figure 6.1(a) will have a bending moment diagram with a location where the moment will be equal to zero (this applies to structures with both constant and varying material properties along the length of the beam). If a hinge is introduced at this location of zero bending moment, the original statically indeterminate structure becomes statically determinate as shown in Figure

6.1(b). The original statically indeterminate structure in Figure 6.1 (a) and the corresponding statically determinate one in Figure 6.1 (b) are perfectly equivalent, in the sense that they will have the exact same bending moment diagrams and exact same deflection diagrams. This equivalence property holds for beams with both constant and varying material properties along their length as will be shown later in this section.

The distance of the hinge from the left end of the beam is denoted by h as can be seen in Figure 6.1(b). When Young's modulus is deterministic and constant over the entire length of the beam, i.e., $E(x) = E_0$ for $x \in [0, L]$, conventional structural analysis provides the location of the hinge as: $h = h_m = L/4$. However, when $1/E(x)$ is modeled as a stochastic field according to Eq. (6.2), the values of $1/E(x)$ will be changing from location to location along the length of the beam and, in principle, it is possible to have an infinity of different realizations of $1/E(x)$ over the length of the structure. Each one of these realizations of $1/E(x)$ will yield a different location for the zero moment and subsequently for the location of the hinge h. This means that h becomes a random variable.

It was mentioned earlier that the original statically indeterminate structure in Figure 6.1(a) and the corresponding statically determinate one in Figure 6.1(b) are perfectly equivalent. This is a well-known fact for structures with deterministic and constant material properties. In order to demonstrate that this perfect equivalence holds also for structures with material properties varying along their length, the following procedure is used:

1) The statically indeterminate beam shown in Figure 6.1(a) is divided into N finite elements of equal size.
2) A realization of stochastic field $f(x)$ (refer to Eq. (6.2)) is generated along the length of the beam according to its prescribed probabilistic characteristics.

3) The resulting statically indeterminate beam is solved using the finite element method, and the location of zero moment is determined.
4) The corresponding statically determinate beam is established by introducing a hinge at the location determined in step 3).
5) The corresponding statically determinate beam established in step 4) is also divided into the same *N* finite elements and solved with the exact same realization of stochastic field *f(x)* generated in step 2).
6) Bending moments and deflections of the two beams (statically indeterminate and corresponding statically determinate) are compared.

The six-step procedure described above was implemented several times for different realizations of stochastic field $f(x)$ following different probabilistic characteristics, and every time, the bending moments and deflections of the two beams were found to be identical.

8.2 Derivation of Variability Response Function with determinate *h*

8.2.1 Mean and variance functions for Beam AB

Consider the governing equation of statically determinate Euler-Bernoulli Beam AB in Figure 6.1(b) and boundary conditions:

$$\begin{cases} \dfrac{d^2}{dx^2}\left(E(x)I\dfrac{d^2 w_1}{dx^2} \right) = q_0 \\ w_1(x=0)=0 \\ \dfrac{dw_1}{dx}(x=0)=0 \\ M_1(x=h)=0 \end{cases} \tag{8.1}$$

Similar with solving governing equations of original statically indeterminate structure in Section 6.2, the moment $M_1(x)$ and deflection $w_1(x)$ can be obtained by integration:

$$M_1(x) = -\frac{q_0}{2}(x-h)(x-L) \tag{8.2}$$

$$w_1(x) = -\int_0^x \int_0^{x_1} \frac{M_1(x_2)}{E(x_2)I} dx_2 dx_1 = \frac{q_0}{2} \int_0^x \int_0^{x_1} \frac{(x_2-h)(x_2-L)}{E(x_2)I} dx_2 dx_1 \tag{8.3}$$

Note that there are two random variables in the deflection function: $E(x)$ and h. Developing the joint distribution of $E(x)$ and h is extremely difficult and the most direct way is by Monte Carlo simulation, which is time-consuming and has to be performed every time when a different type of stochastic field $f(x)$ is applied. Therefore, Variability Response Function provides a more general and efficient way to estimate the response variability.

Take the expectation of Eq. (8.3), since when $E(x)$ is taken at its mean value, i.e., $E(x) = E_0$, h is automatically obtained with $h=h_m$, which represents the beam with constant material property. Then the mean of $w_1(x)$ is expressed as:

$$\begin{aligned} \varepsilon[w_1(x)] &= \varepsilon\left[\frac{q_0}{2}\int_0^x \int_0^{x_1} \frac{(x_2-h)(x_2-L)}{E(x_2)I} dx_2 dx_1\right] \\ &= \frac{q_0}{2}\int_0^x \int_0^{x_1} \frac{(x_2-h_m)(x_2-L)}{E_0 I} dx_2 dx_1 = \frac{q_0}{24E_0 I} x^2(6h_m L - 2h_m x - 2Lx + x^2) \end{aligned} \tag{8.4}$$

For variance, let's first consider the response variability of $w_1(x)$ under certain value of h, i.e., $h=h_0$. And the variance is given as:

$$\begin{aligned} &Var[w_1(x) \mid h = h_0] = \varepsilon[(w_1(x) - \varepsilon[w_1(x)])^2] \\ &= \varepsilon\left[\left(\int_0^x \int_0^{x_1} \frac{M_1(x_2)}{E(x_2)I} dx_2 dx_1 - \int_0^x \int_0^{x_1} \frac{M_1(x_2)}{E_0 I} dx_2 dx_1\right)^2\right] = \frac{1}{(E_0 I)^2} \int_0^x \int_0^x Z_1(x_1, x_2) dx_2 dx_1 \end{aligned} \tag{8.5}$$

where $Z_1(x_1, x_2) = \int_0^{x_1} \int_0^{x_2} R_{ff}(x_3 - x_4) M_1(x_3) M_1(x_4) dx_3 dx_4$ and $R_{ff}(x_3 - x_4)$ is the autocorrelation function of the stochastic field $f(x)$ defined in Eq. (6.2). Using the Wiener-Khintchine transform, $Z_1(x_1, x_2)$ can be further expressed as

$$
\begin{aligned}
Z_1(x_1,x_2) &= \int_0^{x_1}\int_0^{x_2}\int_{-\infty}^{+\infty} S_{ff}(\kappa)e^{i(x_3-x_4)\kappa}d\kappa \bullet M_1(x_3)M_1(x_4)dx_3dx_4 \\
&= \int_{-\infty}^{+\infty} S_{ff}(\kappa)\int_0^{x_1}\int_0^{x_2} e^{i(x_3-x_4)\kappa}M_1(x_3)M_1(x_4)dx_3dx_4d\kappa \\
&= \int_{-\infty}^{+\infty} S_{ff}(\kappa)\left|\bar{V}_1(\kappa,x_1)\bar{V}_1(\kappa,x_2)\right|d\kappa
\end{aligned}
\tag{8.6}
$$

where $\bar{V}_1(\kappa,x)=\int_0^x e^{i\xi\kappa}M_1(\xi)d\xi$. Then, substituting $Z_1(x_1,x_2)$ into Eq.(8.5):

$$
\begin{aligned}
Var[w_1(x)\,|\,h=h_0] &= \frac{1}{(E_0I)^2}\int_0^x\int_0^x\int_{-\infty}^{+\infty} S_{ff}(\kappa)\left|\bar{V}_1(\kappa,x_1)\bar{V}_1(\kappa,x_2)\right|dx_1dx_2d\kappa \\
&= \frac{1}{(E_0I)^2}\int_{-\infty}^{+\infty} S_{ff}(\kappa)\int_0^x\int_0^x\left|\bar{V}_1(\kappa,x_1)\bar{V}_1(\kappa,x_2)\right|dx_1dx_2d\kappa \\
&= \int_{-\infty}^{+\infty} S_{ff}(\kappa)\left|\hat{V}_1(\kappa,x)\right|^2 d\kappa
\end{aligned}
\tag{8.7}
$$

where

$$
\hat{V}_1(\kappa,x)=\frac{1}{E_0I}\int_0^x \bar{V}_1(\kappa,x_1)dx_1=\frac{1}{E_0I}\int_0^x\int_0^{x_1} M_1(x_2)e^{ix_2\kappa}dx_2dx_1 \tag{8.8}
$$

Let the VRF of Beam AB for $h=h_0$ be

$$
\mathrm{VRF}_{AB,h_0}(\kappa,x)=\left|\hat{V}_1(\kappa,x)\right|^2 \tag{8.9}
$$

Then, the variance of $w_1(x)$ given $h=h_0$ can be written as

$$
Var[w_1(x)\,|\,h=h_0]=\int_{-\infty}^{+\infty} S_{ff}(\kappa)\mathrm{VRF}_{AB,h_0}(\kappa,x)d\kappa \tag{8.10}
$$

8.2.2 Mean and variance functions for Beam BC

For Beam BC, it has the following governing equation and boundary conditions:

$$\begin{cases} \dfrac{d^2}{dx^2}\left(E(x)I\dfrac{d^2 w_2}{dx^2} \right) = q_0 \\ w_2(x=h) = w_1(x=h) \\ w_2(x=L) = 0 \\ M_2(x=h) = 0 \\ M_2(x=L) = 0 \end{cases} \tag{8.11}$$

By solving the differential equation, we have the moment $M_2(x)$ and deflection function $w_2(x)$ as

$$M_2(x) = M_1(x) = -\frac{q_0}{2}(x-h)(x-L) \tag{8.12}$$

$$\begin{aligned} w_2(x) &= -\int_0^x \int_0^{x_1} \frac{M_2(x_2)}{E(x_2)I} dx_2 dx_1 + \frac{x-h}{L-h}\int_0^L \int_0^{x_1} \frac{M_2(x_2)}{E(x_2)I} dx_2 dx_1 \\ &= \frac{q_0}{2}\left[\int_0^x \int_0^{x_1} \frac{(x_2-h)(x_2-L)}{E(x_2)I} dx_2 dx_1 - \frac{x-h}{L-h}\int_0^L \int_0^{x_1} \frac{(x_2-h)(x_2-L)}{E(x_2)I} dx_2 dx_1 \right] \end{aligned} \tag{8.13}$$

Similarly, the expectation of $w_2(x)$ is

$$\begin{aligned} \varepsilon[w_2(x)] &= \varepsilon\left[-\int_0^x \int_0^{x_1} \frac{M_2(x_2)}{E(x_2)I} dx_2 dx_1 + \frac{x-h}{L-h}\int_0^L \int_0^{x_1} \frac{M_2(x_2)}{E(x_2)I} dx_2 dx_1 \right] \\ &= \frac{q_0}{2E_0 I}\left[\int_0^x \int_0^{x_1} (x_2-h_m)(x_2-L) dx_2 dx_1 - \frac{x-h_m}{L-h_m}\int_0^L \int_0^{x_1} (x_2-h_m)(x_2-L) dx_2 dx_1 \right] \\ &= \frac{q_0}{24E_0 I} \cdot \frac{-2h_m{}^2(2L^3 - 3Lx^2 + x^3) - Lx(L^3 - 2Lx^2 + x^3) + h_m(L^4 + 4L^3 x - 6L^2 x^2 + x^4)}{h_m - L} \end{aligned} \tag{8.14}$$

And the variance given that $h=h_0$ is

$$\begin{aligned} Var[w_2(x) \mid h = h_0] &= \varepsilon[(w_2(x) - \varepsilon[w_2(x)])^2] \\ &= \frac{1}{(E_0 I)^2}\left[\int_0^x \int_0^x Z_2(x_1, x_2) dx_2 dx_1 - 2\left(\frac{x-h_0}{L-h_0}\right)\int_0^L \int_0^x Z_2(x_1, x_2) dx_2 dx_1 \right. \\ &\quad \left. + \left(\frac{x-h_0}{L-h_0}\right)^2 \int_0^L \int_0^L Z_2(x_1, x_2) dx_2 dx_1 \right] \end{aligned} \tag{8.15}$$

where $Z_2(x_1,x_2)=\int_0^{x_1}\int_0^{x_2} R_{ff}(x_3-x_4)M_2(x_3)M_2(x_4)dx_3dx_4$. And by Wiener-Khintchine transform, the variance can be written as:

$$Var[w_2(x)\,|\,h=h_0]=\begin{bmatrix}\int_{-\infty}^{+\infty} S_{ff}(\kappa)\left(\hat{V}_2(\kappa,x)\right)^2 d\kappa-2\left(\frac{x-h_0}{L-h_0}\right)\int_{-\infty}^{+\infty} S_{ff}(\kappa)\left(\hat{V}_2(\kappa,x)\hat{V}_2(\kappa,L)\right)d\kappa\\ +\left(\frac{x-h_0}{L-h_0}\right)^2\int_{-\infty}^{+\infty} S_{ff}(\kappa)\left(\hat{V}_2(\kappa,L)\right)^2 d\kappa\end{bmatrix} \tag{8.16}$$

$$=\int_{-\infty}^{+\infty} S_{ff}(\kappa)\left|\hat{V}_2(\kappa,x)-\left(\frac{x-h_0}{L-h_0}\right)\hat{V}_2(\kappa,L)\right|^2 d\kappa$$

where

$$\hat{V}_2(\kappa,x)=\frac{1}{E_0I}\int_0^{x}\int_0^{x_1} M_2(x_2)e^{ix_2\kappa}dx_2dx_1 \tag{8.17}$$

Let

$$\mathrm{VRF}_{BC,h_0}(\kappa,x)=\left|\hat{V}_2(\kappa,x)-\left(\frac{x-h_0}{L-h_0}\right)\hat{V}_2(\kappa,L)\right|^2 \tag{8.18}$$

The variance of $w_1(x)$ given $h=h_0$ can also be written in the same form as in Eq. (8.10):

$$Var[w_2(x)\,|\,h=h_0]=\int_{-\infty}^{+\infty} S_{ff}(\kappa)\mathrm{VRF}_{BC,h_0}(\kappa,x)d\kappa \tag{8.19}$$

So far, we have derived the VRF based on the given value of h for both beams AB ($x \le h$) and BC ($x > h$). These VRFs depend only on the deterministic parameters related to geometry, material properties and loading of the structure. As mentioned in the previous section, h is also a random variable determined by stochastic field $f(x)$. Therefore, we will discuss the more general VRF with random variable h in the next section.

8.3 Ensemble average VRF for all possible values of *h*

In Section 6.2, large number of *h* samples can be generated by Eq. (6.17) or by SFEM, which depict the distribution of *h*. In order to find the VRF for the random variable *h*, all the possible values of *h* are incorporated into the functions derived above i.e., $\mathrm{VRF}_{AB,h0}(\kappa, x)$ (Eq. (8.9)) and $\mathrm{VRF}_{BC,h0}(\kappa, x)$ (Eq.(8.18)). Then take the ensemble average of all the VRFs, i.e.,

$$\mathrm{VRF}(\kappa, x) = \frac{1}{n}\sum_{i=1}^{n} \mathrm{VRF}_{h_i}(\kappa, x) \tag{8.20}$$

where *n* is the number of realizations and h_i (i=1, 2…, n) is the sample of *h* generated by Eq. (6.17) for ith realization of stochastic field $f(x)$. And the variance can be obtained by

$$Var[w(x)] = \int_{-\infty}^{+\infty} S_{ff}(\kappa)\mathrm{VRF}(\kappa, x)d\kappa \tag{8.21}$$

Figure 8.1(a) and (b) indicate the average VRFs at x=L/5 and x=L/2 with n=100, 500, 800, 1000. For comparison, it also shows the VRF at h= h_m =L/4 (i.e., $\mathrm{VRF}_{hm}(\kappa, x)$), which is the location with constant Young's modulus. The following values are used for the numerical analysis: q_0 = -1000 N/m; E_0I = 2.8125 10^6 N·m^2; L = 5 m; and power spectrum S_{ff} is defined in Eq. (6.18), with σ_{ff} = 0.1 and parameter b varying from 0 to 10.

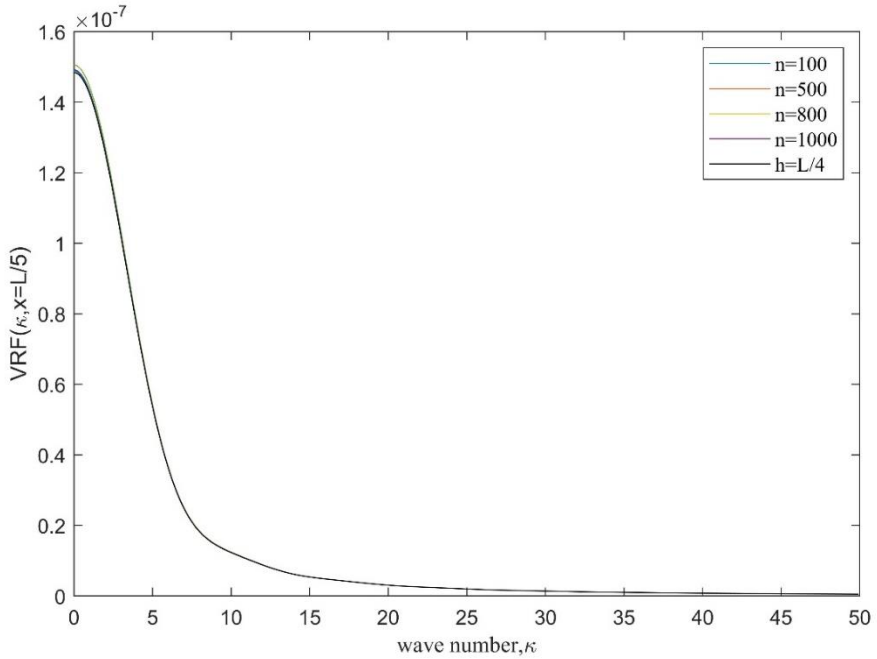

(a) Average VRF and VRF_{hm} at $x=L/5$

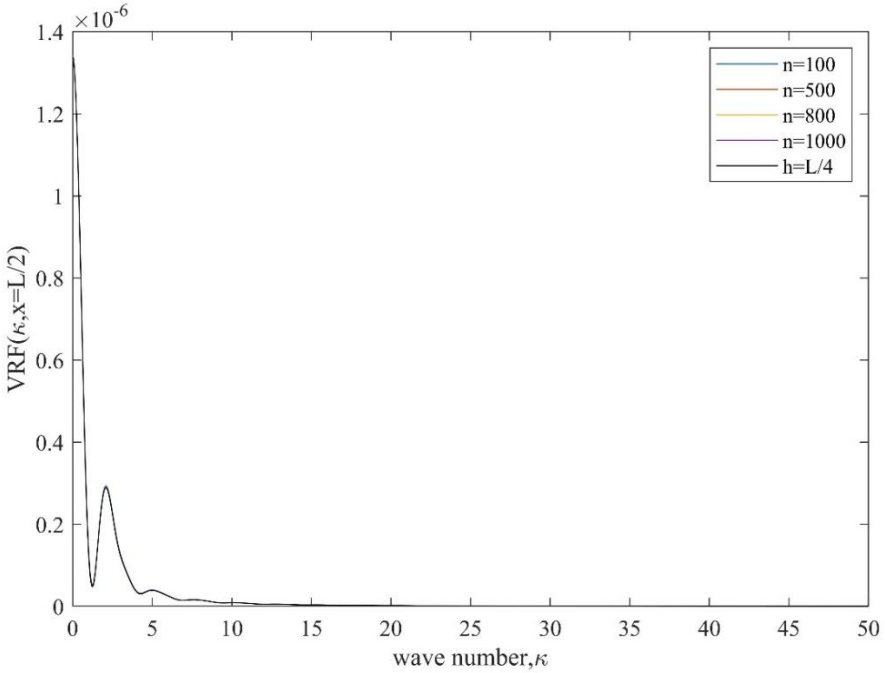

(b) Average VRF and VRF_{hm} at $x=L/2$

Figure 8.1: Comparison of average VRF and VRF_{hm} (i.e., VRF with $h=h_m=L/4$ in Eq (8.9) and (8.18))

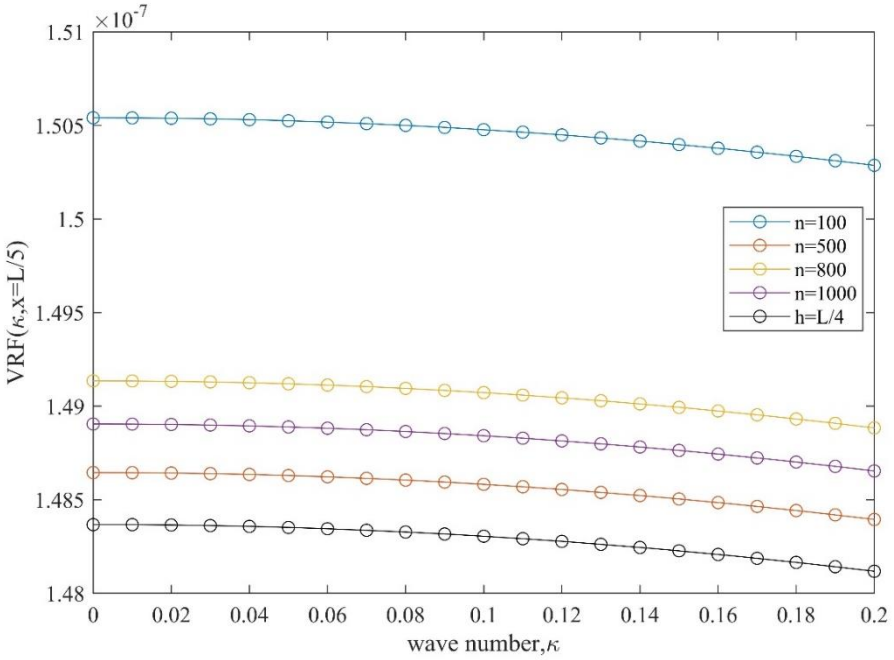

(a) Average VRF and VRF_{hm} at $x=L/5$ around maximum value points

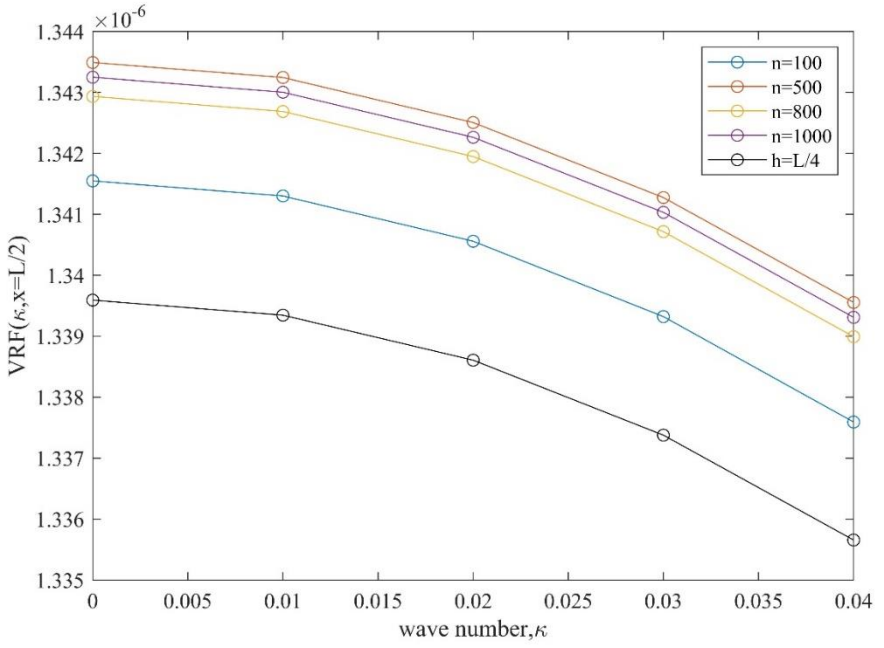

(b) Average VRF and VRF_{hm} at $x=L/2$ around maximum value points

Figure 8.2: Comparison of average VRF and VRF_{hm} around the maximum values

The average VRF converges very fast as n increases and has very tiny difference with the one of $h_m=L/4$, even at the maximum point $\kappa=0$ (see Figure 8.2(a) and (b)). The property is very important to obtain the final VRF, for it means that we can use the $\mathrm{VRF}_{hm}(\kappa, x)$ to approximately represent the average VRF when calculating the response variability of the structure in Eq. (8.21) , which takes only one time calculation by Eq. (8.8)-(8.9) or Eq. (8.17)-(8.18) instead of taking ensemble average of n realizations in Eq. (8.20).

Figure 8.3 shows the estimated variance $Var[w_1(x)]$ at $x=L/5$ by Eq. (8.21) with both average VRF of 1000 realizations and $\mathrm{VRF}_{hm}(\kappa, x)$. It also displays the variance by direct Monte Carlo simulation. It's demonstrated that the average VRF and VRF_{hm} give similar estimates of the response variability, while the use of VRF_{hm} can largely save the computation cost of calculating average VRF. Although there is some distance between VRF estimates and direct MCS estimates (can be taken as true response variability when large quantity of samples applied), which can be observed in Figure 8.3, the VRF estimates can be taken as a good approximation toward the true

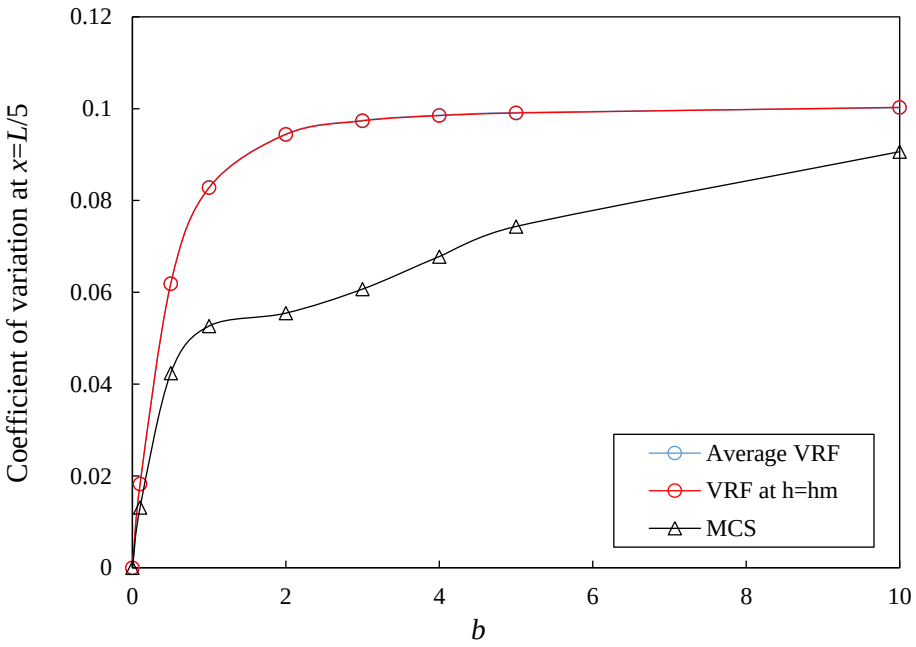

Figure 8.3: Coefficient of variation of the deflection at $x=L/5$ with varying parameter b

response variability of statically indeterminate structures with reasonable accuracy. Moreover, compared with direct MCS or SFEM, VRF has very excellent advantages of computational efficiency and generosity. Especially when VRF_{hm} is applied to skip the step of taking ensemble average of all VRFs, only one integration is needed using Eq. (8.21) instead of thousands of simulations in MCS. Besides, it can be used for arbitrary system properties as long as their probabilistic characteristics is assumed, reflected by spectral density function S_{ff}.

However, in some circumstances, more accurate prediction is needed and the results by VRF can be further revised. In the next part, the difference between VRF estimates and direct MCS will be explained by their physical meanings. Also, a correction term will be by introduced to get more accurate estimates of response variability.

8.4 Correction of Response Variability by VRF

8.4.1 Correction term Dw

In the analysis of statically indeterminate structures, it usually takes more than one random variable to take account the abundant indeterminacy apart from the original stochastic field of the material or loading. Shinozuka [52] introduced statically indeterminate forces and found the correlation and covariance matrix of the random variables. In this way, the response variability can only be obtained by simulations like MCS or approximated like FOSM. There is no analytical solution for the response variability of deflection $w(x)$. In the proposed approach, a random hinge is introduced located at zero-moment point, thus the location h becomes a random variable. To avoid estimating the joint distribution of h and $f(x)$, the VRF derived in the previous section is dependent on known h. Although an ensemble average is taken for all VRFs obtained from h samples, the structure represented by average VRF or it's substitution VRF_{hm} has some fundamental

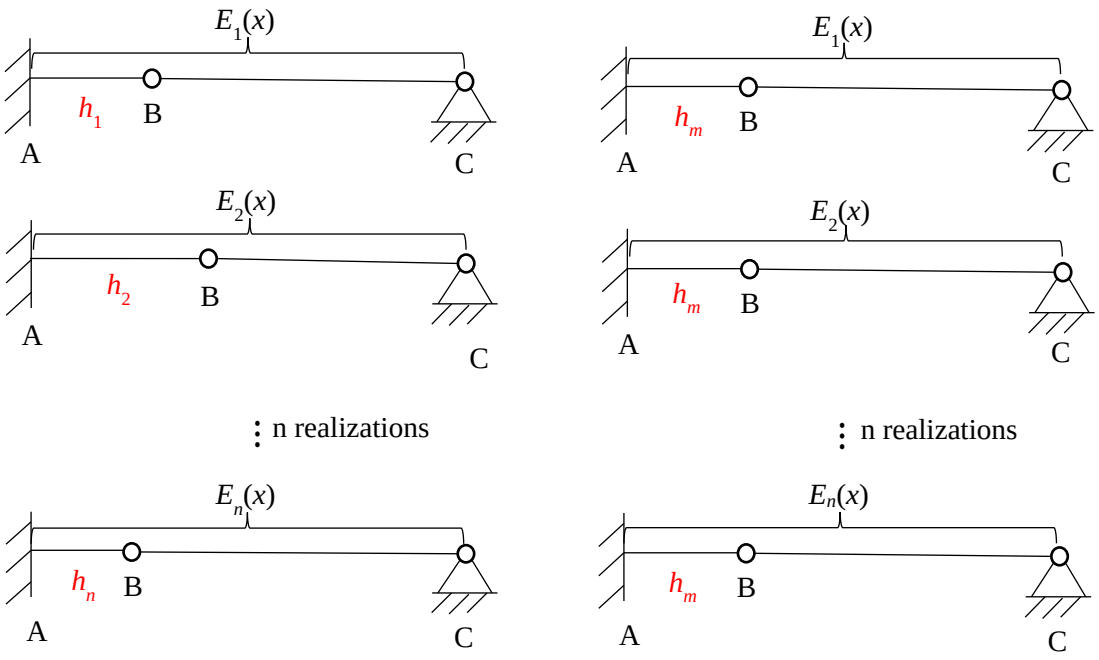

(a) Beam with random hinges (b) Beam with fixed hinge

Figure 8.4: Structural difference of the original statically determinate beam with random hinges and the beam with fixed hinge represented by derived VRF under the same n realizations of stochastic field f(x)

mechanical difference from the original statistically indeterminate beam. The main cause is the relationship between h and $f(x)$. From Eq. (6.17), we can conjecture a one-to-one relationship between h and stochastic field $f(x)$, as long as h value for each realization of $f(x)$ is taken as infinite decimal. However, the one-to-one dependence has been broken when deriving VRF by fixing h at some constant value, and hence the structure behind is also changed accordingly.

Figure 8.4 displays the structural difference based on the structure represented by the derived VRF and the true statically indeterminate beam. For the original statically indeterminate beam (Figure 8.4(a)), the hinge is placed at the zero-moment point for each realization of $f(x)$. While the VRF represents the beam (Figure 8.4(b)) with fixed hinge regardless of different realizations of $f(x)$. In other words, in Figure 8.4(a), h and $f(x)$ are one-to-one correspondence: a series of $f(x)$

along the length of the beam corresponds to one certain value of h. And in Figure 8.4(b), h is fixed for all realizations of $f(x)$. For example, if we use $h=h_m=L/4$ to represent the average VRF, the corresponding structure is the beam with fixed hinge at $h_m=L/4$ and it will not change with $f(x)$ in the simulations. Therefore, to get the actual response variability of the statically indeterminate beam, a correction term Dw is introduced here. Dw is then defined as the difference in deflection between the true statically indeterminate structure (Figure 8.4(a)) and the statically determinate structure with fixed hinge (Figure 8.4(b)), where the derived VRF at $h_m=L/4$ by Eq. (8.8)-(8.9) for beam AB and Eq. (8.17)-(8.18) for beam BC can be applied. Therefore, Dw is expressed as

$$Dw = w_{true} - w_m \tag{8.22}$$

where w_{true} is the true deflection of the statically indeterminant beam and w_m is the deflection of the statically determinate beam with a fixed hinge located at $h_m=L/4$. Then, the true response variability can be easily given as

$$\varepsilon[w_{true}] = \varepsilon[Dw + w_m] = \varepsilon[Dw] + \varepsilon[w_m] \tag{8.23}$$

$$Var[w_{true}] = Var[Dw + w_m] = Var[Dw] + Var[w_m] + 2\mathrm{COV}[Dw, w_m] \tag{8.24}$$

where COV[.] is the covariance. $\varepsilon[w_m]$ and $Var[w_m]$ can be obtained from VRF function (Eq. (8.4), (8.14) and (8.21)) without simulations. Therefore, the key is to find the statistics of Dw and its relationship with w_m.

8.4.2 Analytical function between Dw and h

Let's start with the definition of Dw in Eq. (8.22). w_{true} is the true deflection of the statically indeterminant beam and it can be expressed by Eq. (6.13) with random variable h. w_m is the deflection of the statically determinate beam with the fixed hinge at $h= h_m$=const.

- For Beam AB, w_m is defined by Eq.(8.3). Substitute both w_{true} and w_m into Eq. (8.22),

$$
\begin{aligned}
Dw_{AB} &= w_{true} - w_1(h = h_m) \\
&= \frac{q_0}{2}\int_0^x\int_0^{x_1}\frac{(x_2-h)(x_2-L)}{E(x_2)I}dx_2dx_1 - \frac{q_0}{2}\int_0^x\int_0^{x_1}\frac{(x_2-h_m)(x_2-L)}{E(x_2)I}dx_2dx_1
\end{aligned} \tag{8.25}
$$

- For Beam BC, w_m is defined by Eq. (8.13). And Dw can be written as

$$
\begin{aligned}
Dw_{BC} &= w_{true} - w_2(h = h_m) \\
&= \frac{q_0}{2}\int_0^x\int_0^{x_1}\frac{(x_2-h)(x_2-L)}{E(x_2)I}dx_2dx_1 - \frac{q_0}{2}\left[\begin{array}{l}\displaystyle\int_0^x\int_0^{x_1}\frac{(x_2-h_m)(x_2-L)}{E(x_2)I}dx_2dx_1 \\ \displaystyle-\frac{x-h_m}{L-h_m}\int_0^L\int_0^{x_1}\frac{(x_2-h_m)(x_2-L)}{E(x_2)I}dx_2dx_1\end{array}\right] \\
&= \frac{q_0}{2}\left[\begin{array}{l}\displaystyle\int_0^x\int_0^{x_1}\frac{(x_2-h)(x_2-L)}{E(x_2)I}dx_2dx_1 - \int_0^x\int_0^{x_1}\frac{(x_2-h_m)(x_2-L)}{E(x_2)I}dx_2dx_1 \\ \displaystyle+\frac{x-h_m}{L-h_m}\int_0^L\int_0^{x_1}\frac{(x_2-h_m)(x_2-L)}{E(x_2)I}dx_2dx_1\end{array}\right]
\end{aligned} \tag{8.26}
$$

It can be inferred from Eq. (8.25) and (8.26) that there exists some analytical relationship between *Dw* and *h*. To study the function of *Dw* and *h*, 10 million Monte Carlo simulations of the stochastic field *f*(*x*) are carried out and then the values of *Dw* at some specified location (e.g., *x*=*L*/5 at Beam AB) and *h* for each simulation are obtained by Eq. (8.25) or (8.26) and Eq. (6.17) accordingly.

Figure 8.5 shows an example of 10 million (*h*, *Dw*) points at *x*=*L*/5 and *x*=*L*/2 by MCS. Although there exists some scatterness of the data points, an analytical function can be derived to describe the *Dw*-*h* relationship. As a reference, the red lines in Figure 8.5 are the quadratic curves given by MATLAB curve fitting function 'fit', which fitted the data very well with R^2=0.9989. However, it's not a good way to use library fitting functions directly without considering any physical meanings. One factor that has to be taken account when determining the *Dw*-*h* function is the curve must pass the point (h_m, 0), which means that the two structures are identical to each other when *h* equals to h_m. It's reasonable for that *h* equals h_m reflects a constant Young's modulus

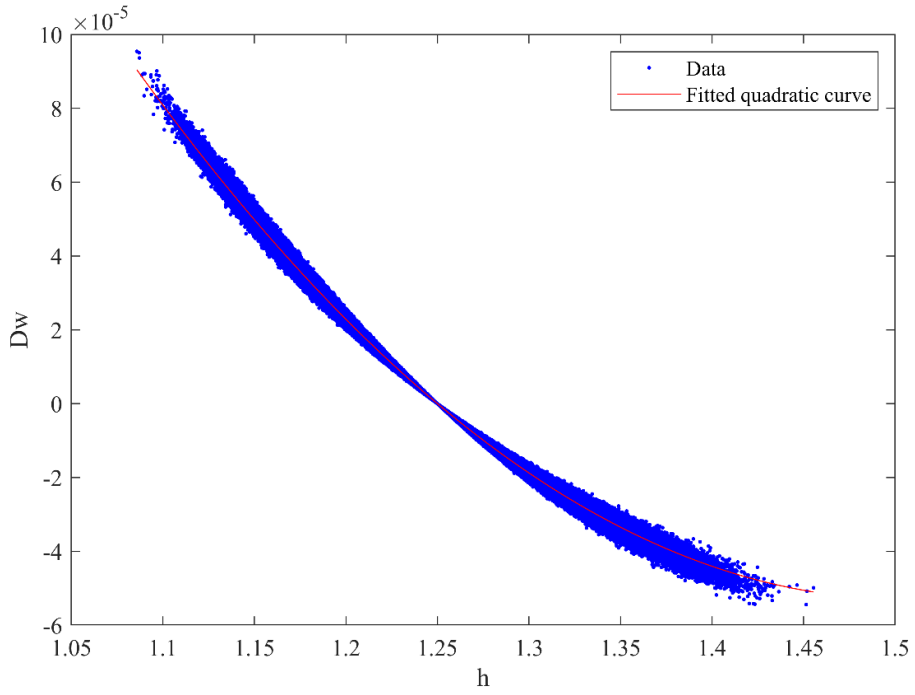

(a) $x=L/5$

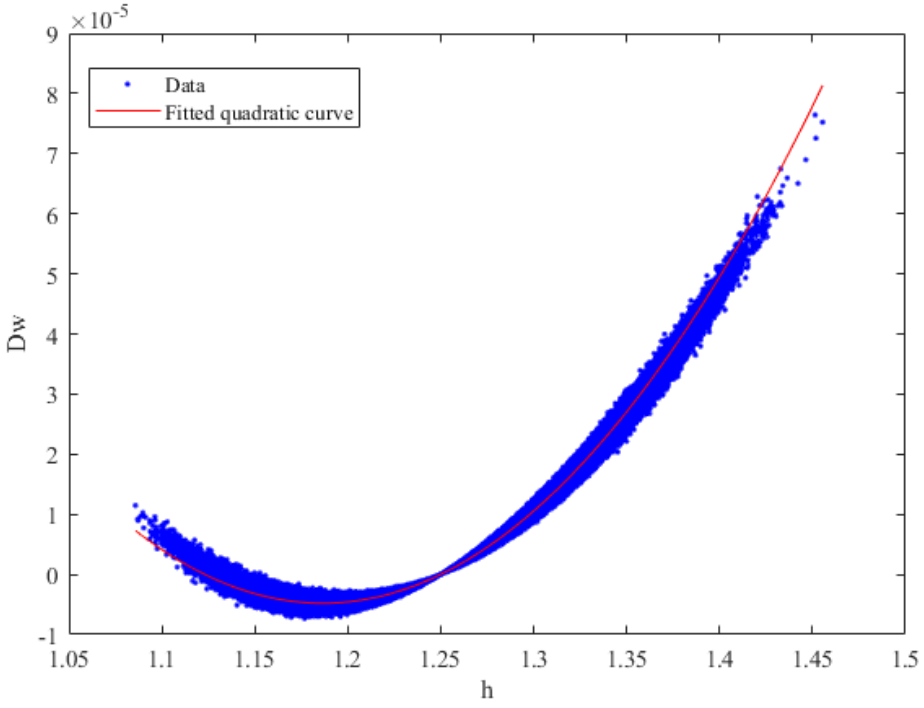

(b) $x=L/2$

Figure 8.5: 10 million MCS realizations of (h, Dw)

(i.e., $E(x)=E_0$) and there is no difference for the two structures in Figure 8.4 (a) and (b). To account for the effect, the part of $(-h+h_m)$ has to be extracted out.

Then, the expression for Dw_{AB} can be further simplified as

$$\begin{aligned} Dw_{AB} &= \frac{q_0}{2}\left(\int_0^x\int_0^{x_1}\frac{(x_2-h)(x_2-L)}{E(x_2)I}dx_2dx_1-\int_0^x\int_0^{x_1}\frac{(x_2-h_m)(x_2-L)}{E(x_2)I}dx_2dx_1\right) \\ &= \frac{q_0}{2}\left(\int_0^x dx_2\int_{x_2}^x\frac{(x_2-h)(x_2-L)}{E(x_2)I}dx_1-\int_0^x dx_2\int_{x_2}^x\frac{(x_2-h_m)(x_2-L)}{E(x_2)I}dx_1\right) \\ &= \frac{q_0}{2}\left(\int_0^x\frac{(x_2-h)(x_2-L)(x-x_2)}{E(x_2)I}dx_2-\int_0^x\frac{(x_2-h_m)(x_2-L)(x-x_2)}{E(x_2)I}dx_2\right) \\ &= \frac{q_0}{2}\int_0^x\frac{(x_2-L)(x-x_2)}{E(x_2)I}(-h+h_m)dx_2=\frac{q_0}{2E_0I}(-h+h_m)\int_0^x(x_2-L)(x-x_2)(1+f(x_2))dx_2 \end{aligned} \tag{8.27}$$

Similarly, by changing integration order, Dw_{BC} can be written as

$$Dw_{BC}=\frac{q_0}{2}\left[\int_0^x\frac{(x_2-L)(x-x_2)}{E(x_2)I}(-h+h_m)dx_2-\frac{x-h_m}{L-h_m}\int_0^L\frac{(x_2-h_m)(x_2-L)^2}{E(x_2)I}dx_2\right] \tag{8.28}$$

For the second part of Eq. (8.28), it can be divided into

$$\int_0^L\frac{(x_2-h_m)(x_2-L)^2}{E(x_2)I}dx_2=\int_0^L\frac{x_2(x_2-L)^2}{E(x_2)I}dx_2-\int_0^L\frac{h_m(x_2-L)^2}{E(x_2)I}dx_2 \tag{8.29}$$

Recall the Eq. (6.17) used to determine h in Section 6.2, then $\int_0^L\frac{x_2(x_2-L)^2}{E(x_2)I}dx_2$ can be replaced with $h\int_0^L\frac{(x_2-L)^2}{E(x_2)I}dx_2$ and Eq. (8.29) can be expressed as

$$\begin{aligned} \int_0^L\frac{(x_2-h_m)(x_2-L)^2}{E(x_2)I}dx_2 &= h\int_0^L\frac{(x_2-L)^2}{E(x_2)I}dx_2-\int_0^L\frac{h_m(x_2-L)^2}{E(x_2)I}dx_2 \\ &= (h-h_m)\int_0^L\frac{(x_2-L)^2}{E(x_2)I}dx_2 \end{aligned} \tag{8.30}$$

Substitute it into Dw_{BC},

$$Dw_{BC} = \frac{q_0}{2}\left[\int_0^x \frac{(x_2-L)(x-x_2)}{E(x_2)I}(-h+h_m)dx_2 - \frac{x-h_m}{L-h_m}(h-h_m)\int_0^L \frac{(x_2-L)^2}{E(x_2)I}dx_2\right]$$
$$= \frac{q_0}{2}(-h+h_m)\left[\int_0^x \frac{(x_2-L)(x-x_2)}{E(x_2)I}dx_2 + \frac{x-h_m}{L-h_m}\int_0^L \frac{(x_2-L)^2}{E(x_2)I}dx_2\right] \quad (8.31)$$
$$= \frac{q_0}{2E_0I}(-h+h_m)\left[\int_0^x (x_2-L)(x-x_2)(1+f(x_2))dx_2 + \frac{x-h_m}{L-h_m}\int_0^L (x_2-L)^2(1+f(x_2))dx_2\right]$$

Now Dw_{AB} and Dw_{BC} have the same analytical form of

$$Dw = \frac{q_0}{2E_0I}(-h+h_m)Z(x) \quad (8.32)$$

For Beam AB

$$Z(x,h) = \int_0^x (x_2-L)(x-x_2)(1+f(x_2))dx_2 \quad (8.33)$$

For Beam BC

$$Z(x,h) = \int_0^x (x_2-L)(x-x_2)(1+f(x_2))dx_2 + \frac{x-h_m}{L-h_m}\int_0^L (x_2-L)^2(1+f(x_2))dx_2 \quad (8.34)$$

Now the key is to find the relationship between Z(x,h) and h. Figure 8.6 is the 10 million simulations of h and Z at $x=L/5$ and $x=L/2$. And it's reasonable to assume that there is a linear function between Z and h, i.e.,

$$Z = \tilde{a}h + \tilde{b} \quad (8.35)$$

where $\tilde{a}$ and $\tilde{b}$ are parameters that can be determined easily by least square or any other numerical methods. Thus, *Dw-h* function becomes a quadratic function,

$$Dw = \frac{q_0}{2E_0I}(-h+h_m)(\tilde{a}h+\tilde{b}) = a_2h^2 + a_1h + a_0 \quad (8.36)$$

where a_2, a_1, a_0 are known numbers as $a_2 = \frac{q_0}{2E_0I}(-\tilde{a})$, $a_1 = \frac{q_0}{2E_0I}(\tilde{a}\cdot h_m - \tilde{b})$ and $a_0 = \frac{q_0}{2E_0I}\tilde{b}\cdot h_m$.

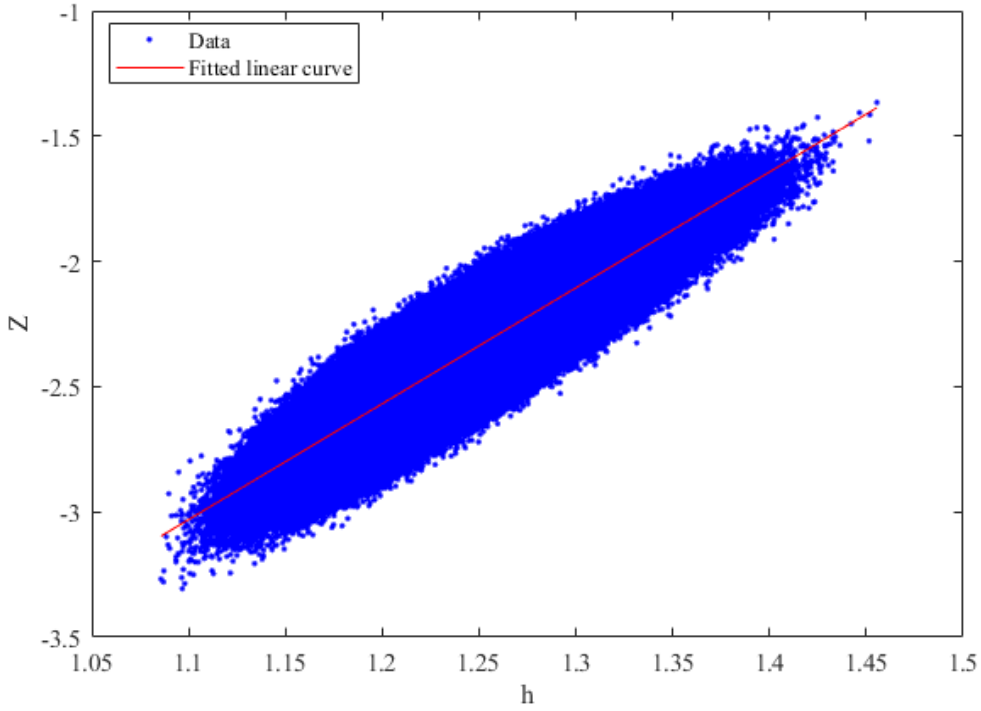

(a) $x=L/5$

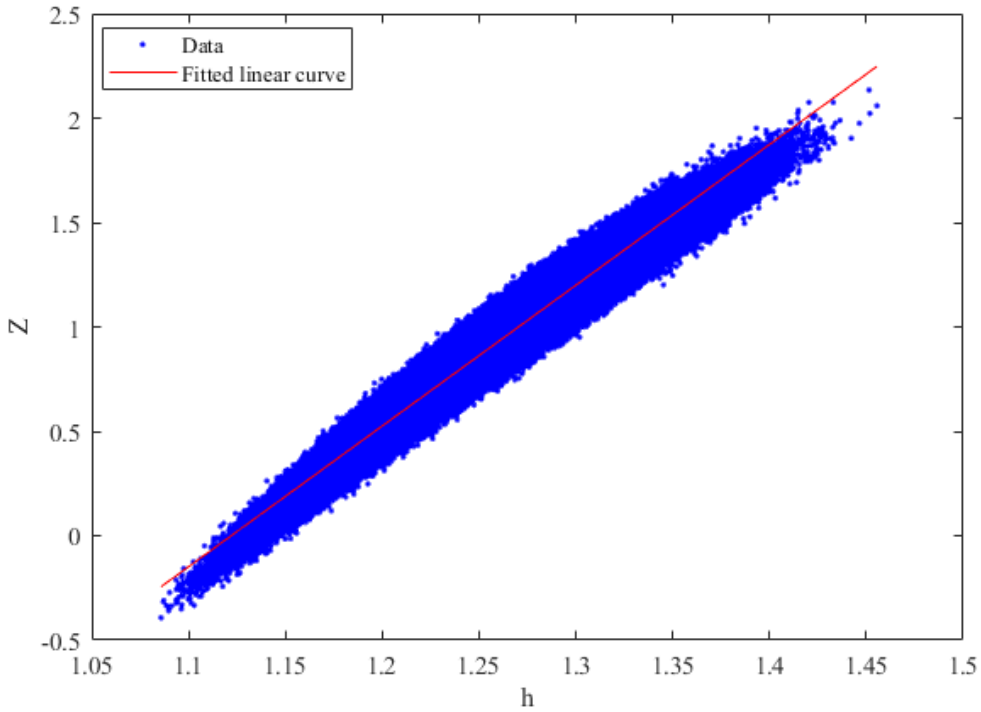

(b) $x=L/2$

Figure 8.6: 10 million MCS realizations of (*h*, *Z*)

Since the statistics of h are known from Eq. (6.17), the statistical properties of Dw can also be obtained by Eq. (8.36). Next, the corrected response variability of the statically indeterminate beam is derived combining w_m (from VRF) and Dw (from h).

8.4.3 Response variability of deflection after correction

From Eq. (8.36), the mean value and variance of Dw can be expressed using the statistics of h,

$$\varepsilon[Dw] = \varepsilon[a_2h^2 + a_1h + a_0] = a_2\varepsilon[h^2] + a_1\varepsilon[h] + a_0 \tag{8.37}$$

$$\begin{aligned} Var[Dw] &= Var[a_2h^2 + a_1h + a_0] \\ &= \varepsilon[(a_2h^2 + a_1h + a_0)^2] - (\varepsilon[Dw])^2 \\ &= \varepsilon[a_2^2h^4 + a_1^2h^2 + a_0^2 + 2a_2a_1h^3 + 2a_2a_0h^2 + 2a_1a_0h] - (\varepsilon[Dw])^2 \\ &= a_2^2\varepsilon[h^4] + 2a_2a_1\varepsilon[h^3] + (a_1^2 + 2a_2a_0)\varepsilon[h^2] + 2a_1a_0\varepsilon[h] + a_0^2 - (\varepsilon[Dw])^2 \end{aligned} \tag{8.38}$$

The only part left to get the corrected response variability in Eq. (8.23) and Eq. (8.24) is the covariance of Dw and w_m. It can be calculated as

$$\mathrm{COV}[w_m, Dw] = \mathrm{COV}[w_m, a_2h^2 + a_1h + a_0] = a_2\mathrm{COV}[w_m, h^2] + a_1\mathrm{COV}[w_m, h] \tag{8.39}$$

By applying the definition of w_m for Beam AB and BC with h=h_m, $\mathrm{COV}[w_m, h^2]$ and $\mathrm{COV}[w_m, h]$ are computed as the following.

- *Beam AB*

$$\begin{aligned} COV[w_m, h] &= \varepsilon[w_m h] - \varepsilon[w_m]\varepsilon[h] \\ &= \varepsilon\left[\frac{q_0}{2}\int_0^x\int_0^{x_1}\frac{(x_2 - h_m)(x_2 - L)}{E(x_2)I}dx_2dx_1 \cdot h\right] - \varepsilon[w_m]\varepsilon[h] \\ &= \frac{q_0}{2E_0I}\int_0^x (x_2 - h_m)(x_2 - L)(x - x_2)\varepsilon\left[h(1 + f(x_2))\right]dx_2 - \varepsilon[w_m]\varepsilon[h] \end{aligned} \tag{8.40}$$

where $\varepsilon[w_m]$ and $\varepsilon[h]$ are known, and $\varepsilon\left[h(1 + f(x_2))\right] = \varepsilon[h] + \varepsilon[hf(x_2)]$ can be obtained during the process of generating h samples by Eq. (6.17). For each simulation, a series of $f(x)$, with x

ranging from 0 to L, is generated as well as one h sample and one $hf(x)$ sample. Finally, the expectation of $\varepsilon[hf(x)]$ at all possible x along the beam is obtained.

Similarly,

$$\begin{aligned} COV[w_m, h^2] &= \varepsilon[w_m h^2] - \varepsilon[w_m]\varepsilon[h^2] \\ &= \varepsilon\left[\frac{q_0}{2}\int_0^x\int_0^{x_1}\frac{(x_2-h_m)(x_2-L)}{E(x_2)I}dx_2dx_1\cdot h^2\right] - \varepsilon[w_m]\varepsilon[h^2] \\ &= \frac{q_0}{2E_0I}\int_0^x (x_2-h_m)(x_2-L)(x-x_2)\varepsilon\left[h^2(1+f(x_2))\right]dx_2 - \varepsilon[w_m]\varepsilon[h^2] \end{aligned} \tag{8.41}$$

where $\varepsilon\left[h^2(1+f(x_2))\right] = \varepsilon[h^2] + \varepsilon[h^2 f(x_2)]$ can also be computed by the same process described above.

- *Beam BC*

$$\begin{aligned} COV[w_m, h] &= \varepsilon[w_m h] - \varepsilon[w_m]\varepsilon[h] \\ &= \frac{q_0}{2}\varepsilon\left\{\left[\int_0^x\int_0^{x_1}\frac{(x_2-h_m)(x_2-L)}{E(x_2)I}dx_2dx_1 - \frac{x-h_m}{L-h_m}\int_0^L\int_0^{x_1}\frac{(x_2-h_m)(x_2-L)}{E(x_2)I}dx_2dx_1\right]\cdot h\right\} - \varepsilon[w_m]\varepsilon[h] \\ &= \frac{q_0}{2E_0I}\left[\begin{array}{l}\displaystyle\int_0^x (x_2-h_m)(x_2-L)(x-x_2)\varepsilon\left[h(1+f(x_2))\right]dx_2 \\ \displaystyle+\frac{x-h_m}{L-h_m}\int_0^L (x_2-h_m)(x_2-L)^2\varepsilon\left[h(1+f(x_2))\right]dx_2\end{array}\right] - \varepsilon[w_m]\varepsilon[h] \end{aligned} \tag{8.42}$$

Also,

$$\begin{aligned} COV[w_m, h^2] &= \varepsilon[w_m h^2] - \varepsilon[w_m]\varepsilon[h^2] \\ &= \varepsilon\left\{\left[\frac{q_0}{2}\int_0^x\int_0^{x_1}\frac{(x_2-h_m)(x_2-L)}{E(x_2)I}dx_2dx_1 - \frac{x-h_m}{L-h_m}\int_0^L\int_0^{x_1}\frac{(x_2-h_m)(x_2-L)}{E(x_2)I}dx_2dx_1\right]\cdot h^2\right\} - \varepsilon[w_m]\varepsilon[h^2] \\ &= \frac{q_0}{2E_0I}\left[\begin{array}{l}\displaystyle\int_0^x (x_2-h_m)(x_2-L)(x-x_2)\varepsilon\left[h^2(1+f(x_2))\right]dx_2 \\ \displaystyle+\frac{x-h_m}{L-h_m}\int_0^L (x_2-h_m)(x_2-L)^2\varepsilon\left[h^2(1+f(x_2))\right]dx_2\end{array}\right] - \varepsilon[w_m]\varepsilon[h^2] \end{aligned} \tag{8.43}$$

In summary, the basic steps of the proposed approach to estimate the response variability of statically indeterminate beams are:

1. Use spectral representation method [35] to generate a large number of samples of the stochastic field $f(x)$ modeling the inverse of Young's modulus (Eq.(6.2)).
2. Locate the zero-moment point of the statically indeterminate structure, denoted as $x=h$. Generate h samples analytically (Eq. (6.17)) or by SFEM based on $f(x)$ samples.
3. Add a hinge at the zero-moment point, transforming the original statically indeterminate structure to its equivalent statically determinate structure.
4. Solve the governing equation of the statically determinate structure, with deflection or any other types of responses expressed by the stochastic field $f(x)$ and h (Eq. (8.3) and (8.13)).
5. Derive the VRF of the statically determinate structure at some deterministic value $h=h_0$ (Eq. (8.8)-(8.9) or Eq. (8.17)-(8.18)), as well as the corresponding response variability (Eq. (8.4) and (8.10) or Eq. (8.14) and (8.19)).
6. Use $\mathrm{VRF}_{h\mathrm{m}}$, i.e., use $h_m=L/4$ to calculate the VRF derived above, to represent the average VRF when estimating response variability $Var[w_m]$ (Eq. (8.21)).
7. Introduce correction term Dw defined by Eq. (8.22). Develop the function between Dw and h, e.g., a quadratic function is applied in this dissertation, with the curve passing the fixed point (h_m, 0) (Eq. (8.36)).
8. Calculate $\varepsilon[Dw]$, $\mathrm{Var}[Dw]$ and $\mathrm{COV}[w_m, Dw]$ (Eq.(8.37)-(8.43)) based on the Dw-h function developed.

Finally, the corrected response variability can be obtained by Eq. (8.23)-(8.24).

8.5 Numerical Example

Consider the statically indeterminate beam in Figure 6.1(a), with the same parameters as in the numerical example of Chapter 7. For illustration, there are two locations selected for analysis, i.e.,

$x = L/5 = 1$ m at Beam AB and $x = L/2 = 2.5$ m at Beam BC. The Variability Response Functions at both locations with $h_m = L/4 = 1.25$ m are calculated by Eq. (8.8)-(8.9) and Eq. (8.17)-(8.18), which are shown in Figure 8.1. To compute the response variability, the spectral density function of $f(x)$ is defined in Eq. (6.18) with $\sigma_{ff} = 0.1$ and $b=1$. By applying it together with the VRFs into Eq.(8.21), the variance of $w_1(x=1) = w_m(x=1)$ and $w_2(x=2.5) = w_m(x=2.5)$ can be obtained. Table 8.1 summarizes the estimated response variability (expectation, variance and coefficient of variation) at $x=1$ m and $x=2.5$ m from VRF and direct MCS. It indicates that VRF estimates have reasonable accuracy towards the true response variability (i.e., MCS results) but there still exists some difference from the MCS results especially in variance estimation.

Table 8.1: Comparison of the estimated response variability at $x=1$ m and $x=2.5$ m by VRF, its correction and 10 million MCS

		By VRF	After correction	10 million MCS
$x=1$ m	Mean value	-3.8519E-04	-3.8445E-04	-3.8445E-04
	Variance	1.1068E-09	4.1567E-10	4.0986E-10
	COV	0.0828	0.0530	0.0527
$x=2.5$ m	Mean value	-0.01157	-0.01157	-0.01156
	Variance	1.5464E-09	1.6940E-09	1.6790E-09
	COV	0.0340	0.0356	0.0355

To further address the problem, correction term Dw is used following the steps described in Section 8.4.3. Figure 8.7 is the histogram of 10 million h samples generated by Eq. (6.17), from which the statistics of h can be obtained. The corresponding 10 million pairs of (h, Dw) and (h, Z) points at $x=1$ m and $x=2.5$ m are shown in Figure 8.5 and Figure 8.6. It's assumed that there is a linear function between h and Z and it can be obtained numerically (the red lines in Figure 8.6).

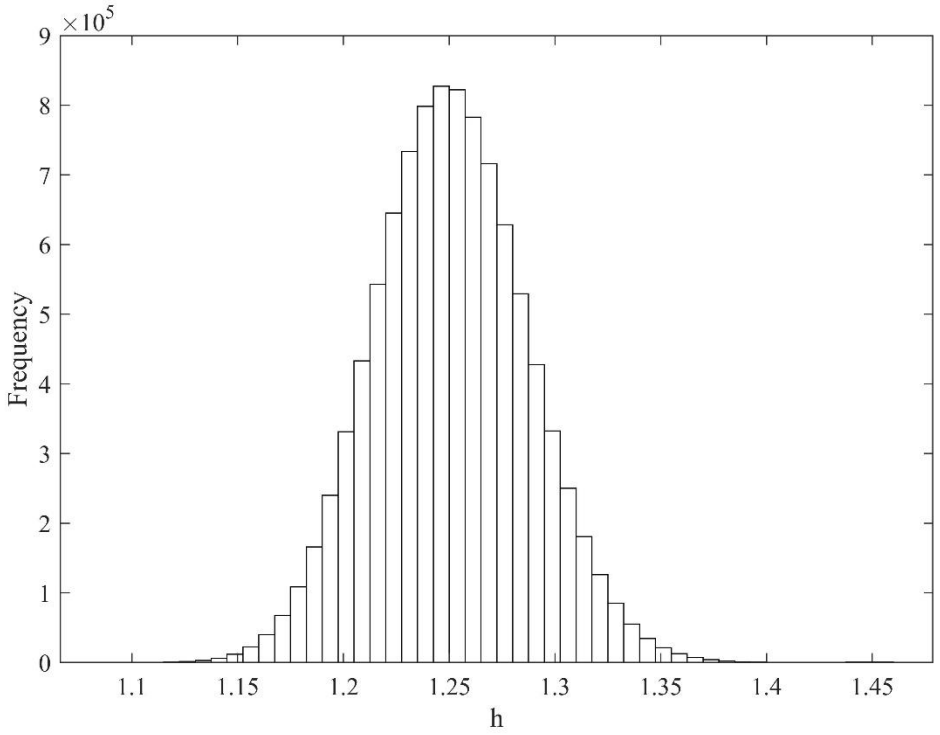

Figure 8.7: Histogram of 10 million samples of *h* generated by Eq. (6.17)

Then, the quadratic function between *Dw* and *h* in Eq. (8.36) can be determined. Incorporating the function and following Eq. (8.23)-(8.24), the corrected response variability is computed. Table 8.1 also includes the results of estimated mean value, variance and coefficient of variation of deflection at x=1 m and x=2.5 m after correction. And the corrected response variability coincides very well with the results by MCS, which proves the effectiveness of the correction term *Dw*.

Summary

To quantify the response variability of statically indeterminate structures, two novel Variability Response Function-based integral expressions for the variances of the bending moment and deflection, of statically indeterminate beams with stiffness modeled by a random field have been

formulated in Part II. By solving the governing equations of the statically indeterminate structure, the response bending moment along the length of the beam $M(x)$, and deflection $w(x)$ are expressed as a function of its (random) zero-moment location h.

For bending moment, the function $M(x)$, combined with Taylor series expansion of the random zero-moment location, leads to novel Variability Response Function-based integral expressions for the variance of the response bending moment, $Var[M(x)]$. In general, the proposed second-order Taylor series-based formulation is expected to provide more accurate results. Extensive numerical examples are provided where the accuracy of the results obtained using the proposed formulation is validated using Monte Carlo simulations involving stochastic fields that follow truncated Gaussian and shifted lognormal probability distribution functions. These Monte Carlo simulation results indicate that the proposed Variability Response Functions are probability-distribution-independent.

For deflection $w(x)$, an approximate close-form analytical Variability Response Function is built based on the transformed statically determinate structure with all possible hinge locations. And an ensemble average is taken to get the overall Variability Response Function of the system, which can be replaced by the Variability Response Function with the hinge located at the same zero-moment point with the deterministic system without any randomness. To get more accurate estimates of the original statically indeterminate system, the estimates from Variability Response Function can be further revised by introducing a correction term Dw. The relationship between Dw and h can be found numerically based on the samples generated from the stochastic field. Finally, incorporating the Dw-h function as well as the estimates from Variability Response Function into the correction function, the corrected response variability of the original statically indeterminate structure can be obtained with perfect accuracy.

Chapter 9 : Conclusions

In this dissertation, two important topics have been addressed in the field of uncertainty quantification in civil infrastructure systems: 1) quantify the uncertainties/randomness in material properties by stochastic field model; 2) estimate the response variability of civil structures caused by the randomness in material/loading properties. The main contributions of the work in the two aspects are presented below and future works are also included then.

9.1 Main contributions

9.1.1 Part I

For Part I, a novel methodology is proposed to evaluate the ultimate strength of the main cables of suspension bridges using information obtained from site inspections and from tensile strength tests on selected wire samples extracted from the bridge's main cables.

First of all, spatial variability of the strength of corroded wires is modeled for the first time when evaluating cable strength. To fully account for the spatial variation of strength along a wire's length, the methodology uses the mapping of the corrosion stage variation of all wires exposed through wedging, along the length of the entire panel. This mapping is not adding any cost to the current standard inspection process. Then, probability distribution functions for the ultimate tensile strength of 18" long wire segments in each corrosion stage group are established, and random realizations of the ultimate strength of all the wires in the cable's cross section can be generated conveniently by the corrosion maps and probability distributions. Second, redevelopment of broken wires in adjacent panels is considered through a reduction in the evaluation panel of the original simulated strengths of wires. Monte Carlo simulations then generate a large number of

overall cable strength realizations and the final outcome is the probability distribution of the main cable under evaluation. Any probabilistic characteristics (e.g., mean, variance, confidence interval etc.) can be extracted from the histogram or PDF/CDF developed, which gives more detailed information as well as insights into the condition of the bridge, assisting engineers in more robust risk-based decision-making.

9.1.2 Part II

In Part II, analytical close-form of Variability Response Functions for statically indeterminate structures are formulated for the first time on the variances of the response bending moment as well as the response displacement/deflection.

For bending moment, novel Variability Response Function-based integral expressions for the variance of the response bending moment, $Var[M(x)]$, of statically indeterminate beams with stiffness modeled by a random field have been formulated in Chapter 7. This is the first time that such expressions are established using a second-order Taylor series expansion and an approach based on the zero bending moment location along the length of the beam. The proposed expressions are fundamentally different from all currently existing expressions that are based inherently on first-order Taylor series expansions, as they involve: (i) two distinct integrals in the expression for $Var[M(x)]$ and, (ii) an expression for $\varepsilon[M(x)]$ that depends on stochastic field $f(x)$. In all currently existing formulations, there is a single integral in the expression for $Var[M(x)]$ and the expression for $\varepsilon[M(x)]$ is independent of stochastic field $f(x)$. It also resolves the long-standing issue of whether the single-term, VRF-based integral form for the response variance of statically determinate structures (Eq. (6.1)) can be conjectured to exist also for statically indeterminate structures. The answer is negative as the proposed formulation involves an

expression with two integrals. The accuracy of the results obtained using the proposed formulation is validated using Monte Carlo simulations, which indicates that the proposed Variability Response Functions are probability-distribution-independent.

For deflection $w(x)$ of the statically indeterminate beams, an approximate Variability Response Function has been formulated in Chapter 8. By adding hinges at the zero-moment locations of the system, the original statically indeterminate structure can be transformed into its equivalent statically determinate structure, with the zero-moment location h as a random variable. Then, the VRF of the statically determinate structure can be derived at different h samples generated by the realizations of stochastic field $f(x)$. An ensemble average is taken for all the VRFs obtained with h samples as the overall VRF of the structure. It's found that the average VRF has very insignificant difference from the VRF obtained at $h=h_m$, where h_m is the zero-moment location of the statically indeterminate beam with constant material property. It dramatically reduces the computational effort compared with direct Monte Carlo simulation or stochastic finite element analysis, especially using the substitution of average VRF with VRF at h_m. Then, the estimates of the developed VRF are further improved by the introduction of the correction term Dw, with almost perfect accuracy.

9.2 Future work

Uncertainty quantification for civil infrastructure systems is a very significant topic. It's directly related to structures safety and risk assessment. This dissertation just covers a very small part of researches and some progress in the field, and extensive works are expected in the future, which may include:

- *Higher-level study of suspension bridge cable strength estimation with the consideration of spatial variability.*

  One way is to use more complex mathematical models with higher accuracy, for example, a 3D random field [78], to depict the spatial variation of wire strength within the suspension cables. However, the resulting methodology would be applicable in practice without the need to understand the underlying complex mathematical theory.

  Second, finite element models can be introduced to evaluate the overall strength of the cable under some loading conditions, instead of the simplified loading process used in this dissertation. The contact model between the wires should be developed, together with the stochastic field model along the wires, and eventually ensembled and put to FEM analysis.

- *Extensive work in VRF and stochastic fields modeling*

  Extending the derived VRFs to more complex statically indeterminate structures like 2D frames or plates is one of the interesting applications that the author wants to explore. For complex structures, advanced analysis tools like Stochastic Finite Element (SFEM) would be applied to determine the locations of zero-moment or hinges and obtain the probabilistic characteristics.

  Improvements in the proposed methodology in Chapter 8 could be the correction term *Dw* and its relationship with *h*. In the dissertation, *Dw*-*h* relationship is developed thorough a semi-analysis and semi-simulation way, which can be replaced by more alternatives. Mainly, there are two ways to extend research along the line: (1) using machine learning methods to determine the *Dw*-*h* relationship, which makes it a learning process without any predetermined assumptions; (2) deriving the true *Dw*-*h* relationship by the physical meaning of the two and incorporating it into the VRF.

Finally, all VRFs presented in this dissertation are validated and applied to Gaussian or Gaussian-translated stochastic fields, and stationary in time. It's of great importance to extend the VRFs for statically indeterminate structures to more complex conditions, where non-Gaussian, non-stationary stochastic processes are involved like earthquakes.

References

[1] Steinman, Boynton, Gronquist, and Birdsall. “Williamsburg bridge cable investigation program: Final report” *Submitted to the New York State Department of Transportation and New York City Department of Transportation*, New York, N.Y, 1988.

[2] J. Matteo, G. Deodatis, and D. P. Billington. “Safety analysis of suspension-bridge cables: Williamsburg bridge.” *Journal of Structural Engineering*, 120(11), pp. 3197-3211, Nov. 1994.

[3] R. Q. Haight, D. P. Billington and D. Khazem. “Cable safety factors for four suspension bridge.” *Journal of Bridge Engineering*, 2(4), pp. 157-167, Nov. 1997.

[4] K. M. Mahmoud. “BTC method for evaluation of remaining strength and service life of bridge cables.” *NYSDOT REPORT C-07-11 FINAL REPORT*. New York (State). Dept. of Transportation, Sep. 2011.

[5] R. Nickerson. “Safety appraisal of suspension bridge main cables.” *Contractor's Report from a Workshop in Neward*, New Jersey, No. NCHRP Project 20-07, Nov. 1998.

[6] P. Sluszka, C. Gagnon and S. Rankin. “Inspection, evaluation, and monitoring of suspension bridge cables.” *In Structures Congress 2006: Structural Engineering and Public Safety*, pp. 1-9, 2006.

[7] I.C. Noyan, A. Brügger, R. Betti and B. Clausen. “Measurement of strain/load transfer in parallel seven-wire strands with neutron diffraction.” *Experimental Mechanics*, 50(2), pp. 265-272, Feb. 2010.

[8] M. J D. Sloane, R. Betti, G. Marconi, A. L. Hong and D. Khazem. “Experimental analysis of a nondestructive corrosion monitoring system for main cables of suspension bridges.” *Journal of Bridge Engineering*, 18(7), pp. 653-662, 2012.

[9] R. Betti, D. A. Khazem, M. Carlos, R. Gostautas and Y. P. Virmani. “Corrosion monitoring research for city of New York bridges.” *United States. Federal Highway Administration*. Office of Infrastructure Research and Development, May 2014.

[10] S. Park, J. W. Kim and D. J. Moon. “Non-contact main cable NDE Technique for suspension bridge using magnetic flux-based BH Loop measurements.” *Structural Health Monitoring and Inspection of Advanced Materials, Aerospace, and Civil Infrastructure*, Vol. 9437, pp. 136-144, Apr. 2015.

[11] R. M. Mayrbaurl and S. Camo. “Guidelines for inspection and strength evaluation of suspension bridge parallel wire cables.” *Transportation Research Board,* NCHRP Report 534, 2004.

[12] US Federal Highway Administration. *Primer for the inspection and strength evaluation of suspension bridge cables*. Government Printing Office, 2012.

[13] Y. Shi, G. Deodatis and R. Betti. "Random field-based approach for strength evaluation of suspension bridge cables." *Journal of Structural Engineering*, 133(12), pp. 1690-1699, Dec. 2007.

[14] S.C. Barton, G.W. Vermaas, P.F. Duby, A.C. West and R. Betti. "Accelerated corrosion and embrittlement of high-strength bridge wire." *Journal of materials in civil engineering*, 12(1), pp. 33-38, Feb. 2000.

[15] K. Furuya, M. Kitagawa, S.I. Nakamura and K. Suzumura. "Corrosion mechanism and protection methods for suspension bridge cables." *Structural engineering international*, 10(3), pp. 189-193, Aug. 2000.

[16] S. Li, Y. Xu, S. Zhu, X. Guan and Y. Bao. "Probabilistic deterioration model of high-strength steel wires and its application to bridge cables." *Structure and Infrastructure Engineering*, 11(9), pp. 1240-1249, Sep. 2015.

[17] E. Karanci and R. Betti. "Modeling corrosion in suspension bridge main cables. I: annual corrosion rate." *Journal of Bridge Engineering*, 23(6), p. 04018025, Jun. 2018.

[18] E. Karanci and R. Betti. "Modeling corrosion in suspension bridge main cables. II: Long-term corrosion and remaining strength." *Journal of Bridge Engineering*. 23(6), p. 04018026, Jun. 2018.

[19] T. Hopwood and J. H. Havens. "Corrosion of cable suspension bridges." *Kentucky Transportation Research Program*, University of Kentucky Lexington, 1984.

[20] Modjeski and Masters, Inc. "The Mid-Hudson Bridge 2009 cable strength evaluation." *Technical Report Prepared for the New York State Bridge Authority*, New York, 2011.

[21] Z. P. Bažant. "Design of quasibrittle materials and structures to optimize strength and scaling at probability tail: an apercu." *Proceedings. Mathematical, physical, and engineering science*, 475(2224), p. 20180617, Apr. 2019.

[22] S. Camo. "Probabilistic strength estimates and reliability of damaged parallel wire cables." *Journal of Bridge Engineering*, 8(5), pp. 297-311, Sep. 2003.

[23] C. Cremona. "Probabilistic approach for cable residual strength assessment." *Engineering Structures*, 25(3), pp. 377-384.

[24] Perry R. J. (1998). "Estimating strength of the Williamsburg bridge suspension cables." *The American Statistician*, 52(3), pp. 211-217, Feb. 2003.

[25] G. Fu, F. Moses and D. A. Khazem. “Strength of parallel wire cables for suspension bridges.” *8th ASCE Specialty Conference on Probabilistic Mechanics and Structural Reliability*. University of Notre Dame, Notre Dame, Indiana: American Society of Civil Engineers, Jul. 2000.

[26] L Devroye. *Non-Uniform Random Variate Generation*. New York: Springer-Verlag, 1986

[27] A. Montoya, H. Waisman and R. Betti. “A simplified contact-friction methodology for modeling wire breaks in parallel wire strands.” *Computers & Structures*, 100, pp. 39-53, Jun. 2012.

[28] A. Montoya, G. Deodatis, R. Betti and H. Waisman. “Physics-based stochastic model to determine the failure load of suspension bridge main cables*.” Journal of Computing in Civil Engineering*, 29(4), p. B4014002, Jul. 2015.

[29] H. Waisman, A. Montoya, R. Betti and I. C. Noyan. “Load transfer and recovery length in parallel wires of suspension bridge cables.” *Journal of Engineering Mechanics*, 137(4), pp. 227-237, Apr. 2011.

[30] Modjeski and Masters, Inc. “The Bear Mountain Bridge 2018 cable strength evaluation,” *Technical Report Prepared for the New York State Bridge Authority*, New York, 2021.

[31] M. Shinozuka “Probabilistic modeling of concrete structures.” *Journal of the Engineering Mechanics Division*, 98(6), pp. 1433-1451, Dec. 1972.

[32] M. Shinozuka, E. Lenoe. “A probabilistic model for spatial distribution of material properties.” *Engineering Fracture Mechanics*, 8(1), pp. 217-227, Jan. 1976.

[33] K. Handa. “Application of finite element methods in the statistical analysis of structures.” *In Proc. 3rd Int. Conf. on Structural Safety and Reliability*, Sydney, pp. 409-417, 1981.

[34] M. Shinozuka, C.M. Jan. “Digital simulation of random processes and its applications.” *Journal of Sound and Vibration*.” 25(1), pp. 111-128, Nov. 1972.

[35] M. Shinozuka and G. Deodatis. “Simulation of stochastic processes by spectral representation.” *Applied Mechanics Reviews*, 44(4), 1991.

[36] W. Gersch and J. Yonemoto. “Synthesis of multivariate random vibration systems: a two-stage least squares AR-MA model approach.” *Journal of Sound and Vibration*, 52(4), pp. 553-565, Jun. 1977.

[37] P. Spanos and J. E. Hansen. “Linear prediction theory for digital simulation of sea waves.” *Journal of Energy Resources Technology*, 103(3), pp. 243-249, Sep. 1981.

[38] P. Spanos. “ARMA algorithms for ocean wave modeling.” *Journal of Energy Resources Technology*, 300-309, 1983.

[39] E. Samaras, M. Shinzuka and A. Tsurui. “ARMA representation of random processes.” *Journal of Engineering Mechanics*, 111(3), pp. 449-461, Mar. 1985.

[40] Kari Karhunen. “Über lineare Methoden in der Wahrscheinlichkeitsrechnung.” *Ann. Acad. Sci. Fennicae*, 37: 1–79, 1947.

[41] M. Loève. *Probability theory*. Vol. II, 4th ed. Graduate Texts in Mathematics. Vol. 46. Springer-Verlag. 1978.

[42] R.G. Ghanem and P. Spanos. *Stochastic finite elements: a spectral approach*. Courier Corporation, 2003.

[43] M. Grigoriu. *Applied non-gaussian processes: Examples, theory, simulation, linear random vibration, and MATLAB solutions*. Englewood Cliffs, NJ: Prentice Hall, Inc, 1995.

[44] F. Yamazaki and M. Shinozuka. “Digital generation of non-Gaussian stochastic fields.” *Journal of Engineering Mechanics*, 114(7), pp. 1183-1197, Jul. 1988.

[45] G. Deodatis and R.C. Micaletti. “Simulation of highly skewed non-Gaussian stochastic processes.” *Journal of Engineering Mechanics*, 127(12), pp. 1284-1295, Dec. 2001.

[46] P. Bocchini and G. Deodatis. “Critical review and latest developments of a class of simulation algorithms for strongly non-Gaussian random fields.” *Probabilistic Engineering Mechanics*. 23(4), pp. 393-407, Oct. 2008.

[47] M.D. Shields, G. Deodatis and P. Bocchini. “A simple and efficient methodology to approximate a general non-Gaussian stationary stochastic process by a translation process.” *Probabilistic Engineering Mechanics*, 26(4), pp. 511-519, Oct. 2011.

[48] M.D. Shields, G. Deodatis. “A simple and efficient methodology to approximate a general non-Gaussian stationary stochastic vector process by a translation process with applications in wind velocity simulation.” *Probabilistic Engineering Mechanics*, 31, pp. 19-29, Jan. 2013.

[49] I. Elishakoff and Y. Ren. *Finite element methods for structures with large stochastic variations*. Vol. 7. Oxford University Press on Demand, 2003.

[50] A. Haldar and M. Sankaran. *Reliability assessment using stochastic finite element analysis*. John Wiley & Sons, 2000.

[51] C. Bucher. *Computational analysis of randomness in structural mechanics: structures and infrastructures book series*. Vol. 3. Crc Press, 2009.

[52] M. Shinozuka. “Structural response variability.” *Journal of Engineering Mechanics*, 113(6), pp. 825-842, Jun. 1987.

[53] C. Bucher and M. Shinozuka. “Structural response variability II.” *Journal of Engineering Mechanics*, 114(12), pp. 2035-2054, Dec. 1988.

[54] A. Kardara, C. Bucher and M. Shinozuka. “Structural response variability III.” *Journal of Engineering Mechanics*, 115(8), pp. 1726-1747, Aug. 1989.

[55] G. Deodatis and M. Shinozuka. “Bounds on response variability of stochastic systems.” *Journal of Engineering Mechanics*, 115(11), pp. 2543-2563, Nov. 1989.

[56] G. Deodatis, L. Graham-Brady and R. Micaletti. “A hierarchy of upper bounds on the response of stochastic systems with large variation of their properties: random variable case.” *Probabilistic Engineering Mechanics*, 18(4), pp. 349-363, Oct. 2003.

[57] G. Deodatis, L. Graham-Brady and R. Micaletti. “A hierarchy of upper bounds on the response of stochastic systems with large variation of their properties: random field case.” *Probabilistic Engineering Mechanics*, 18(4), pp. 365-375, Oct. 2003.

[58] G. Deodatis. “Bounds on response variability of stochastic finite element systems.” *Journal of Engineering Mechanics*. 116(3), pp. 565-585, Mar. 1990.

[59] G. Deodatis. “Bounds on response variability of stochastic finite element systems: effect of statistical dependence.” *Probabilistic Engineering Mechanics*, 5(2), pp. 88-98, Jun. 1990.

[60] G. Deodatis. “Weighted integral method. I: stochastic stiffness matrix.” *Journal of Engineering Mechanics*, 117(8), pp. 1851-1864, Aug. 1991.

[61] G. Deodatis and M. Shinozuka. “Weighted integral method. II: response variability and reliability.” *Journal of Engineering Mechanics*, 117(8), pp. 1865-1877, Aug. 1991.

[62] F.J. Wall and G. Deodatis. “Variability response functions of stochastic plane stress/strain problems.” *Journal of Engineering Mechanics*, 120(9), pp. 1963-1982, Sep 1994.

[63] L. Graham-Brady and G Deodatis. “Variability response functions for stochastic plate bending problems.” *Structural Safety*. 20(2), pp. 167-188, Jan. 1998.

[64] S.R. Arwade, G. Deodatis and K. Teferra. “Variability response functions for apparent material properties.” *Probabilistic Engineering Mechanics*, 44, pp. 28-34, Apr 2016.

[65] V. Papadopoulos, G. Deodatis and M. Papadrakakis. “Flexibility-based upper bounds on the response variability of simple beams.” *Computer Methods in Applied Mechanics and Engineering*, 194(12-16), pp. 1385-1404, Apr. 2005.

[66] V. Papadopoulos and G. Deodatis. “Response variability of stochastic frame structures using evolutionary field theory.” *Computer Methods in Applied Mechanics and Engineering*, 195(9-12), pp. 1050-1074, Feb. 2006.

[67] V. Papadopoulos, M. Papadrakakis and G. Deodatis. “Analysis of mean and mean square response of general linear stochastic finite element systems.” *Computer Methods in Applied Mechanics and Engineering*, 195(41-43), pp. 5454-5471, Aug. 2006.

[68] G. Deodatis, L. Graham-Brady and R. Micaletti. “Upper bounds on the response variance of stochastic systems via generalized variability response functions.” *In Computational Fluid and Solid Mechanics 2003*, pp. 1918-1921, Elsevier Science Ltd, 2003.

[69] M. Miranda. *On the response variability of beam structures with stochastic variations of parameters*. Columbia University; 2009.

[70] M. Miranda and G. Deodatis. “Generalized variability response functions for beam structures with stochastic parameters.” *Journal of Engineering Mechanics*, 138(9), pp. 1165-1185, Sep. 2012.

[71] K. Teferra. *Developments in the theory and applications of the variability response function concept.* Columbia University, 2012.

[72] K. Teferra, S.R. Arwade and G. Deodatis. “Stochastic variability of effective properties via the generalized variability response function.” *Computers & Structures*. 110, pp. 107-115, Nov. 2012.

[73] K. Teferra and G. Deodatis. “Variability response functions for beams with nonlinear constitutive laws.” *Probabilistic Engineering Mechanics*, 29, pp. 139-148, Jul. 2012.

[74] K. Teferra, S.R. Arwade and G. Deodatis. “Generalized variability response functions for two-dimensional elasticity problems.” *Computer Methods in Applied Mechanics and Engineering*, 272, pp. 121-137, Apr. 2014.

[75] N. Wiener. “Generalized harmonic analysis.” *Acta mathematica*. 55(1), pp. 117-258, Dec. 1930.

[76] A. Khintchine. “Korrelationstheorie der stationären stochastischen Prozesse.” *Mathematische Annalen*, 109(1), pp. 604-615, Dec. 1934.

[77] A. Papoulis. *Probability, random variables, and stochastic processes*. WCB/McGraw-Hill, 3rd edition, 1991.

[78] M. Shinozuka and G. Deodatis. “Simulation of multi-dimensional Gaussian stochastic fields by spectral representation.” *Applied Mechanics Reviews*, 49(1), pp. 29-53, Jan. 1996.

Appendix A

Table A.1: Summary of C_i Constants

Parameter	Expression	Simplified
α	$\alpha = \varepsilon[Y] = \int_0^L (x-L)^2 dx$	/
β	$\beta = \varepsilon[X] = \int_0^L x(x-L)^2 dx$	/
C_1	$C_1 = \int_0^L \int_0^L x_1(x_1-L)^2(x_2-L)^2 dx_1 dx_2$	$\alpha\beta$
C_2	$C_2 = \int_0^L \int_0^L x_1(x_1-L)^2 x_2(x_2-L)^2 dx_1 dx_2$	β^2
C_3	$C_3 = \int_0^L \int_0^L (x_1-L)^2(x_2-L)^2 dx_1 dx_2$	α^2
C_4	$C_4 = \int_0^L \int_0^L \int_0^L x_1(x_1-L)^2 x_2(x_2-L)^2(x_3-L)^2 dx_1 dx_2 dx_3$	$\alpha\beta^2$

Summary of V_i Functions

Table A.2: Summary of V_i Functions

Parameter	Expression
$V_1(\kappa)$	$V_1(\kappa) = \int_0^L x_1(x_1-L)^2 e^{ix_1\kappa} dx_1 \cdot \int_0^L (x_2-L)^2 e^{-ix_2\kappa} dx_2$
$V_2(\kappa)$	$V_2(\kappa) = \int_0^L x_1(x_1-L)^2 e^{ix_1\kappa} dx_1$
$V_3(\kappa)$	$V_3(\kappa) = \int_0^L (x_1-L)^2 e^{ix_1\kappa} dx_1$

Table A.3: Summary of Expression for $\varepsilon[h^2]$ Established Using a First-Order Taylor Series Expansion

Parameter	Coefficient	Expression
$\varepsilon[X^2]$ Eq. (37)	$1/\alpha^2$	$\varepsilon[X^2]=\beta^2+\int_{-\infty}^{+\infty} S_{ff}(\kappa)\,\lvert V_2(\kappa)\rvert^2\,d\kappa$
$\varepsilon[XY]$ Eq. (33)	$-2\beta/\alpha^3$	$\varepsilon[XY]=\alpha\beta+\int_{-\infty}^{+\infty} S_{ff}(\kappa)V_1(\kappa)d\kappa$
$\varepsilon[Y^2]$ Eq. (41)	$1/\alpha^4$	$\varepsilon[Y^2]=\alpha^2+\int_{-\infty}^{+\infty} S_{ff}(\kappa)\,\lvert V_3(\kappa)\rvert^2\,d\kappa$
$\varepsilon[h^2]$ Eq. (44)		$\varepsilon[h^2]=\frac{\beta^2}{\alpha^2}+\int_{-\infty}^{+\infty} S_{ff}(\kappa)\frac{1}{\alpha^2}\left[\lvert V_2(\kappa)\rvert^2-\frac{2\beta}{\alpha}V_1(\kappa)+\frac{\beta^2}{\alpha^2}\lvert V_3(\kappa)\rvert^2\right]d\kappa$

Table A.4: Summary of Expression for $\varepsilon[h^2]$ Established Using a Second-Order Taylor Series Expansion

Parameter	Coefficient	Expression
$\varepsilon[X^2]$ Eq.(37)	$4/\alpha^2$	$\varepsilon[X^2]=\beta^2+\int_{-\infty}^{+\infty} S_{ff}(\kappa)\lvert V_2(\kappa)\rvert^2\,d\kappa$
$\varepsilon[XY]$ Eq. (33)	$-10\beta/\alpha^3$	$\varepsilon[XY]=\alpha\beta+\int_{-\infty}^{+\infty} S_{ff}(\kappa)V_1(\kappa)d\kappa$
$\varepsilon[Y^2]$ Eq. (41)	$6\beta^2/\alpha^4$	$\varepsilon[Y^2]=\alpha^2+\int_{-\infty}^{+\infty} S_{ff}(\kappa)\lvert V_3(\kappa)\rvert^2\,d\kappa$
$\varepsilon[X^2Y]$ Eq. (54)	$-4/\alpha^3$	$\varepsilon[X^2Y]=\alpha\beta^2+\int_{-\infty}^{+\infty} S_{ff}(\kappa)\left[\alpha\lvert V_2(\kappa)\rvert^2+2\beta V_1(\kappa)\right]d\kappa$
$\varepsilon[XY^2]$ Eq. (56)	$8\beta/\alpha^4$	$\varepsilon[XY^2]=\alpha^2\beta+\int_{-\infty}^{+\infty} S_{ff}(\kappa)\left[2\alpha V_1(\kappa)+\beta\lvert V_3(\kappa)\rvert^2\right]d\kappa$
$\varepsilon[X^2Y^2]$ Eq. (57)	$1/\alpha^4$	$\varepsilon[X^2Y^2]=\alpha^2\beta^2+\int_{-\infty}^{+\infty} S_{ff}(\kappa)\left[\alpha^2\lvert V_2(\kappa)\rvert^2+4\alpha\beta V_1(\kappa)+\beta^2\lvert V_3(\kappa)\rvert^2\right]d\kappa$
$\varepsilon[Y^3]$ Eq. (58)	$-4\beta^2/\alpha^5$	$\varepsilon[Y^3]=\alpha^3+\int_{-\infty}^{+\infty} S_{ff}(\kappa)\left[3\alpha\lvert V_3(\kappa)\rvert^2\right]d\kappa$
$\varepsilon[XY^3]$ Eq. (59)	$-2\beta/\alpha^5$	$\varepsilon[XY^3]=\alpha^3\beta+\int_{-\infty}^{+\infty} S_{ff}(\kappa)\left[3\alpha^2V_1(\kappa)+3\alpha\beta\lvert V_3(\kappa)\rvert^2\right]d\kappa$
$\varepsilon[Y^4]$ Eq. (60)	β^2/α^6	$\varepsilon[Y^4]=\alpha^4+\int_{-\infty}^{+\infty} S_{ff}(\kappa)\left[6\alpha^2\lvert V_3(\kappa)\rvert^2\right]d\kappa$
$\varepsilon[h^2]$ Eq. (61)		$\varepsilon[h^2]=\frac{\beta^2}{\alpha^2}+\int_{-\infty}^{+\infty} S_{ff}(\kappa)\frac{1}{\alpha^2}\left[\lvert V_2(\kappa)\rvert^2-\frac{4\beta}{\alpha}V_1(\kappa)+\frac{3\beta^2}{\alpha^2}\lvert V_3(\kappa)\rvert^2\right]d\kappa$